Missouri S&T Library and Learning Resources

Scholars' Mine

Doctoral Dissertations | Student Theses and Dissertations

Summer 2008

Characterization and synthesis of nanoscale materials

Jinfeng Wang

Follow this and additional works at: https://scholarsmine.mst.edu/doctoral_dissertations

 Part of the Physics Commons

Department: Physics

Recommended Citation

Wang, Jinfeng, "Characterization and synthesis of nanoscale materials" (2008). *Doctoral Dissertations*. 2141.
https://scholarsmine.mst.edu/doctoral_dissertations/2141

This thesis is brought to you by Scholars' Mine, a service of the Missouri S&T Library and Learning Resources. This work is protected by U. S. Copyright Law. Unauthorized use including reproduction for redistribution requires the permission of the copyright holder. For more information, please contact scholarsmine@mst.edu.

CHARACTERIZATION AND SYNTHESIS OF NANOSCALE MATERIALS

by

JINFENG WANG

A DISSERTATION

Presented to the Faculty of the Graduate Schools of the

MISSOURI UNIVERSITY OF SCIENCE AND TECHNOLOGY

AND

UNIVERSITY OF MISSOURI-ST. LOUIS

In Partial Fulfillment of the Requirements for the Degree

DOCTOR OF PHILOSOPHY

In

PHYSICS

2008

Approved by

Phil Fraundorf, Chair
George D. Waddill, Co-Chair
Jingyue Liu
F. Scott Miller
Bernard J. Feldman
Paul E. Parris

© 2008
JINFENG WANG
All Rights Reserved

PUBLICATION DISSERTATION OPTION

This dissertation consists of the following articles:

Pages 52-64 are going to submit to Journal of Nanotechnology.

Pages 65-81 are going to submit to Journal of Nanoletter.

Pages 82-95 are going to submit to Journal of Advanced Materials.

Pages 96-103 are going to submit to Journal of Advanced Materials.

Pages 117-128 are published in Journal of Microscopy and Microanalysis 2007 pp 768.

ABSTRACT

This dissertation focuses on the systematic study of techniques for characterization and synthesis of nanoscale materials. We have achieved several goals.

Firstly, high number density uniform zinc oxide nanostructure growth has been achieved using thermal evaporation, through control of experimental parameters that include source material temperature, substrate temperature, substrate material, gas flow rate, and choice of catalyst. Aligned zinc oxide nanowires, randomly oriented zinc oxide nanowires, zinc oxide container-shaped structures, and zinc oxide nanobelts have been synthesized with high yield.

Secondly, using a one parameter family of lattice fringe geometry curves, we show how to examine the epitaxial relationship between catalyst particles and a cylindrical support. Using digital darkfield techniques, this investigation can be automated.

Thirdly, the structure relationship between catalyst particles and zinc oxide nanowires has been investigated using scanning and high resolution scanning transmission electron microscopes. A vapor-solid-solid growth model involving a hexagonal array of aligned growth regions is proposed in zinc oxide nanowire formation. Evidence indicates in particular that gold catalyst particles remain solid during ZnO nanowire growth.

Finally, the effect of tin catalyst thickness on nanostructure formation has been investigated. The catalyst abundance on the substrate has a direct impact on its ability to absorb ZnO. The thicker coated substrates can absorb more source vapor, and form larger structures, than can thinner coated substrates.

ACKNOWLEDGMENTS

I would like to thank Dr. Phil Fraundorf, for his inspiration, guidance and constant support on my project. I would like to thank Dr. Jingyue Liu, for his valuable advice and hearty encouragement. His leadership, logical way of thinking, hard work and scholarship have set up an example I hope to match some day. Their technical contributions to this work, in acquiring and analyzing data, are noted here as well as in many of the figures. I would like thank Dr. Bernard J. Feldman, Dr. George D. Waddill, Dr. F. Scott Miller, Dr. Paul E. Parris for serving as my committee members.

I would like to thank the UMSL Physics & Astronomy department for providing opportunities and financial support for my PhD studies. I would like to thank the Center for Nanoscience for providing facilities for my research. I gratefully acknowledge the financial support from University of Missouri research board.

Thanks also go to Dr. Zhou Dan for his help with my experiments. Special thanks are given to members in the Materials Science and Technology Division at Oak Ridge National Laboratory. Research sponsored by Asst. Sec. for Energy Efficiency and Renewable Energy, Off. of FreedomCAR and Vehicle Technologies, as part of the High Temperature Materials Laboratory User Program, ORNL, managed by UT-Battelle LLC for the U.S. Department of Energy, under contract # DE-AC05-00OR22725. The names that specially need to be mentioned here are: Dr. Lawrence F. Allard and Dr. Jane Y. Howe.

Finally I owe my loving thanks to my parents and my sisters, who have taught me to be a strong person physically and mentally.

TABLE OF CONTENTS

Page
PUBLICATION DISSERTATION OPTION.....iii
ABSTRACT……..iv
ACKNOWLEDGMENTS……...v
LIST OF FIGURES viii
LIST OF TABLES.....xv
SECTION
1. INTRODUCTION.....1
1.1. NANOSCIENCE AND NANOTECHNOLOGY.....1
1.2. NANOSCALE MATERIAL APPLICATIONS.....2
1.2.1. Carbon nanotube applications.....3
1.2.2. Zinc oxide nanostructure applications.…....…….…....7
1.2.3. Other metal oxide nanostructure applications...…….....8
1.3. SYNTHESIS TECHNIQUES.....……....…..10
1.4. CHARACTERIZATION TECHNIQUES.....……....14
1.5. TARGETS OF THE THESIS.....……...17
2. ZINC OXIDE NANOSTRUCTURES AND SYNTHESIS TECHNIQUES.....19
2.1. ZINC OXIDE NANOSCALE MATERIALS.....19
2.2. SYNTHESIS METHODS.....20
2.2.1 Source temperature effect.....23
2.2.2 Substrate temperature effect.....25
2.2.3 Gas flow rate effect.....26
2.2.4 Total and partial pressure effect.....27
2.2.5 Substrate material effect.....28
2.2.6 Catalyst effect.....30
2.2.7 Oxygen effect.....32
2.3. CRYSTAL GROWTH THEORETICAL BACKGROUND.....33
2.4. RESULTS ON VARIOUS MATERIAL SYSTEMS.....36

PAPER

1. LATTICE FRINGE SIGNATURES OF EPITAXY ON NANOTUBES.....52

1.1. INTRODUCTION.....52

1.2. THEORY.....54

1.2.1. Fringe visibility theory.....54

1.2.2. Predictions from visibility theory.....55

1.2.3. Computer experiment results.....59

1.2.3.1. Manual count result.....59

1.2.3.2. Digital darkfield imaging technique result.....59

1.3. EXPERIMENTAL TEST.....62

1.4. DISCUSSION AND CONCLUSIONS.....62

1.5. FUTURE WORK.....64

2. GROWING ZnO NANOWIRES VIA DIFFUSION ON AU.....65

3. EFFECTS OF CATALYST THICKNESS ON THE GROWTH OF ZINC OXIDENANOSTRUCTURES.....82

4. VERTICALLY ORIENTED ZINC OXIDE NANOCONTAINERS GROWN ON MICA SUBSTRATES.....96

SECTION

3. SUMMARY AND OUTLOOK.....104

3.1. NANOSTRUCTURE APPLICATIONS.....104

3.2. CHALLENGES AND OUTLOOK.....107

APPENDIX

SYNTHESIS AND CHARACTERIZATION OF ANTIMONY-DOPED TIN OXIDE NANOSTRUCTURES.....117

BIBLIOGRAPHY..... 129

VITA 143

LIST OF FIGURES

Figure Page

INTRODUCTION

1.1. SEM image of tin oxide nanowires.....9

1.2. SEM image of silicon oxide nanowires..... 10

1.3. SEM image of ZnO nanobelts.....13

1.4. SEM image of ZnO hollow spheres.....14

1.5. Diagram shows that scanning electron microscope (left) and transmission electron microscope (right).....15

1.6. EDX spectrum shows the chemical composition of the specimen.....16

ZINC OXIDE NANOSTRUCTURES AND SYNTHESIS TECHNIQUES

2.1. The diagram of zinc oxide structure using Diamond 3 software.....20

2.2. The diagram of the synthesis setup. HTZ, MTZ, LTZ mean high temperature zone, middle temperature region and low temperature region.....21

2.3. The tube furnace temperature profile distribution.....22

2.4. SEM image shows that zinc oxide cone and comb shapes products fabricated at source temperature of 1100°C. (a) and (b) were comb-shape structures formed at 900ºC region. (c) and (d) were hexagonal cone shape structures formed at 700ºC region.....24

2.5. Low magnification and high magnification SEM images show uniform zinc oxide nanowires synthesized using 1000°C condition.....25

2.6. (a) ZnO film like structures form at 900°C-950°C region, (b) ZnO ribbon or belt shape structures nucleate at 600°C-850°C, and (c) ZnO nanowires form at temperature blow 600°C.....26

2.7. SEM image (a) randomly oriented ZnO nanowires on (100) silicon wafer substrate. (b) Aligned ZnO nanowires nucleate on mica substrates.....30

2.8. (a) ZnO particles nucleate on the catalyst-free substrate; (b) Under the same experimental condition ZnO wire-like structures form on a tin catalyst substrate.....31

2.9. Schematic diagram illustrates that vapor-liquid-solid aligned growth of metal oxide nanowires, via the use of metal nanoparticles as catalysts for nucleation and growth of nanostructures.....34

2.10. Schematic diagram illustrates that the metal oxide nanowires via vapor-solid-solid mechanism.....35

2.11. Schematic illustrates that metal oxide nanostructures form on the substrate directly via vapor solid mechanism.....36

2.12. SEM image of gold particle.....37

2.13. Gold particle size distribution.....37

2.14. (a) Aligned zinc oxide nanowires with gold particles on the tip at substrate temperature 600ºC-850ºC. (b) Randomly orientated zinc oxide nanowires were found at substrate temperature below 600ºC.....38

2.15. Gold and zinc oxide nanowire diameter size distribution.....39

2.16. Correlation between gold and zinc oxide diameter on individual wires.....40

2.17. Low magnification STEM images of Au-ZnO nanowire image. (a) High angle annular darkfield (HA-ADF) image. (b) The corresponding bright field image.....41

2.18. (a) The bright field STEM image of the gold catalyzed zinc oxide nanowire. (b) Darkfield STEM image of the same sample. (c) The FFT pattern of gold particle part. (d) The FFT pattern of zinc oxide nanowire part. (e) The FFT pattern of the whole image.....42

2.19. SEM image of Pd/Au catalyst particle.....43

2.20. Pd/Au alloy particle size distribution. 43

2.21. (a) Aligned zinc oxide nanowires with Pd/Au particles on the tip at substrate temperature 600ºC-850ºC. (b) Randomly oriented zinc oxide nanowires were found at substrate temperature below 600ºC.....44

2.22. Low magnification STEM images of PdAu-ZnO nanowire image. (a) High angle annular darkfield (HA-ADF) image. (b) The corresponding bright field image.....45

2.23. Low magnification TEM image (a) shows a nanoparticle located at the tip of a ZnO nanowire. EDS spectra (b) show the element information on different locations. Location 1 is mainly at PdAu particle position. Location 2 is located at ZnO nanowire. (Ti peak comes from the Ti TEM grid). 2 has Zn peak without apparent PdAu peak.....46

2.24. SEM image of tin catalyst particle.....47

2.25. (a) Low magnification SEM image of tin catalyzed zinc oxide nanobelts with TEM grid as mask. (b) High magnification SEM image of zinc oxide nanobelts.....48

2.26. High resolution transmission electron microscope image of zinc oxide nanobelt. The inset shows that zinc oxide grows along {10.0} direction.....49

2.27. ZnO nanobelt diagram.....50

PAPER 1

1.1. Low magnification (left) and high magnification TEM image of Pt particles supported by carbon nanotubes.....54

1.2. Illustrated Pt lattice fringe patterns expected on carbon nanotube.....56

1.3. The diagram showed the relationship between azimuthal angle of (111), (200) and (220) FCC Pt crystals and the fraction radial distance from the center of the tube in the columnar growth model (left). Right was relationship between azimuthal angel of (111) FCC fringe and fraction radial distance from the center of the tube in epitaxally growth model on armchair nanotube.....58

1.4. The azimuthal angle of (111) Pt lattice fringes versus projected distance from the tube axis for a columnar growth model specimen. The fractional radial distance was from center of the tube (0) to the edge of the tube wall (1).....60

1.5. Using digital darkfield image technique, (111) lattice fringes were light up at the direction.....61

1.6. 2.3 Angstrom periodicity along various directions in a lattice image, combine with fringe visibility theory to analyze the crystallographic relationship between some nanoparticles and a cylindrical structure on which they lie.....62

1.7. Experimental data was superimposed on the previous model data.....63

PAPER 2

2.1. FESEM image of zinc oxide nanowires. (a) Low magnification SEM image of ZnO nanowire grown from the patterned Au. (b) High magnification SEM image of ZnO nanowire, showing that the nanowires have uniform diameters and clean smooth surface with gold catalysts on the tip of the nanowires. (c) High magnification backscattering SEM image of nanowire structures. Gold particles show up clearly due to the high atomic number. (d) Backscattering SEM image of the same area at different focus. Gold particles exist on inner layer individual nanowire.....69

2.2. Low magnification HA-ADF image (a) shows a faceted Au nanoparticle located at the tip of a ZnO nanowire. Optical diffractogram (b) shows the structure relationship between Au catalyst particle and ZnO nanowires. Diagram schematics image (c) shows the relationship between Au and ZnO nanowire. High resolution HA-ADF image (d) shows the interfacial structure between the Au nanoparticle and the ZnO nanowire.....70

2.3. Figure (a) shows the profile of HAADF intensity along rows of atoms parallel to the interface. The gradual decrease of intensity in moving from Au to ZnO likely comes from C contamination on the specimen. Fourier transform amplitude spectra from rows on either side of that anomalous layer are shown in Figure (b). Note that there is evidence for a mixing of Au and ZnO periodicities only in the modulated layer, and in the Au layer immediately below that.....72

2.4. HA-ADF image (a) shows the Au nanoparticles are locating off the direction of the nanowire's growth direction. High resolution STEM image (b) shows that the epitaxial relationship between Au and ZnO nanowire. HA-ADF image (c) and bright field image (d) shows that gold particle is embedded in the nanowire. High resolution STEM image (e) shows that there is 6 degree angle between Au (111) lattice fringe and ZnO (0002) lattice fringe.....73

2.5. At lower magnifications and off-zone orientations, a periodic array of dislocations is apparent, as illustrated here with images of two different regions.....74

2.6. Schematic of atoms at a ZnO {0001} on Au {111} interface viewed face-on, with relative azimuthal rotation that agrees with data reported. Note that there are three types of alignment which have 3-fold symmetry: Zn over Au, O over Au, and neither over Au. HAADF contrast in the modulated interface layer suggests that one of the alignments may be preferred for catalytic incorporation of ZnO into the growing nanowire. The field with is 4nm.....76

2.7. Low magnification TEM image (a) shows a nanoparticle located at the tip of a ZnO nanowire. EDS spectra (b) show the element information on different location. Location 1 is mainly at gold particle position. Location 2 is located at ZnO nanowire. (Ti peak comes from the Ti TEM grid). 2 has Zn peak without apparent Au peak. Electron beam builds carbon contamination around sample surface as shown in location 3.....77

2.8. The proposed formation mechanism: ZnO vapor diffuses over the gold particle and forms the nanowire.....80

PAPER 3

3.1. The substrate is divided by three parts. One third of the substrate is the tin film coated region, one third of the substrate is tin particle coated part and one third of the substrate has no catalyst.....84

3.2. Various ZnO nanostructures were fabricated on 850ºC at the different substrates. ZnO particles deposit on the clean substrate without coating as shown in Figure a. Short aligned nanowires with conical shape form on the tin particle coated substrate as shown in Figure b. Belt shape structures are concentrated in the thick tin film coated substrate as shown in Figure c. All the experimental conditions are the same except for the catalyst coating 86

3.3. Various ZnO nanostructures are fabricated on 750ºC on the different substrates. ZnO particles deposit on the clean substrate without coating as shown in Figure a. Figure b exhibits the long aligned nanowires on the tin particle coated substrates. Figure c shows that belt shape structures are formed on the thick tin film coated substrates.....87

3.4. Various ZnO nanostructures are fabricated on 650ºC on the different substrates.....89

3.5. The diagram shows that facet individual nanoparticles formation process on mica substrate.....90

3.6. The diagram shows that aligned nanowire formation process on tin particles coated mica substrate.....91

3.7. The diagram shows that nanobelt formation process on thick tin film coated mica substrate.....92

3.8. Low magnification SEM image shows the interface between nanoparticles and aligned zinc oxide nanowires.....94

3.9. Low magnification SEM image shows the interface between aligned zinc oxide nanowires and zinc oxide nanobelts.....95

PAPER 4

4.1. (a) Low magnification SEM image of zinc oxide nanocontainers grown on mica substrate; (b) higher magnification SEM image of top view nanocontainers.....98

4.2. (a) Some of nanocontainers are covered; (b) most of the lids are covered and form a tip on each container.....99

4.3. SEM images of cone shape nanocontainers. (a) is the low magnification SEM image of the containers. High magnification SEM image (b) shows that the diameter of the container is around 2 micrometers.....100

4.4. Scanning transmission electron microscope images of zinc oxide nanocontainers. (a) is high angle annular darkfield image of the container and (b) is the bright field image. (c) is high angle annular darkfield image of another container and (d) is the bright field image.....101

4.5. Schematic steps of formation of nanocontainers.....102

SUMMARY AND OUTLOOK

3.1. Low magnification SEM image of Pd particles on zinc oxide nanobelt. 105

3.2. High magnification SEM image of Pd particles on zinc oxide nanobelt. 105

3.3. (a) Low magnification high angle annual darkfield STEM (HA-ADF) image of Pd on ZnO nanobelt. (b) High magnification STEM bright field image of Pd particle on the center of the nanobelt. (c) and (d) are HA-ADF images of Pd particle on the side of the nanobelt.....106

3.4. High resolution STEM image of tin catalyzed zinc oxide nanobelt.....107

3.5. (a).Low magnification transmission electron microscope image of zinc oxide nanobelt. (b). Energy dispersive spectra obtained from the zinc oxide nanobelt.....109

3.6. SEM image of zinc oxide hollow sphere structures.....111

3.7. TEM image of the zinc oxide spheres. From the images, we can see that some of the spheres are hollow inside.....112

3.8. (a) Zinc oxide triangle shape needles. (b) Zinc oxide hexagonal shape nanorods with a sharp tip. (c) Zinc oxide needle flowers. (d) Zinc oxide flower like shape structures.....113

3.9. Zinc oxide golf rod shape structures.....114

3.10. Zinc oxide fence structures.....114

3.11. The lantern shape structures made of silicon oxide nanowire.....115

3.12. SEM image of silica “glasses”. The diameter of the glasses is around 20 micrometers.....115

3.13. Tin oxide zigzag shape nanowires. Every about 2 micrometers there is a 75º kink and form the zigzag shape.....116

APPENDIX

A1. SEM image shows silicon substrate coated with gold nanoparticles.....119

A2. (a**)** ATO powders growing on the clean silicon substrate.
(b) shows growth of ATO powders on the Au/Si substrate,
revealing the presence of large Au particles. The temperature
of the silicon substrates was about 700ºC-800ºC.....120

A3. (a) ATO clusters on the clean silicon wafer at 600ºC -700ºC
temperature zone. (b) Au-promoted growth of ATO nanowires
at the same 600ºC -700ºC temperature zone.....121

A4. (a) ATO powders on the clean silicon wafer at 500ºC -600ºC
temperature zone. (b) Au-promoted growth of ATO nanocones
at the same 600ºC -700ºC temperature zone.....122

A5. ATO nanowires formed on the gold coated silicon
wafers at 600ºC -700ºC temperature zone.....124

A6. ATO nanocones formed at 500ºC -600ºC temperature zone.....125

A7. HRTEM image shows ATO nanowires lattice fringe.
0.27nm is tin oxide orthorhomic structure (114) spacing,
0.39nm is (004) spacing and 0.36nm is (110) spacing.
The small inset is corresponding diffraction pattern of same location.....126

A8. A representative SEM image of the fabricated ATO products.
A unique tree-like structure was frequently observed.
It is interesting to note that most of the tree branches have
flag-like morphology at the tips of the branches. The
dendritic (figure A9) structures are artistically amusing,
but the presence of these structures reduces the
yield of the desired structures.....127

A9. Unique hollow structures have also been observed.
These tube structures seem to have a well-defined
external shape (square prism).....128

LIST OF TABLES

Table Page

INTRODUCTION

1.1 Catalytic, electrical, magnetic, mechanical, optical, sterical and biological advantage of nanomaterials (Cao 2004).....4

1.2 Carbon nanotube synthesis methods (Guo et al. 1995a).....7

ZINC OXIDE NANOSTRUCTURES AND SYNTHESIS TECHNIQUES

2.1 Synthesis parameters of different ZnO nanostructures in our system.....32

2.2 Comparison of Zinc oxide nanostructure length, width, formation temperature and number density.....51

1. INTRODUCTION

1.1. NANOSCIENCE AND NANOTECHNOLOGY

Generally, nanomaterials are defined by component structures whose dimensions are within 1-100nm (Rosei 2004). Nanoscience is the fundamental study of nanomaterials, and nanotechnology is comprised of techniques for their creation and application (Ebbesen et al. 2006). In the past decade, nanoscience and nanotechnology have become rapidly growing research and development fields. They are beginning to change daily life. Their techniques are used for manufacturing, medicine, security, defense, energy production and storage, environmental management, transportation, communication, computation and education (Correia et al. 2007). Nanoscience is a multidisciplinary science, rather than an individual science, which draws many traditional sciences together. Fields that exhibit new life as a result include applied physics, material science, interface and colloid science, device physics, supramolecular chemistry, chemical engineering, mechanical engineering, biological engineering, and electrical engineering.

Nanoscience is an old science, which can be tracked back to early 19^{th} century (Faraday 1857). Richard Feynman in 1959 gave a famous talk titled “There is plenty room at the bottom”. In his talk, he predicted that with the help of new experimental techniques and instruments, the building blocks of matter can be visualized and modified with atomic precision. In 1974, Taniguchi defined nanotechnology as processing, consolidation, and deformation of materials by one atom or by one molecule (Taniguchi 1974). The first nanotechnology application was invention of the scanning tunneling microscope (STM) in 1986 by Binning and Rohrer. Later IBM Company used STM to

spell “IBM” letters using STM. It is the first time humans used the instrument to manipulate one atom at a time. Sophisticated instruments for characterization and manipulation such as scanning electron microscopy, transmission electron microscopy, and scanning probe microscopy are now available for researchers to approach the nanoworld. With deeper understanding of the nanoworld, more and more nanotechnologies are being applied in our everyday life. The vision of nanotechnology advances broad societal goals, such as improved understanding of nature extending the potential of the human creativity (Roco 2003).

1.2. NANOSCALE MATERIAL APPLICATIONS

A wide variety of nanostructures have already been observed and utilized. According to shape and size, nanostructures can be separated into three different categories. The first category is zero dimensional structures. Quantum dots or nanoparticles are usually put in this category. The second category is one dimensional nanostructures, which includes nanowires, nanorods, and nanotubes. The third is two dimensional nanostructures, which includes thin films, nanoribbons and nanobelts. Nanostructures have features in between of those of bulk materials and single atoms. Nanomaterial properties are significantly different from those of atoms and bulk materials. Nanoscale materials have a large fraction of surface atoms, high surface energy, spatial confinement, and reduced imperfections (Cao 2004). When nanomaterial sizes are comparable to the Debye length, the entire material is affected by its surface properties (Ogawa et al. 1982). For example, metallic nanoparticles can be used as active catalysts. Chemical sensors which are made of nanoparticles and nanowires may have high sensitivity and sensor selectivity. Energy band structures and charge carrier density

also modify the electrical and optical properties. For example, nanoparticle and nanowire lasers and light emitting diodes (LED) are very promising in future optoelectronics. Control of imperfections can have profound effects on the mechanical properties on the nanostructures. For example, carbon nanotubes have superior mechanical properties. Nanostructure properties are summarized in the Table below.

These properties have drawn much attention due to their wide ranging applications. Nanowires can be applied in nanophotonics, lasers, nanoelectronics, solar cells, resonators and high sensitivity sensors. Nanoparticles can be used as catalysts, functional coatings, nanoelectronics, energy storage, drug delivery and biomedicines. Nanostructured thin films can be used in light emitting devices, displays and high efficiency photovoltaics.

Here, this dissertation focuses on two special nanomaterials, namely carbon nanotubes and metal oxide wires.

1.2.1. Carbon nanotube applications Carbon nanotubes were discovered by Sumio Iijima in 1991 (Iijima 1991). The diameter of the carbon nanotube is on the order of few nanometers, and the length is up to few millimeters. Depending on the number of wall layers, carbon nanotubes fall into two different categories. One is the single walled carbon nanotube (SWCNT). The other one is the multi-walled carbon nanotube (MWCNT). The diameter of single walled carbon nanotubes is usually between 1 and 5 nm. It is defined by the rolling one atomic layer of graphene into a cylinder. Multi walled carbon nanotubes involve the wrapping of more than one layer of graphene together. Depending on the wrapping direction, single walled carbon nanotubes are classified as zigzag, armchair and chiral (Dresselhaus et al. 1996).

Table 1.1 Catalytic, electrical, magnetic, mechanical, optical, sterical and biological advantages of nanomaterials (Cao 2004).

Properties	**Examples**
Catalytic	Better catalytic efficiency through higher surface-to-volume ratio
Electrical	Increased electrical conductivity in ceramic and magnetic nanocomposites, increased electric resistance in metals
Magnetic	Increased magnetic coercivity up to a critical grain size, superparamagetic properties
Mechanical	Improved hardness and toughness of metals and alloys, ductility and superplasticity of ceramics
Optical	Spectral shift optical absorption and fluorescence properties, increased quantum efficiency of semiconductor crystals
Sterical (spatial arrangement of atoms in molecules)	Increased selectivity, hollow spheres for specific drug transportation and controlled release
Biological	Increased permeability through biological barriers, improved biocompatibility

Carbon nanotubes have plenty of special properties, including mechanical properties, thermal properties, and electrical properties. Carbon nanotubes are strong and stiff compared to other materials. They have good thermal conductivity. Depending on their chirality, single walled carbon nanotubes exhibit metallic and semiconducting behavior (Hamada et al. 1992; Saito et al. 1992; Odom et al. 1998; Wildoer et al. 1998). Because of these unique properties, many research and development opportunities have emerged in the past few years. Carbon nanotubes can be used as a bridge in field effect transistors to connect the source and drain terminals (Tans et al. 1998). Carbon nanotubes have atomic robustness, and an ability to carry more current than conventional semiconductors by size at room temperature. Due to this special property, carbon nanotubes may be used in channels or gates in future electronics (Chen et al. 2006). Carbon nanotube based gas sensors have higher sensitivity, faster response, and lower operating temperature than other gas sensors (Kong et al. 2000; Kong et al. 2001; Cantalini et al. 2003; Li et al. 2003a; Pengfei et al. 2003; Snow et al. 2005). Carbon nanotubes can be functionalized to use as biosensors. Recently, experiments have been conducted to fabricate nano devices with carbon nanotubes incorporated into electronic circuits, to work faster and with less power consumption (Lin et al. 2005a).

Due to their cylindrical structure, carbon nanotubes can also be used as drug delivery capsules. Carbon nanotubes are called “magic bullets” for carrying drugs (Couvreur et al. 2006). Attaching the drug to the inner tube wall, or inserting it in particle form, the drug may be released at particular sites after transport (Gasparac et al. 2004; Kim et al. 2005).

Recently, people have used carbon nanotubes instead of carbon black to attach catalyst particles like Pt or Pt-Ru, to generate powder more efficiently (Han et al. 2004a; Xing et al. 2004; Ye et al. 2004; Gu et al. 2005; Lin et al. 2005b; Chien et al. 2006; Remita et al. 2006; Guo et al. 2008). Direct methanol fuel cells use methanol as the fuel, because of the easy storage. Energy is generated on reaction at the cathode. Traditionally, metal catalysts are supported by carbon black. Recently, more and more fuel cell experiments use multi walled carbon nanotubes to support catalyst particles and increase fuel cell performance. Carbon nanotubes can be designed for specific catalyst size distributions. Li (2002) reported that higher maximum power density (47%) was produced using carbon nanotubes than using carbon black.

Techniques have been developed to synthesize carbon nanotubes directly. Carbon nanotubes can be made through arc discharge (Iijima 1991), chemical vapor deposition (Joseyacaman et al. 1993), and laser ablation (Guo et al. 1995a; Guo et al. 1995b) methods. Large quantities of carbon nanotubes can be made using these techniques. A comparison of carbon nanotube synthesis techniques is shown in Table 1.2.

Table 1.2. Carbon nanotube synthesis methods (Guo et al. 1995a).

Arc discharge method	Chemical vapor deposition	Laser ablation (vaporization)
Connect two graphite rods to a power supply, place them millimeters apart, and throw switch. At 100 amps, carbon vaporizes in hot plasma.	Place substrate in oven, heat to 600 C, and slowly add a carbon-bearing gas such as methane. As gas decomposes it frees up carbon atoms, which recombine in the form of nanotubes	Blast graphite with intense laser pulses; use the laser pulses rather than electricity to generate carbon gas from which the nanotubes form; try various conditions until hit on one that produces prodigious amounts of single wall carbon nanotubes
Can produce single wall carbon nanotube and multi wall carbon nanotubes with few structural defects	Easiest to scale to industrial production; long length	Primarily single wall carbon nanotubes, with a large diameter range that can be controlled by varying the reaction temperature
Tubes tend to be short with random sizes and directions	Nanotubes are usually multi wall carbon nanotubes and often riddled with defects	By far the most costly, because requires expensive lasers

1.2.2. Zinc oxide nanostructure applications Zinc oxide nanostructures have plenty of applications in electronics, optics and photonics due to its wide band gap of 3.37eV and exciton binging energy of ~60meV, which permits excitonic emission at room temperature and above (Wang 2004; Vlasenko et al. 2005). In our experiments, zinc oxide nanowires, nanobelts, hollow spheres and castle-shaped structures have been fabricated and will be discussed later. Zinc oxide nanostructures can be applied to room-temperature ultraviolet (UV) lasers and blue light emitting devices (Bagnall et al. 1997; Service 1997; Cao et al. 2000; Huang et al. 2001a; Liu et al. 2003a), UV photodetectors (Kind et al. 2002), sensors (Shibata et al. 2002; Mitzner et al. 2003), photocatalysts (Yumoto et al. 1999), solar cell (Keis et al. 1999; Hara et al. 2000; Law et al. 2005),

nanogenerators (Wang et al. 2007b), and field emission devices (Lee et al. 2002; Zhu et al. 2003). We will talk more about zinc oxide nanostructures in chapter 2 and 4.

1.2.3. Other metal oxide nanostructure applications Tin oxide nanowires have been synthesized in our system, as shown in Figure 1.1. Besides nanowires, various tin oxide nanostructures have been synthesized by many groups, including tin oxide nanorods (Cheng et al. 2004), tin oxide nanotubes (Steinhart et al. 2004), and tin oxide nanobelts (Pan et al. 2001). Deng and Lee recently reported using tin oxide nanoparticles to assemble a highly ordered nanostructure with hollow core shell mesospheres. These nanostructures can be utilized for high capacity Li^+ ion storage (Zhang et al. 2006a; Deng et al. 2008). The size of the tin oxide nanoparticles is very important for the lithium battery performance, where the nanoparticles have greater cyclability than micro tin oxide particles (Young et al. 2006). Mesoporous tin oxide nanostructure is considered to be a good gas sensor candidate. Because this sensor has low electrical resistance, the gas sensitivity is significantly improved (Shimizu et al. 2004). Patterned tin oxide nanostructures are efficient field emission and field emission based flat panel displays (Zhang et al. 2006b).

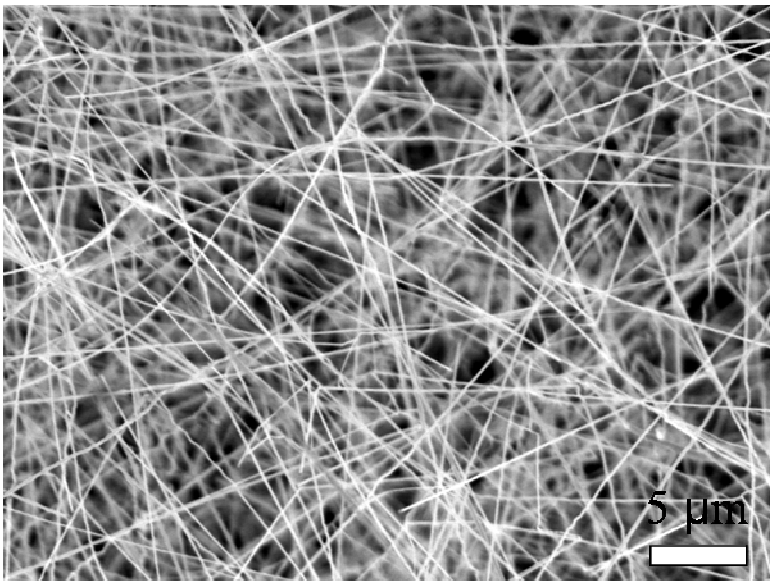

Figure 1.1. SEM image of tin oxide nanowires.

Silicon oxide nanowires have plenty of applications due to their semiconductor property and controllable dopant type and concentration (Cui et al. 2000; Cui et al. 2001a; Duan et al. 2001). They can be used as high sensitive and selective detection sensors for biological and chemical species (Cui et al. 2001b). Silicon oxide nanowires can be applied in field effect transistors, because of controllable hole and electron doping (Cui et al. 2003). Silicon oxide nanowires are synthesized in our system as shown in Figure 1.2. Silica nanotubes have been fabricated using the template method (Fan et al. 2007). Silica nanotube inter wall and outer walls are hydrophilic. The nanotube is easy to form by colloidal suspension, and has good accessibility for surface functionalization. Modified silica nanotubes have good potential applications in bio-separation and bio-catalysis (Mitchell et al. 2002). Silica nanotubes are a promising dielectric material for nanoelectronics applications because of their low dielectric constant (Kovtyukhova et al. 2003).

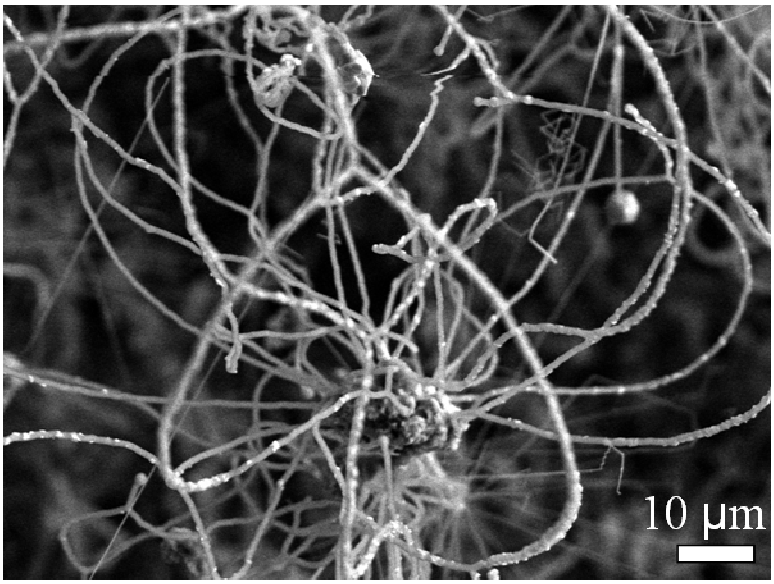

Figure 1.2. SEM image of silicon oxide nanowires (2006, J. Liu).

Besides the nanostructures mentioned above, there are many metal nanostructures and semiconductor nanostructures that have been investigated. Most of these have potential applications.

1.3. SYNTHESIS TECHNIQUES

Metal oxide nanostructures have been studied extensively. Typically, there are two categories of fabrication. One is the “bottom up” technique using vapor phase deposition. The other one is a so called “top-down” technique using lithography, and externally controlled tools to cut, etch, mill, and shape the materials into desired nanoscale objects.

Several approaches have been well established which use vapor phase deposition, including chemical vapor deposition and physical vapor deposition. Physical vapor deposition historically was used to make thin films. Physical vapor deposition is also able to prepare atomic or nanometer scale, by careful monitoring of process conditions (Tjong

et al. 2004). Physical vapor deposition includes evaporation, sputtering, cathodic arc discharge, laser or ion beam ablation (Singh et al. 2005). Thermal evaporation generates source vapor using a furnace, and facilitates the deposition of nanostructures. Zinc oxide nanowires (Huang et al. 2001a), zinc oxide nanocombs (Lao et al. 2005), zinc oxide nanorings (Hughes et al. 2005), and zinc oxide nanobelts (Pan et al. 2001) have been fabricated successfully using thermal evaporation. The sputtering process uses electron ions to eject the target and generate atoms. Sputter methods have been used to synthesize one dimensional nanostructures, like tungsten nanorods (Karabacak et al. 2003), silicon nanowires (Marsen et al. 1999), boron nanowires (Cao et al. 2001; Cao et al. 2002), and carbon nitride nanotubulite (Suenaga et al. 1999). Cathodic arc discharge was used to synthesize carbon nanotubes in 1993 (Bethune et al. 1993; Iijima et al. 1993). This method is still useful in carbon related nanostructure fabrication.

Laser ablation, a method that combines laser ablation cluster formation and vapor liquid solid growth was also developed for the synthesis of semiconductor nanowires. Traditionally, this method was used for thin film coating (Dijkkamp et al. 1987). It uses a laser gun to ablate targets within a quartz furnace tube with appropriate temperature, pressure, and residence time. Various nanostructures have been synthesized using this method (Morales et al. 1998; Lauhon et al. 2002; Han et al. 2004b).

Chemical vapor deposition (CVD) is a more complex method, compared with physical vapor deposition. There are a lot of different kinds of chemical vapor deposition methods. Our method uses the gas phase of source materials to form solid state products with help from the carrying gas. Depending on the operating pressure, the method can be classified as atmospheric pressure chemical CVD, low pressure CVD or ultrahigh

vacuum CVD. Also there are plasma assisted CVD, metal-organic CVD, and hot wire CVD. Many high purity nanostructures have been fabricated using chemical vapor deposition methods. These include tungsten oxide nanowires (Wang et al. 2007a), zinc oxide nanoparticles (Guan et al. 2008b), carbon nanotubes (Cao et al. 2007), tin oxide nanowires (Zeng et al. 2007), zinc oxide nanowires (Wei et al. 2007a), and aluminum-nitride nanowires (Tang et al. 2005).

It is hard to synthesize some nanoscale materials directly using vapor phase methods, like metal nanostructures and multi components semiconductor nanostructures. Gold, silver, platinum nanowires have been synthesized using a solution method (Xia et al. 2003). Some multi component structures also are made by a solution phase method (Urban et al. 2002; Bu et al. 2004). The advantage of the wet chemistry method is that a large amount fabrication can be achieved. The disadvantage is that the purity is not as good as vapor phase synthesis. So contamination is a challenge for this technique.

Lithography is an important method for the semiconductor industry. Traditionally lithography is a technique for printing on smooth surfaces. The image is created after chemical processing. This technique is well applied in nanoscale materials synthesis, especially in semiconductor microchip manufacturing and MEMS devices. The technique involves using photocatalysts (Lee et al. 2004), electrons (Balaur et al. 2004), ions, or an atomic force microscope (Xu et al. 1997) to form a designed pattern on a substrate, then through etching or depositing materials on the surface to get the desired shape. TiO_2 tubes (Lai et al. 2008), graphitic wires (Takai et al. 2007), anodic aluminum oxide pillars (Lee et al. 2005), zinc and zinc oxide particles (Guan et al. 2008a) have all been

synthesized by lithography methods. Regular patterned nanostructures play a central role in artificial systems such as sensors, optoelectronics and emissions.

Among all the synthesis methods, thermal evaporation is the most popular method because of the low cost, high purity, and easy setup. We used the thermal evaporation method to synthesize zinc oxide nanowires, zinc oxide nanobelts, and tin oxide nanowires successfully as shown in Figure 1.3 and 1.4. We also get antimony doped tin oxide nanostructures, which will be illustrated in the appendix.

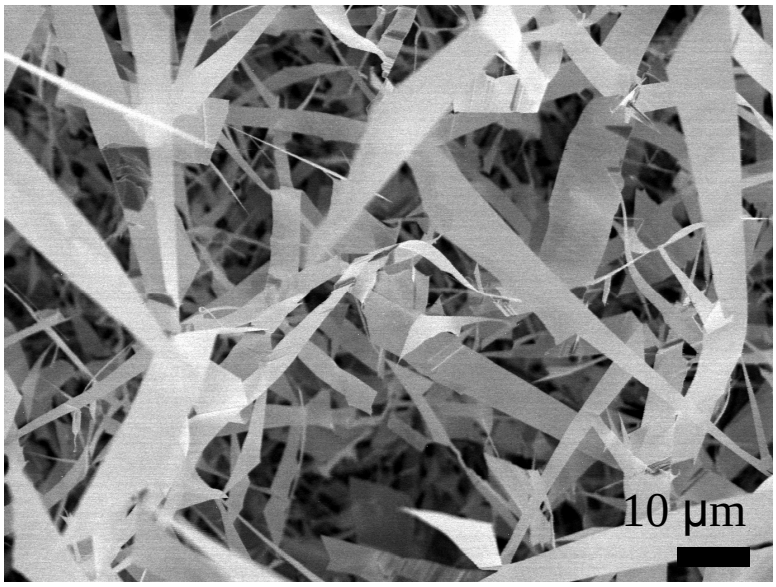

Figure 1.3.SEM image of ZnO nanobelts.

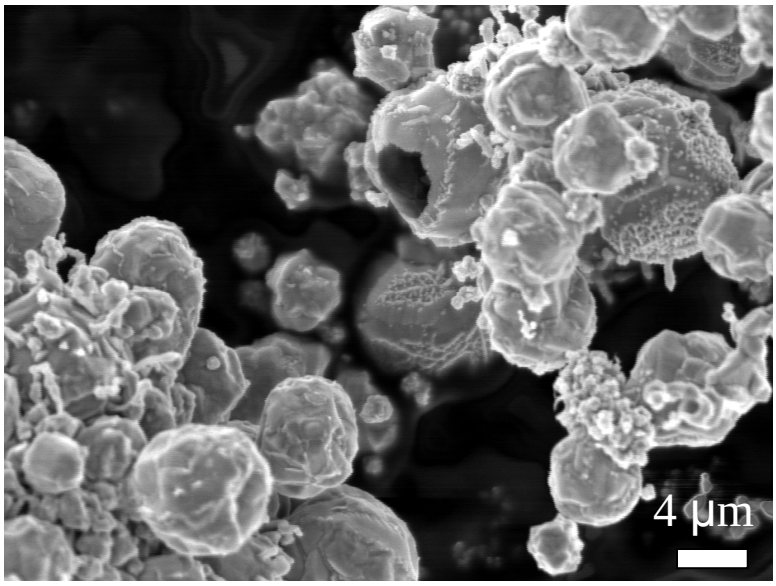

Figure 1.4.SEM image of ZnO hollow spheres (2007, J. Liu).

1.4. CHARACTERIZATION TECHNIQUES

Proper tools are needed to study and "see" nanoscale materials. Several tools have been developed for imaging atomic size structures, including electron microscopy, scanning probe microscopy, and X-ray diffraction technique. X-ray diffraction (XRD) is very useful on crystalline materials. X-ray diffraction provides information on the crystallographic structure, chemical composition, and physical properties of materials and thin films. X-ray beams are scattered after interacting with the sample. The scattered intensity is a function of the incident and scattered angle, polarization, and wavelength or energy. Small single crystal structure information can be determined by X-ray diffraction directly. Powder sample crystal structure and crystal size information can be obtained from the powder method (Warren 1992).

Scanning probe microscopes are microscopes that use physical scanning tips or cantilevers to visualize the sample surface. When the cantilever is close to the sample surface, forces between cantilever and sample will lead to the deflection of the cantilever.

The deflection is measured by the laser spot. The topography of the sample surface is formed from the laser signal (Meyer et al. 2003).

In this work, scanning electron microscopy (SEM) and transmission electron microscopy (TEM) were used for nanoscale materials characterization. SEM gives a good view of structure size and shape. TEM gives specimen crystallography structures and detailed specimen morphology. A simplified illustration of the image forming processes in SEM and TEM is shown in Figure 1.5.

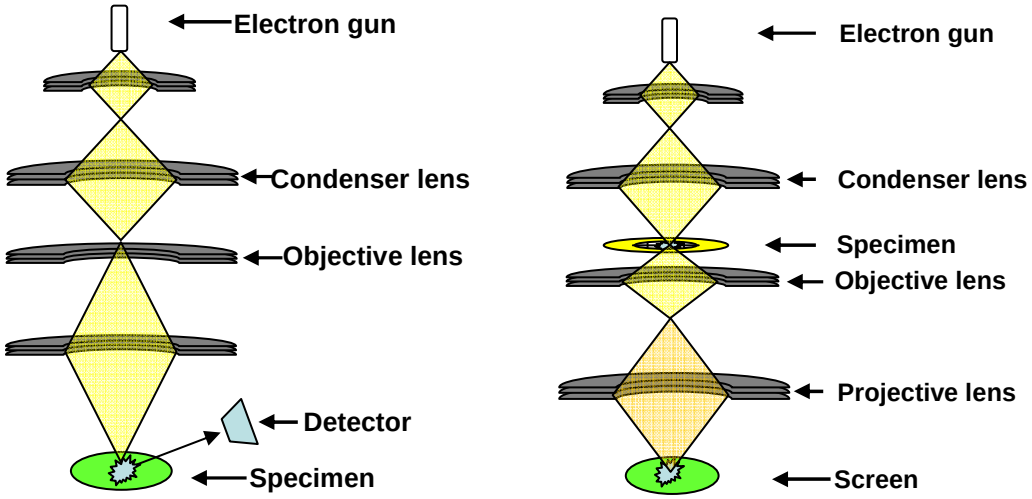

Figure 1.5: Diagram shows that scanning electron microscope (left) and transmission electron microscope (right).

SEM is a key technique for assessing minimum feature size in nanoscale materials research. The fine imaging capability depends on the wavelength of the electrons being much less than the feature size. For SEM, the electron beam is shaped by an electromagnetic condenser lens and focused on sample by objective lens. 1-30kV is the usual acceleration voltage range. The electron optical system is comprised of electromagnetic coils surrounding the column. The focused spot is scanned on the sample

surface, and secondary electrons as well as backscattered electrons emitted by the specimen are detected. The final image is formed by combining the position information from the scanning coil driver with the detector signal. The resolution of SEM is several nanometers. The information on chemical composition can be obtained from energy dispersive x-ray spectroscopy (EDS). SEM is very important for us to evaluate the experimental parameters and design the next round experiments.

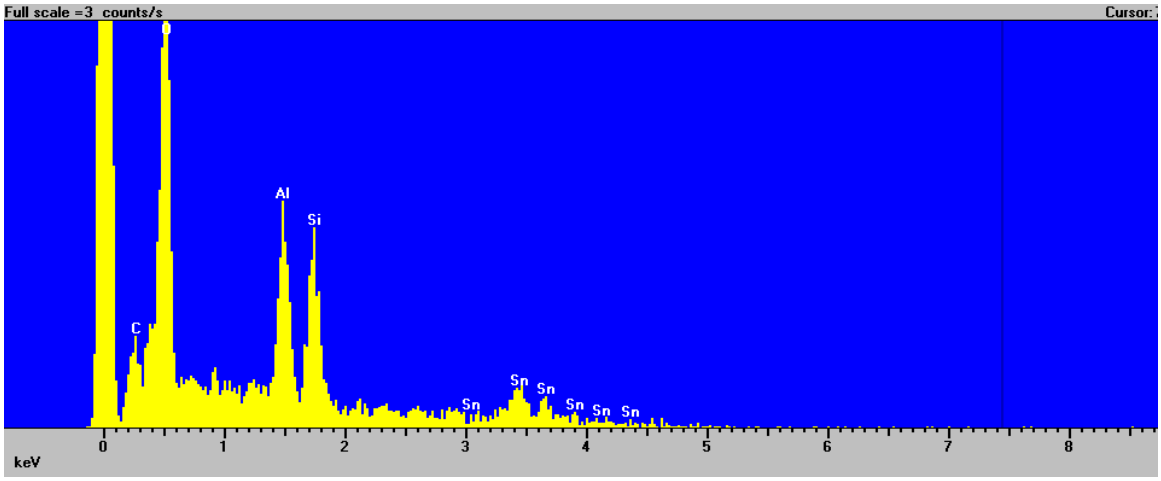

Figure 1.6. EDX spectrum shows the chemical composition of the specimen.

Tungsten hairpin, LaB_6 and field emission source could be utilized as transmission electron microscope electron gun. Most of recent transmission electron microscopes are using field emission source as the gun source duet to the high brightness, high coherent electron emission. The acceleration voltage in TEM is 200-400kV for materials science work. Electrons go through the sample and form images on a fluorescent screen. The image is recorded by CCD camera or negatives. The crystal structure and crystal quality information can be obtained by TEM imaging and electron diffraction patterns. If the material is crystalline, diffraction patterns give reciprocal lattice information.

For any Bravais lattice, three numbers serve to index generic lattice planes $\{h,k,l\}$ and directions $\langle u,v,w\rangle$. Specific planes and zones are denoted with round and squre brackets, respectively. For hexagonal structures, four-number Miller-Bravais indices $\{h,k,-h-k,l\}$ are sometimes used to highlight symmetries in the **a-b** plane. The redundant third of four indecies may also be replaced with a dot.

The reciprocal lattice vector $\{h,k,l\}$ can be written as $ha^* + kb^* + lc^*$ if the reciprocal-lattice basis-vector are a^*, b^*, and c^*. For hexagonal crystals this may also be written in terms of the direct-lattice basis-vectors $\vec{a}, \vec{b}$ and $\vec{c}$ as

$$(hkl) = h\vec{a^*} + k\vec{b^*} + l\vec{c^*} = \frac{2}{3a^2}(2h+k)\vec{a} + \frac{2}{3a^2}(h+2k)\vec{b} + \frac{1}{c^2}(l)\vec{c}.$$

Hence lattice indices of the perpendicular to plane $\{hkl\}$ can be written, in suitably normalized form, as $\langle 2h+k, h+2k, l\frac{3}{2}(\frac{a}{c})^2\rangle$. Lattice directions for the same plane are sometimes also written with four indices as $\langle h,k,-h-k,l(\frac{3}{2})(\frac{a}{c})^2\rangle$ (Edington 1976). Because this latter convention mixes direct and reciprocal basis vector coefficients, we will avoid it where possible.

1.5. TARGETS OF THE THESIS

In this thesis, the work is focused on characterization and synthesis including carbon nanotubes and zinc oxide nanostructures. Using SEM and TEM, we try to understand the atomic structures of these nanostructures. More importantly, we want to understand the nanoscale material formation mechanisms, as this can be crucial for large scale manufacturing.

In chapter 2, we discuss synthesis process. According to our experimental results, we have gained a better understanding of nanostructure fabrication techniques. Here we mainly discuss the thermal evaporation method and the effect of experimental parameters on the final products, like source material temperature, substrate temperature, substrate material, and catalyst effects.

If we attach catalyst particles to nanotubes or rods, the orientation may affect catalytic activities. Hence the orientation relationship between catalyst particles and carbon nanotubes is important. In chapter 3, we will illustrate new strategies to determine this.

Various zinc oxide nanostructures have been synthesized at UM-St. Louis. Then atomic structure is investigated using high resolution scanning transmission electron microscopy. From this work, we try to understand the formation mechanism in chapter 4, when we discuss the relationship between catalyst and nanostructures.

From this work, we gain some new partial understanding but there remain many uncertainties. In chapter 5, we will discuss the difficulties and challenges, and illustrate with additional data.

2. ZINC OXIDE NANOSTRUCTURES AND SYNTHESIS TECHNIQUES

2.1. ZINC OXIDE NANOSCALE MATERIALS

Zinc oxide exists as a white powder, and also occurs as the mineral zincite in nature. Zinc oxide melts at about 1975ºC and has a hexagonal wurtzite structure with lattice constant a=3.2494 and c=5.2038 Angstroms, belonging to space group $P6_3mc$. Figure 1 shows a diagram of this structure. It is composed of two alternating layers of Zn^{2+} and O^{2-} atoms tetrahedrally bonded to each other. This structure is a non-centrosymmetric structure, with polarization along the c axis: a positively-charged Zn terminated surface (0001) and negatively-charged O terminated surface $(000\bar{1})$. This structure results in zinc oxide piezoelectricity, potentially usefully in nanogenerators (Wang et al. 2007b).

Zinc oxide is a promising wide band inorganic semiconductor, and has significant applications in optoelectronics (Huang et al. 2001a), photonics (Choy et al. 2003), and sensors (Govender et al. 2002). Zinc oxide is one of the richest morphologies in the inorganic semiconductor family (Wang et al. 2004b).

Various zinc oxide nanostructures have been fabricated including wires or rods (Gao et al. 2003a), belts (Pan et al. 2001), cages (Gao et al. 2003b), spirals (Kong et al. 2004b), rings (Kong et al. 2004a), and so on. These zinc oxide nanostructures have novel applications in optoelectronics, sensors, transducers and biomedical sciences (Tatsuyama et al. 1976; Jin et al. 1988; Wang 2004).

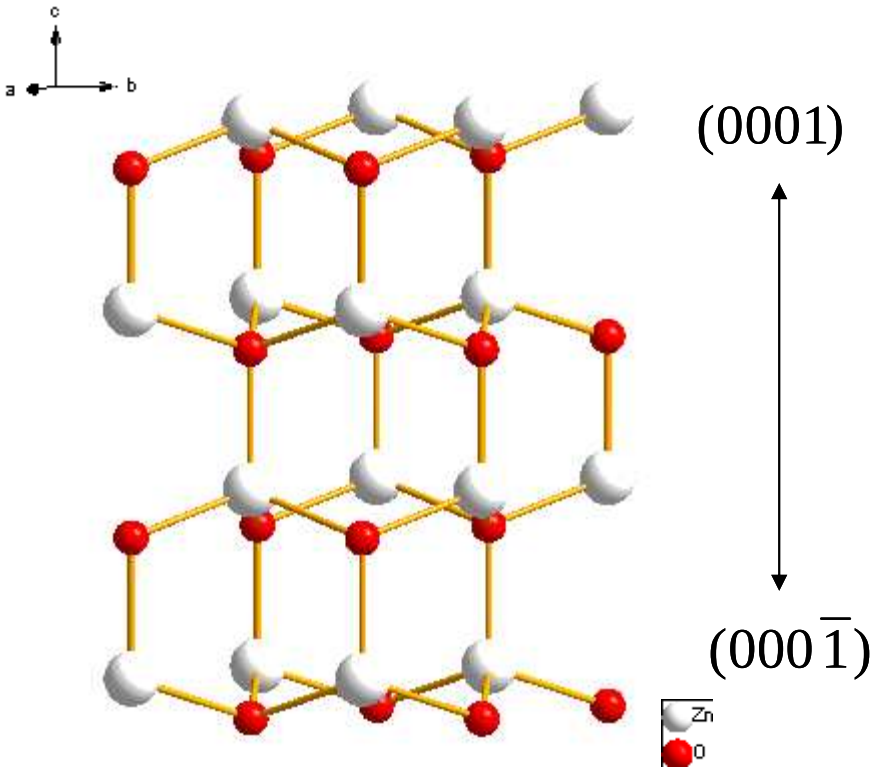

Figure 2.1 The diagram of zinc oxide structure using Diamond 3 software.

2.2. SYNTHESIS METHODS

Various methods have been used to synthesize zinc oxide nanostructures. These include catalytic growth via the vapor liquid solid mechanism, thermal evaporation, and wet chemistry processes. Among these synthesis methods, vapor evaporation is a simple and low cost method. Thermal evaporation is a process to vaporize source materials at certain temperature and condense the vapor phase source materials to form the desired products. The reactions take place in a horizontal tube furnace as shown in Figure 2, which shows the tube furnace, an alumina tube, a gas supply system, and a pumping system. The tube is sealed by Teflon stoppers. The carrier gas comes in from the left end of the tube and exhausts to the right end. Source materials are located in the center of the

tube furnace. All the substrates are loaded at the lower temperature zone downstream of the gas flow direction.

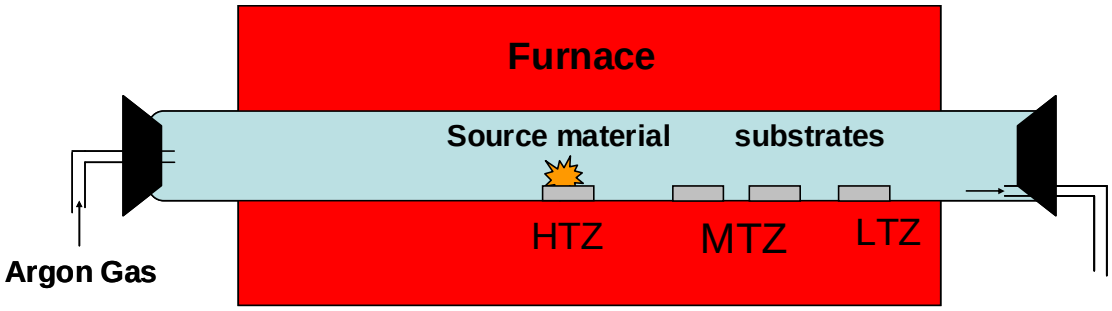

Figure 2.2 The diagram of the synthesis setup. HTZ, MTZ, LTZ mean high temperature zone, middle temperature region and low temperature region.

Several parameters including source material temperature, substrate temperatures, experimental time, total and partial pressure in the tube and gas flow rate control the final products (Dai et al. 2003).

The furnace temperature has been calibrated using a thermo couple as shown in the Figure below.

This temperature profile guides loading of the source material and substrates at specific temperature regions.

ZnO has a high melting point, but can be vaporized much lower than 1975ºC with the help of carbon black. At 1000ºC, ZnO reacts with carbon or carbon monoxide in the center of the furnace.

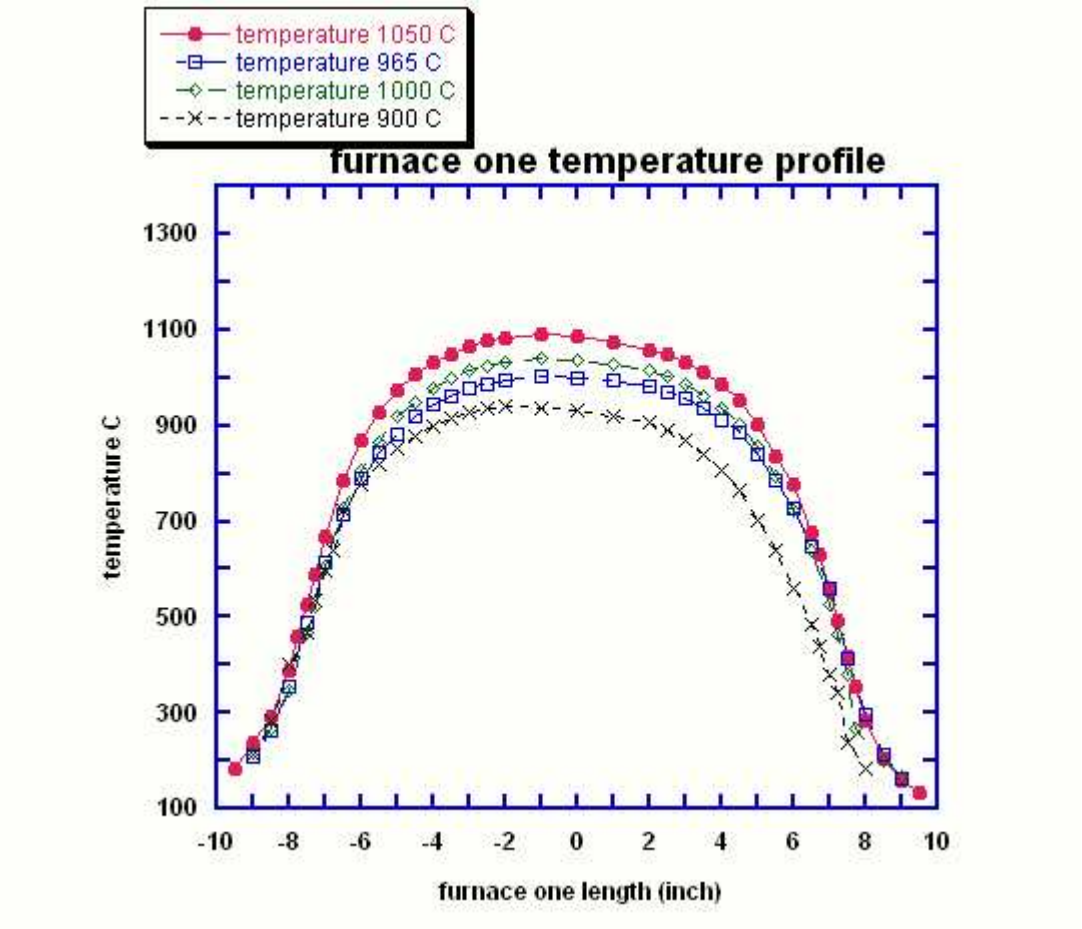

Figure 2.3 The tube furnace temperature profile distribution.

$$ZnO + C \rightarrow Zn + CO$$
$$ZnO + CO \rightarrow Zn + CO_2$$
$$ZnO + (1-x)C \rightarrow ZnO_x + (1-x)CO$$
$$ZnO + (1-x)CO \rightarrow ZnO_x + (1-x)CO_2$$

After the reaction, zinc and zinc oxide vapor move to cooler temperature zones with the carrier gas. Zinc vapor has this reaction with carbon oxides in the cooler temperature zones:

$$Zn + CO \rightarrow ZnO + C$$
$$2Zn + CO_2 \rightarrow 2ZnO + C \,.$$

2.2.1. Source temperature effect Source material temperature will determine source material vapor pressure. The vapor pressure increases exponentially with source material temperature (Ye et al. 2005). High source temperatures will result in more nanostructure growth on the substrates than low source temperatures. The size and shape of the final products structures will also change accordingly to source material temperature. The source material needs to be hot enough to evaporate. On the other hand, source vapor nucleates uniformly if a large amount of source material deposits simultaneously. Chen et al. report that there are no ZnO products at sintering temperatures below 900ºC. And at 1200ºC, zinc oxide powders tend to form. The optimum temperature is around 1100ºC, where the growth rate and resultant yield of nanostructures is best (Chen et al. 2004).

Different materials systems have different optimum parameter settings, including temperature. In order to find the optimum temperature to get uniformly distributed products, we tested our system using various temperatures. We put the same amount of commercial ZnO and carbon black (Alfa Aesar Company) into a crucible boat as source materials, and loaded them at the center of the tube furnace. Then we set the argon gas flow rate at 15 sccm (standard cubic centimeters per minute). The system is heated to final temperature with ramping rate at 30°C/minute. One experiment set final temperature at 1100°C, and the other experiment set it at about 1000°C. We kept the system at the temperature for about 1 hour, then cooled down the system naturally.

At 1100°C temperature, very differently shaped structures were synthesized as we moved from high to low substrate temperature regions, as shown in Figure 4.

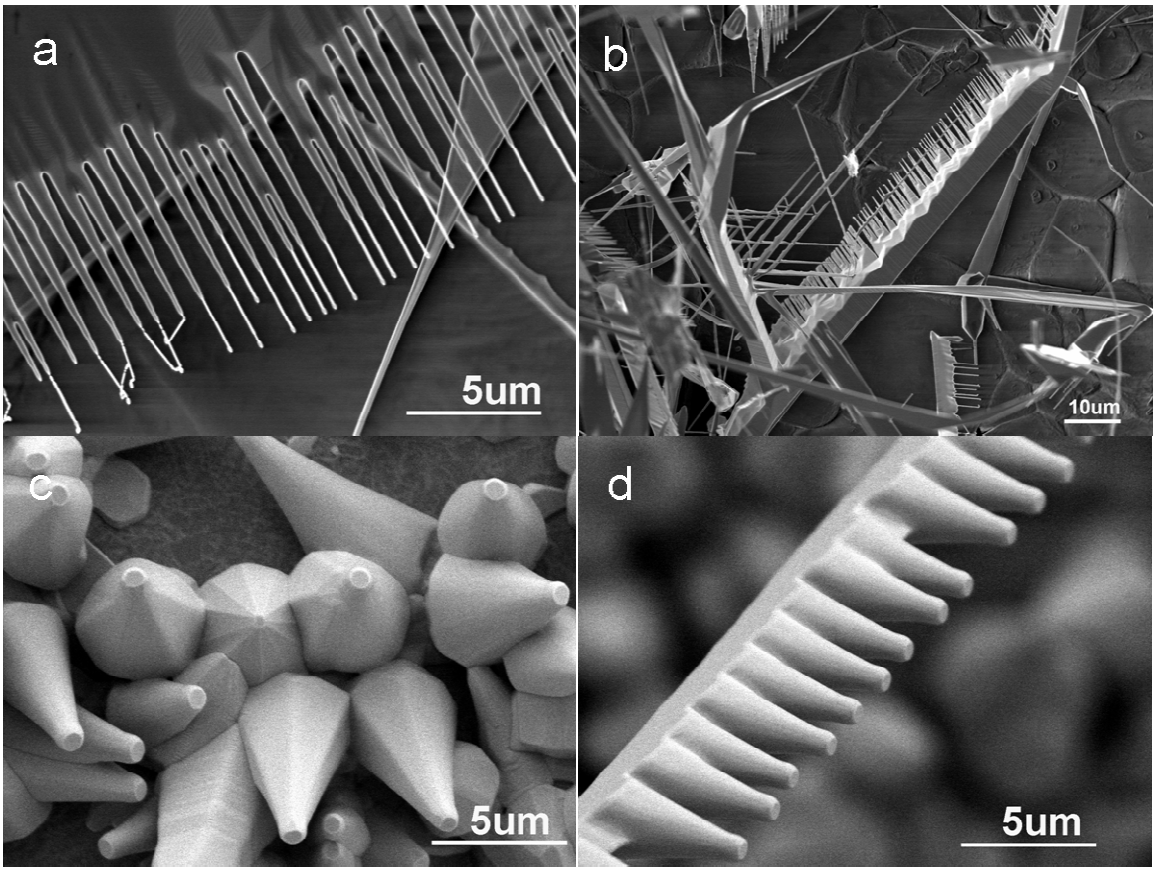

Figure 2.4 SEM image shows that zinc oxide cone and comb shapes products fabricated at source temperature of 1100°C. (a) and (b) were comb-shape structures formed at 900ºC region. (c) and (d) were hexagonal cone shape structures formed at 700ºC region (2007, J. Liu).

Under similar experiment conditions with the final temperature at 1000°C, we found that uniformly distributed zinc oxide nanowires nucleate in substrate temperature zone between 600ºC-800ºC.

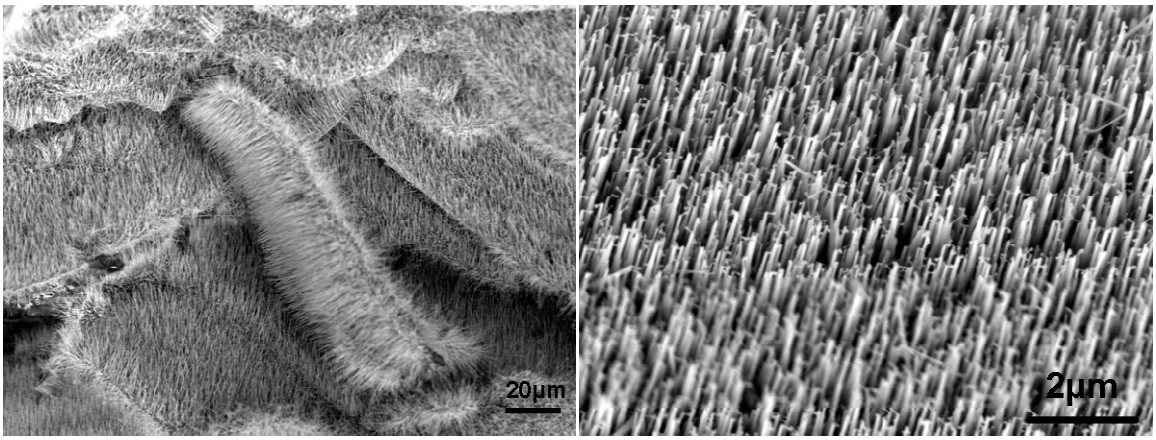

Figure 2.5 Low magnification and high magnification SEM images show uniform zinc oxide nanowires synthesized using 1000°C condition (2007, J. Liu).

2.2.2. Substrate temperature effect In different substrate temperature zones, different zinc oxide nanostructures are obtained in the same evaporation experiment. Such morphological evolution has been observed by several groups. Li reported that zinc oxide nanostructures change with substrate temperature. Nanoridges were reported at 900ºC. At 790ºC-850ºC region, well vertical aligned high density zinc oxide nanorods are observed at this region. At 650ºC-750ºC, an array of nanowall-nanorods junction is obtained. At 550ºC-630ºC, zinc oxide nanotips formed at this region. Below 550ºC, there is no clear crystal structures expect crystalline films are observed (Li et al. 2006). Umar (2007) reported zinc oxide morphologies evolution as well. At 470ºC-515ºC zone, pyramidal tower shaped zinc oxide nanostructures were reported. At 515ºC-555ºC zone, hexagonal faceted zinc oxide nanorods were found. At 555ºC-580ºC zone, zinc oxide nanowires attached to nanosheets are observed here.

ZnO morphological evolution is also shown in our experiments. Different experimental setups may have different temperature zones for these structures. In our system, we found that film structures were deposited around 900ºC-950º C. Nanobelts

were found in the 600ºC-850º C and nanowires were found below 600º C as shown in Figure 6. Of course, different gas flow rates will also have an effect on the structures at a given substrate temperature. Besides the substrate temperature, the heating rate may also influence the initial nucleation and hence the diversity of final products. Higher heating rates may also make the final products more homogeneous.

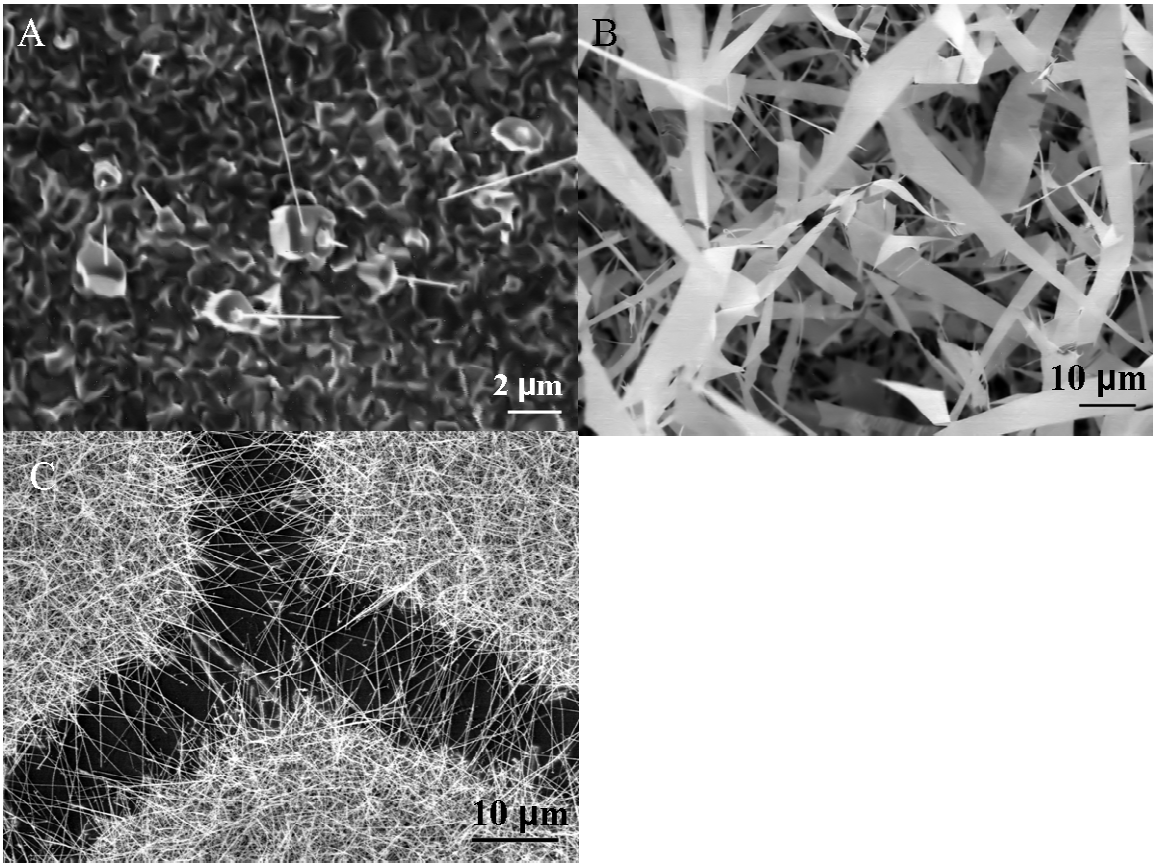

Figure 2.6 (A) ZnO film like structures form at 900°C-950°C region, (B) ZnO ribbon or belt shape structures nucleate at 600°C-850°C, and (C) ZnO nanowires form at temperature below 600°C.

2.2.3. Gas flow rate effect Chen et al. claimed that with a nitrogen gas flow rate of 70 sccm (standard cubic centimeter per minute), fine ZnO tetrapods grew on the inner wall of the quartz tube (temperature range of 950ºC-980ºC). When the flow rate of Nitrogen was turned to 90-100 sccm, ZnO nanowires were formed instead of tetrapods. The dark grey

Zn nanowires were formed as Nitrogen flow rate increased to 150 sccm or more (Chen et al. 2005). Kong et al. reported that ZnO nanowire diameters become bigger with higher gas flow rate (Kong et al. 2006). ZnS nanostructure morphologies are highly influenced by the gas flow rate. In the 850°C substrate region, higher gas flow rates were reported to increase the density of the nanowires. At 950°C, a large quantity of long ZnS nanowires formed at low gas flow rates. At 1050°C, ZnS nanoribbons were reported to widen with higher gas flow rates. At 1150°C, microparticle clusters along with nanoribbons were reported at low gas flow rates. On the other hand, there are only microcrystals without nanoribbons at high gas flow rate(Kar et al. 2005). In our experiment, film like structures form in the 900°C-950°C region, ribbon-like structures nucleate at 600°C-850°C, and nanowires form at below 600°C at a low gas flow rate (15 sccm). At a higher gas flow rate (30 sccm), similar structures are observed but it moved to lower temperature region.

2.2.4. Total and partial pressure effect Zinc and oxygen partial pressure are very important factors to affect final product morphologies. Atmospheric pressure chemical vapor deposition has proven to be a simple and cheap method to fabricate zinc oxide nanostructures. Local vapor pressure is the key for zinc oxide supersaturation. Excessive vapor precipitates on the substrate after supersaturation to form nanostructures. Supersaturation is determined by the vapor pressure. Zn, oxygen, CO, and ZnO_x vapor pressure decreases from the center of furnace to the end of the tube. Since Zn vapor is too low to nucleate at low temperature region and CO's reduction at high temperature region ZnO forms nanoparticles better in intermediate temperature zone. Oxygen vapor is essential to allow zinc to deposit on the substrates as zinc oxide, instead of as metal only.

High local oxygen partial pressure will promote $\langle 10\bar{1}1\rangle$ growth of zinc oxide nanostructures (Mahmud et al. 2006). Oxygen partial pressure also affects the number density of zinc oxide nanorods. When oxygen pressure is around 2×10^{-2} Torr, nanorods have the maximum abundance (Yan et al. 2003). If oxygen pressure is lower than 2×10^{-2} Torr, oxygen mainly works on the substrate surface in order to make zinc nucleate and deposit on the substrates. If oxygen pressure is higher than 2×10^{-2} Torr, rod density decreases due to the lack zinc ions since zinc has deposited on the substrates. Zhang et al. (2004) reported that various zinc oxide nanostructures obtained at different pressure. They changed in order of nanorods, nanowalls, and nanotubes with a decrease in pressure from 10 Torr, 0.3 Torr, to 0.06 Torr. At one atmosphere pressure without any gas flow, various structures formed at different points along the path, from the source material location to the open end of the tube. Zn, ZnO_x, and CO_x vapor pressures decrease from the source gradually to the open end. Of course from the center of tube to end of tube, temperature also decreases gradually. Nanowires, nanobelts, and nanofibers form along the temperature and vapor pressure decreasing direction (Chen et al. 2004). For iron oxide nanostructures, the literature has reported that iron oxide nanocluster sizes increase with increasing pressure (Nakayama et al. 2000). In our experiment, we used one atmosphere pressure to synthesize ZnO nanostructures. From the center of the tube to the end of the tube, film-like structures, ribbon-like structures and wire-shaped structures form along the gas pressure decreasing direction.

2.2.5. Substrate material effect Various substrates have been used for ZnO nanostructure synthesis, including sapphire (Yang et al. 2002), GaN (Fan et al. 2006), ZnO coated film silicon substrate (Ye et al. 2005; Ye et al. 2007), NiO coated silicon

(Kim et al. 2004), glass (Sreenivas et al. 2005), Al_2O_3 (Gao et al. 2003a), gold coated silicon (Chen et al. 2004), and even fresh silicon substrates (Khan et al. 2007). In most cases, the nanostructures alignments are determined by lattice matching between zinc oxide and the substrates. Several substrates have been shown to allow epitaxial growth of zinc oxide nanowires, such as sapphire (Yang et al. 2002), GaN (Fan et al. 2006), and ZnO coated substrates (Ye et al. 2007). The lattices of these substrates match with zinc oxide in certain crystallographic directions. Sapphire has only 0.08% mismatch with zinc oxide's (0001) plane. GaN has about 1.9% mismatch with the zinc oxide's (0001) plane. ZnO matches with itself very well. Substrates thus may have significant impact on the orientation of nanostructures.

In our experiment, we used silicon and mica substrates to grow ZnO nanowires using the same conditions. ZnO nanowires are observed at the same substrate temperature region. On the silicon wafer, zinc oxide nanowires are randomly oriented. On the mica substrate, aligned zinc oxide nanowires are observed. On mica randomly oriented nanowires are found in lower temperature zones than the aligned nanowires.

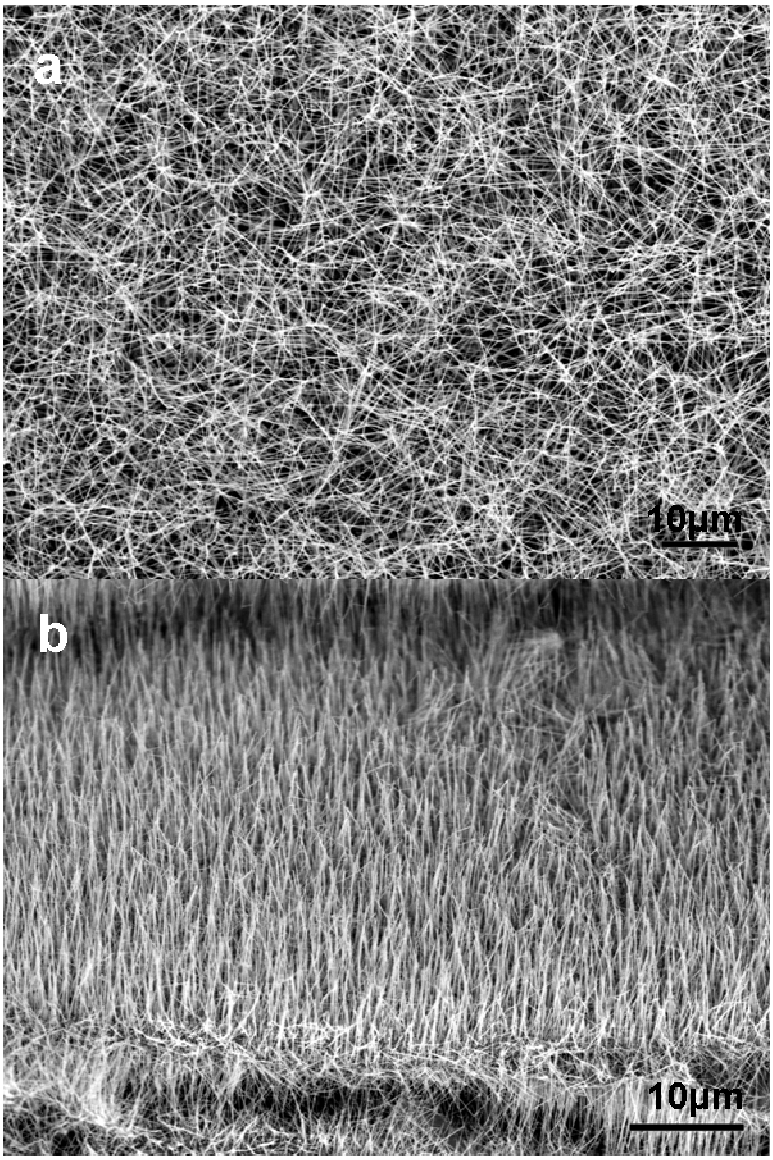

Figure 2.7 SEM image (a) randomly oriented ZnO nanowires on (100) silicon wafer substrate. (b) Aligned ZnO nanowires nucleate on mica substrates.

2.2.6. Catalyst effect Catalysts are very important for the vapor deposition mechanism including controlling the zinc oxide nanowire orientations, alignments, and precise locations. A vapor liquid solid growth mechanism is proposed to explain catalyst assisted ZnO nanowires' growth. Various catalysts have been used and achieved similar results

such as Au (Huang et al. 2001a; Wang et al. 2005), Sn (Wang et al. 2004a), Cu and Au (Li et al. 2004), and Au/Pt (Andreazza-Vignolle et al. 2006). The alloy droplet forms at the catalyst site. Then ZnO nanowires nucleate and push the catalysts up with the tip of the growing wire. Nanobelts and nanowires can be observed in the literature even without help of any catalyst following a vapor solid growth mechanism. $<0001>$ is preferential growth direction of nanowires, and $<10\bar{1}0>$ is the preferential growth direction of nanoribbons. The size of catalyst particles may control the diameter of ZnO nanowires (Pan et al. 2001; Ye et al. 2007).

From our experimental results, we find that the catalyst does have significant influence on the morphology of nanostructures.

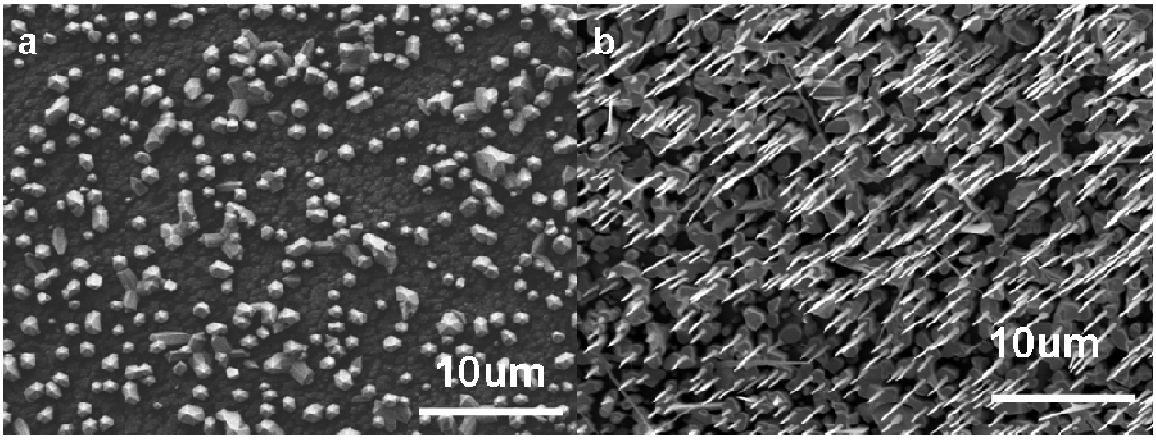

Figure 2.8 (a) ZnO particles nucleate on the catalyst-free substrate; (b) Under the same experimental condition ZnO wire-like structures form on a tin catalyst substrate.

In particular, we used one catalyst free substrate and one tin catalyzed substrate in the same experiment. Very different structures form on these two different substrates as shown Figure 8. The catalyst has an impact on the substrate's capacity to absorb source vapor, i.e. on its absorption coefficient. Clean substrates without any catalyst absorb

limited source vapor. Catalyzed substrates absorb larger amounts of source material, to better nucleate nanowires.

Table 2.1 Synthesis parameters of different ZnO nanostructures in our system.

Source material	ZnO+C	ZnO+C	ZnO+C	ZnO+C	ZnO+C
Source material temperature	1000ºC	1000ºC	1000ºC	1000ºC	1000ºC
Substrate material	Silicon	Mica	Au particles on mica	PdAu particles on mica	Sn film on mica
Substrate temperature	550ºC-800ºC	550ºC-800ºC	550ºC-800ºC	550ºC-800ºC	550ºC-800ºC
Gas flow rate	55 sccm (standard cubic centimeter per minute)	55 sccm (standard cubic centimeter per minute)	per minute)	55 sccm (standard cubic centimeter per minute)	55 sccm (standard cubic centimeter per minute)
Products	Random nanowires	Nanocastles	Aligned nanowires	Aligned nanowire	Nanoribbon

2.2.7. Oxygen effect We intentionally keep the system in an argon gas environment to minimize unwelcome oxygen in our experiment. In some experiments, the presence of oxygen by design affects the final structures. Kodambaka et al. (2006) reported that uniform silica nanowires were grown with the controlled oxygen because of the oxidization of the silicon nanowire surface. The preferred growth direction was achieved since the sidewall energies were changed. Tseng et al reported that ZnO nanorod diameters increased with the high oxygen gas flow rate. The ZnO crystallinity was also

affected (Tseng et al. 2003a). We did not observe these experimental phenomena in the absence of oxygen.

Source material temperature, substrate material temperature, substrate material, catalyst, total and partial gas pressure are parameters that need to be considered in our experiment. There are four essential stages in this system, which includes generation of precursor atoms or molecules, transport from source to substrate, adsorption on substrate surface, plus nucleation and growth of nanostructures.

2.3. CRYSTAL GROWTH THEORETICAL BACKGROUND

Theories about nano crystal growth have been developed by many groups, including the famous BCF theorem (Burton, Cabrera and Frank theorem) and Sears et al (Burton et al. 1949; Burton et al. 1951; Sears 1955) in the past half century. The crystal's final shape is determined by the Wulff theorem, at equilibrium condition, since the crystals are bound with surface planes with minimum total surface free energy (Herring 1951). The hexagonal-shaped tip of zinc oxide nanorods' helps to prove the Wulff theorem.

Wagner and Ellis (1964) proposed the vapor liquid solid growth mechanism for silicon whisker growth. In their silicon whisker synthesis experiment, they reported that BCF screw dislocations were not present. Gold particles instead worked as a sink in the experiment, to absorb arriving silicon atoms and form Au-Si alloy. The alloy became droplets at 950ºC. The $<111>$ silicon whiskers grew after the silicon was supersaturated. This theory is a common mechanism of semiconductor nanostructure growth, especially nanowire's growth including GaAs and InAs whiskers (Hiruma et al. 1995), silicon

nanowires and indium phosphide nanowires (Duan et al. 2000; McIlroy et al. 2004). Figure 2.9 illustrates the vapor liquid solid growth mechanism. Various metal nanoparticles have been used as catalysts in nanoscale materials synthesis. The key point in the process is that metal catalysts like Au, Ni, Co, Fe, get involved in the experiment. The whole process of the experiment includes three steps: dissolution of the deposited source vapor in the metal or alloy droplets, saturation or supersaturation of the deposition materials in these liquid droplets, and precipitation of the solid source materials along the growth direction. The catalyst particles control structure formation location, size, and orientation (Morales et al. 1998; Yang et al. 2002).

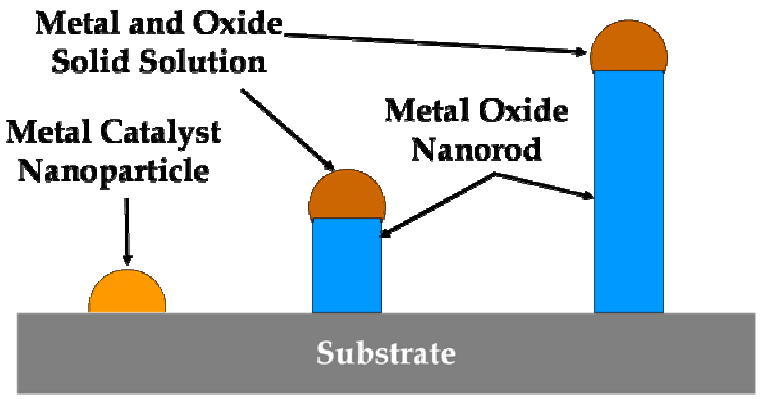

Figure 2.9. Schematic diagram illustrates that vapor-liquid-solid aligned growth of metal oxide nanowires, via the use of metal nanoparticles as catalysts for nucleation and growth of nanostructures.

Another formation mechanism is proposed for the catalyzed grown nanostructures. Persson et al. (2004) reported that solid phase diffusion was observed by in situ transmission electron microscopy during the synthesis of GaAs nanowire experiment. From the XEDS data, vapor-solid-solid (VSS) was proposed for gold catalyzed nanowires growth. Dick et al. (2005) later found that VSS growth mechanism was also

proposed for gold catalyzed III-V semiconductor nanowires synthesis. Kirkham et al. (2007) reported solid gold nanoparticles as catalyst for growing aligned ZnO nanowires recently. The vapor-solid-solid growth mechanism is also seen in our experiment. We will discuss more in chapter 4. The choices of vapor-liquid-solid or vapor-solid-solid mechanisms depends on the catalyst selection (Zhang et al. 2007).

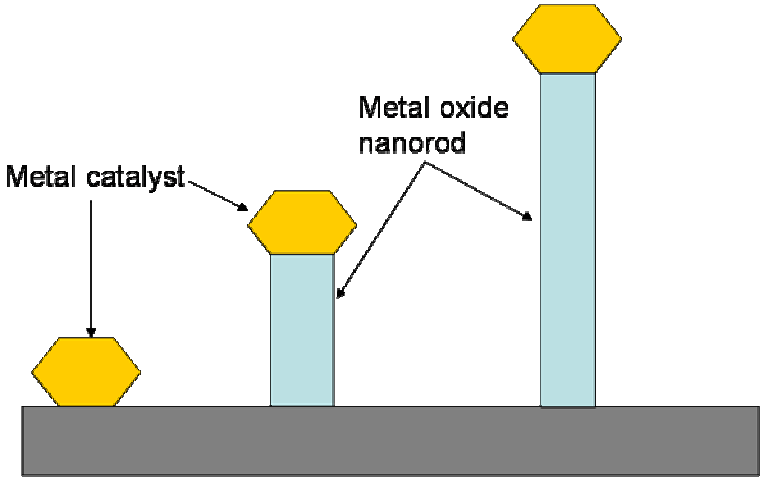

Figure 2.10 Schematic diagram illustrates that the metal oxide nanowires via vapor-solid-solid mechanism.

If the substrates have no catalyst particles in the experiment, the as-synthesized nanostructure formation mechanism is via vapor solid (VS) mechanism. Source atoms nucleate on the substrate surface and form nanocrystallites. After absorbing more source atoms, the nanocrystallites form the smallest surface energy shape (Kast et al. 2007).

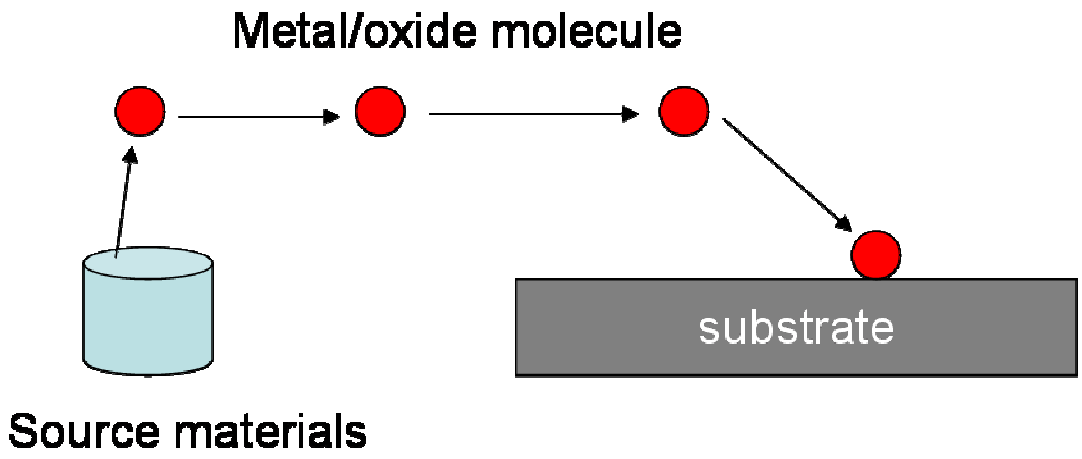

Figure 2.11 Schematic illustrates that metal oxide nanostructures form on the substrate directly via vapor solid mechanism.

2.4. RESULTS ON VARIOUS MATERIAL SYSTEMS

In this chapter, we discussed zinc oxide nano-synthesis techniques using thermal evaporation. Due the high zinc oxide melting temperature, carbon black is used to decrease the experimental temperature. In the system, source material temperature, substrate temperature, vapor pressure, substrate material, substrate catalyst, and gas flow rate will have a direct impact on the final structures size and shape. Under the different experimental conditions, nanostructures are formed via vapor-liquid-solid, vapor-solid-solid, and vapor-solid mechanism.

In our experiment, we used carbon black and zinc oxide powder mixtures as source materials. The source material temperature was set 1000ºC. Substrates were located in the 550ºC-850ºC region. Various different substrates were used, and resulted in different zinc oxide nanostructures. Argon gas was used as carrier gas. The whole system was kept at one atmosphere pressure.

The first structures were aligned zinc oxide nanowires. We used Au particle coated mica as our substrates. Figure 2.12 is the SEM image of gold particles. Au particle size distribution is shown in Figure 2.13.

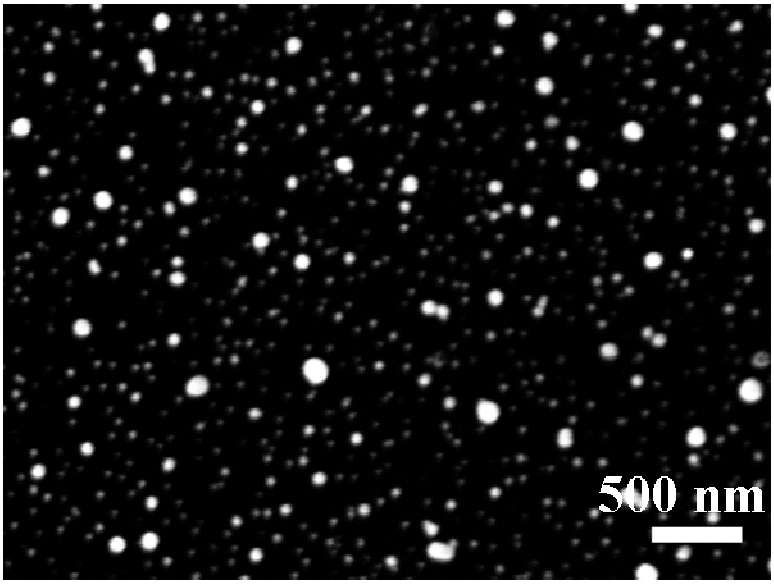

Figure 2.12 SEM image of gold particle.

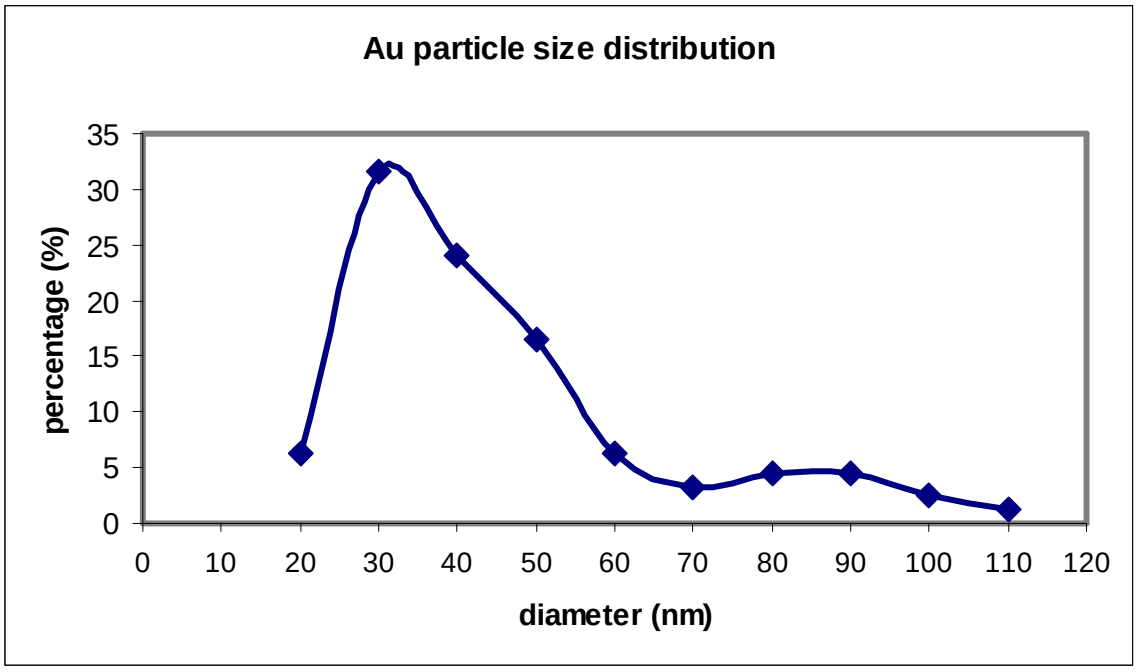

Figure 2.13 Gold particle size distribution.

From the size distribution, we find that most of the gold particles are below 100nm in diameter. Aligned zinc oxide nanowires were found at substrate temperature 650ºC-800ºC region. Figure 2.14a shows backscattering SEM image of aligned growth zinc oxide nanowire. The diameter of the nanowire is around 30nm. The size is consistent with the gold particle size distribution as shown above. The length of the nanowires is around few micrometers. They have the similar orientations. From the image we can find gold particles on the tip of the nanowires. Some of the nanowires have kinked tips, which may be caused by at the end of the experiment small amount of source vapor deposits on the gold particles. Randomly orientated zinc oxide nanowires were found at substrate temperature below 600ºC, with 30nm in diameter and few hundred micrometers in length as shown in Figure 2.14b.

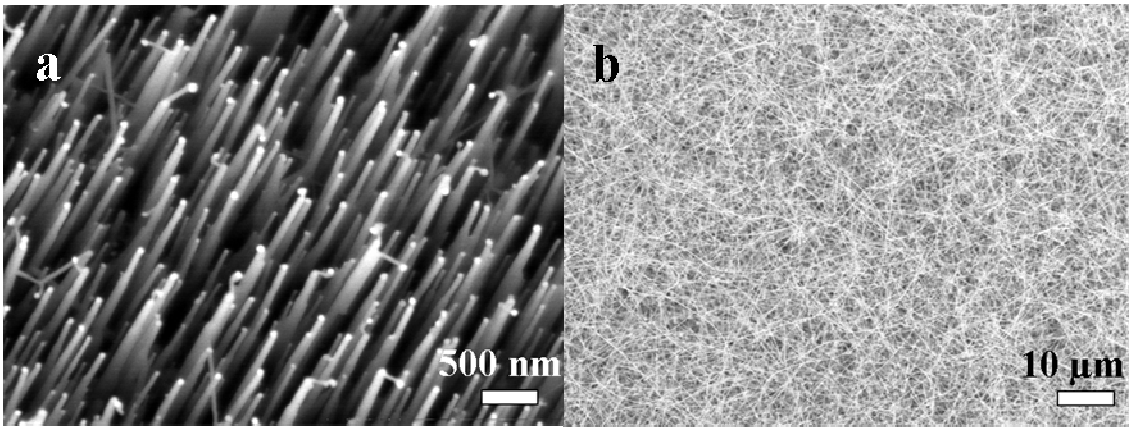

Figure 2.14 (a) Aligned zinc oxide nanowires with gold particles on the tip at substrate temperature 600ºC-850ºC (2007, J. Liu). (b) Randomly orientated zinc oxide nanowires were found at substrate temperature below 600ºC.

In order to investigate the relationship between gold particle size and zinc oxide nanowire diameter, we measure the gold particle and zinc oxide nanowire diameter. The diameter distribution of gold particles and zinc oxide nanowires can be seen in Figure 2.15. Most gold particles are around 30nm in diameter. Most of zinc oxide nanowire

diameters are 50nm or 70nm. Measurements of gold and zinc oxide nanowire diameter on some individual wires, in both TEM (red) and SEM (blue), are shown in Figure 2.16. As you can see gold diameter has simple relationship with zinc oxide diameter.

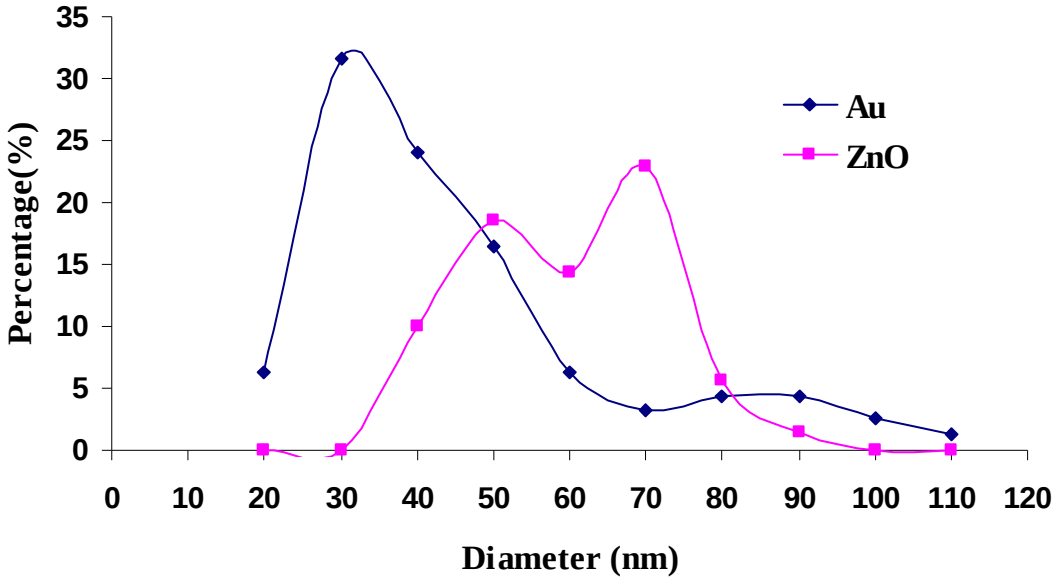

Figure 2.15 Gold and zinc oxide nanowire diameter size distribution.

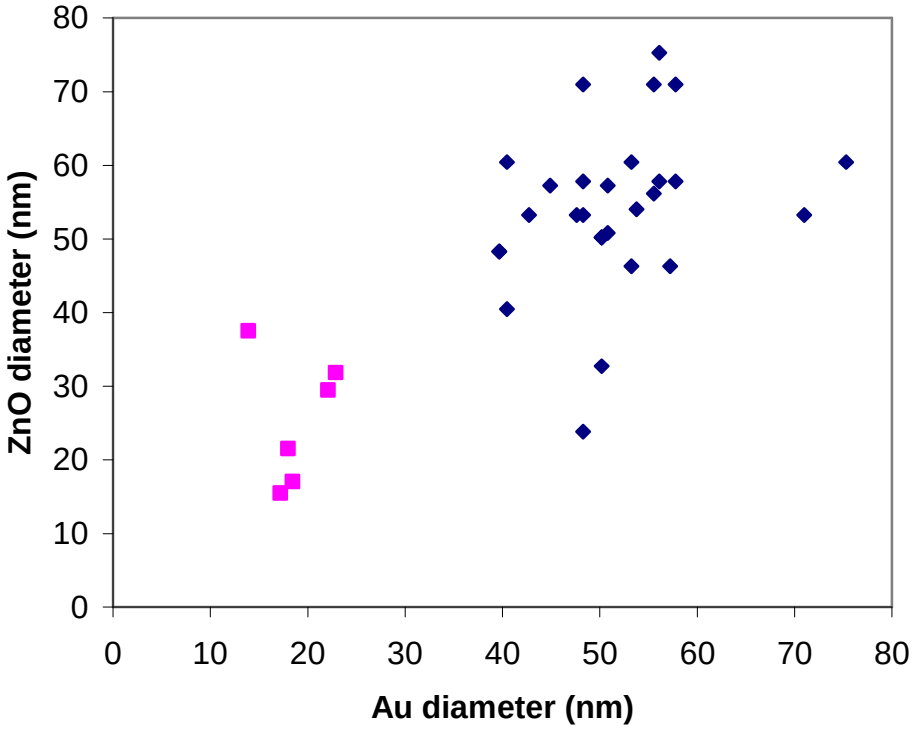

Figure 2.16 Correlation between gold and zinc oxide diameter on individual wires.

Scanning transmission electron microscopy imaging of ZnO nanowires is present in Figure 2.17. Au particles have faceted surfaces and are located at the growth front. Gold particles are brighter in darkfield images because of their high atomic number. The diameter of the nanowire is around 30nm, which is consistent with SEM results.

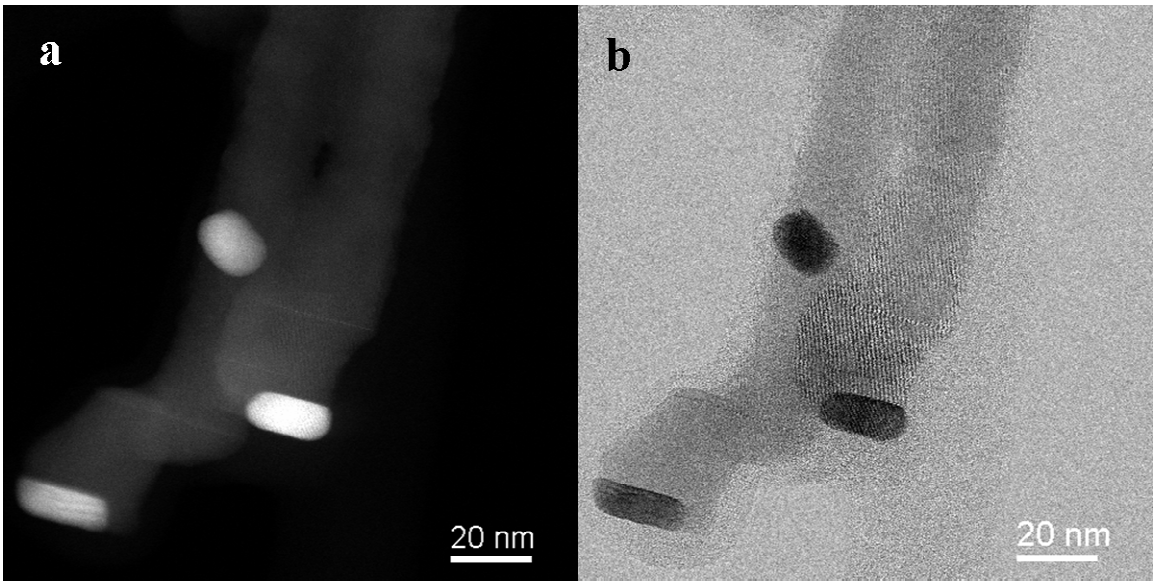

Figure 2.17 Low magnification STEM images of Au-ZnO nanowire image. (a) High angle annular darkfield (HA-ADF) image. (b) The corresponding bright field image (2007, J. Liu).

A high resolution STEM image presented in Figure 2.18 shows that the ZnO nanowire grows along $<00.1>$. The interface between the Au particle and the ZnO nanowire is atomically sharp. On the basis of the image information, the side surfaces of the gold particles are defined to be $\{111\}$ facing the zinc oxide, $\{002\}$ perpendicular to that with the electron beam direction down $<\bar{1}10>$. The perpendicular side surface of the ZnO nanowire is $\{10.0\}$ with the beam direction down $<01.0>$. The detailed structure relationship between gold particles and zinc oxide nanowires is investigated in chapter 4.

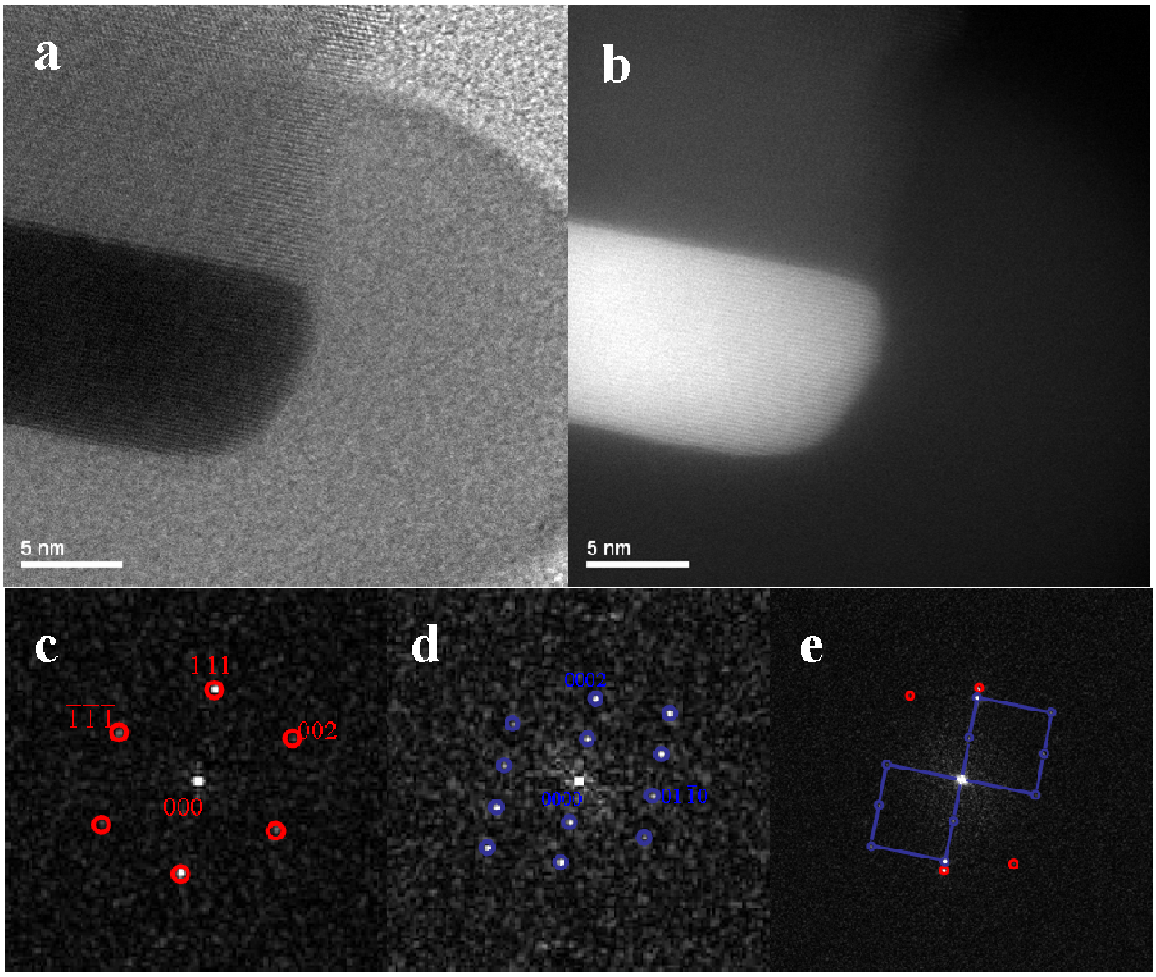

Figure 2.18 (a) The bright field STEM image of the gold catalyzed zinc oxide nanowire. (b) Darkfield STEM image of the same sample (2007, J. Liu). (c) The FFT pattern of gold particle part. (d) The FFT pattern of zinc oxide nanowire part. (e) The FFT pattern of the whole image.

The second catalyst we used is Pd/Au alloy, using the similar experimental parameters as the first one. Figure 2.19 is an SEM image of a Pd/Au particle. Figure 2.20 is the particle diameter size distribution. Most of the particles are around 40-80nm in diameter.

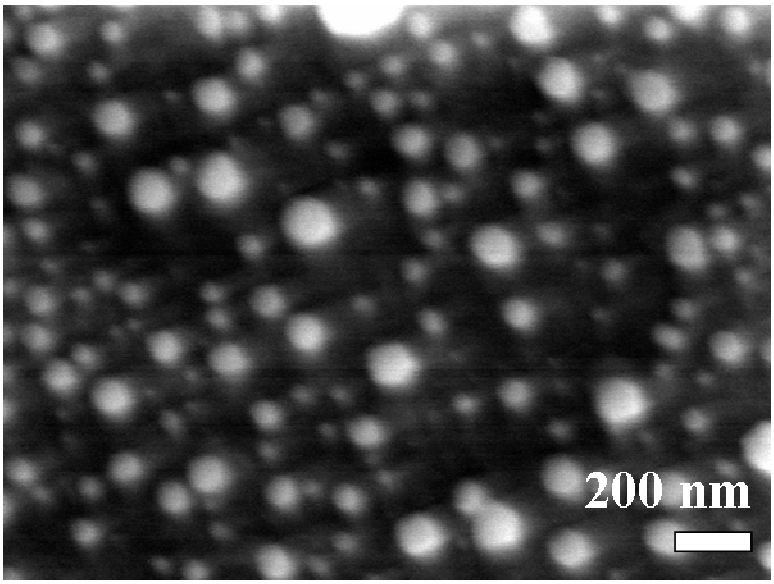

Figure 2.19 SEM image of Pd/Au catalyst particle.

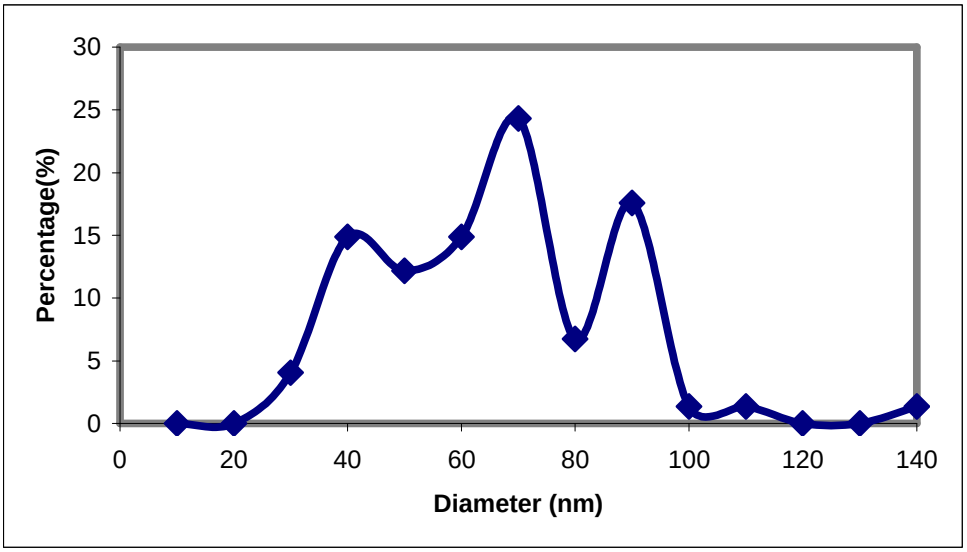

Figure 2.20 Pd/Au alloy particle size distribution.

After one hour experiment, we found aligned of zinc oxide nanowires beneath the Pd/Au catalyst. Aligned zinc oxide nanowires were found at a substrate temperature around 600ºC-850ºC. The diameter of the nanowire is around 50nm, with the length a few micrometers as shown in figure 2.21a. The kinked tips were found again in this case.

Randomly oriented zinc oxide nanowires were found at substrate temperature below 600ºC. The diameter of these nanowires is around 50nm, and the length is few hundred micrometers.

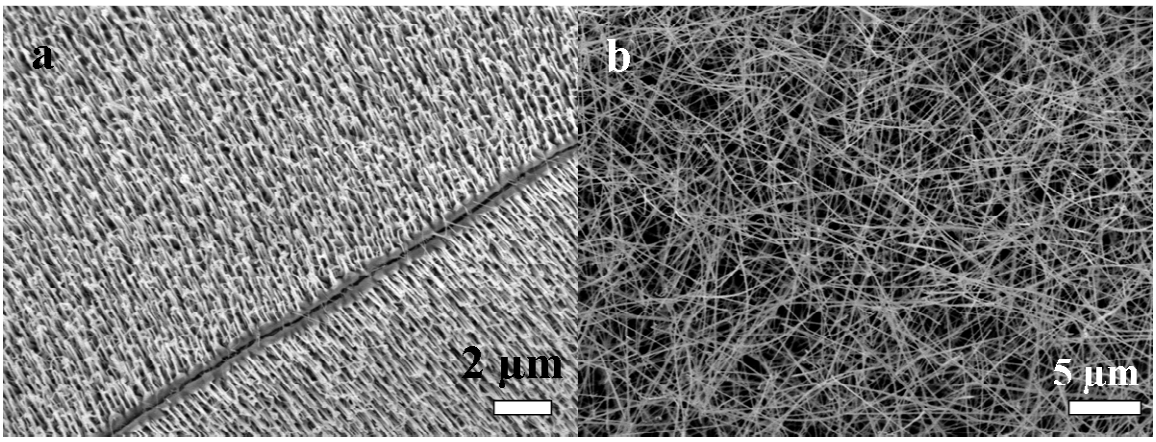

Figure 2.21 (a) Aligned zinc oxide nanowires with Pd/Au particles on the tip at substrate temperature 600ºC-850ºC. (b) Randomly oriented zinc oxide nanowires were found at substrate temperature below 600ºC.

Low magnification STEM images obtained for PdAu catalyzed ZnO nanowires are shown in figure 2.22. The faceted PdAu particle is located on the tip of the nanowire. The particle is brighter than the ZnO nanowire in darkfield since the PdAu alloy has a bigger atomic number than ZnO. The diameter of the nanowire is around 30nm.

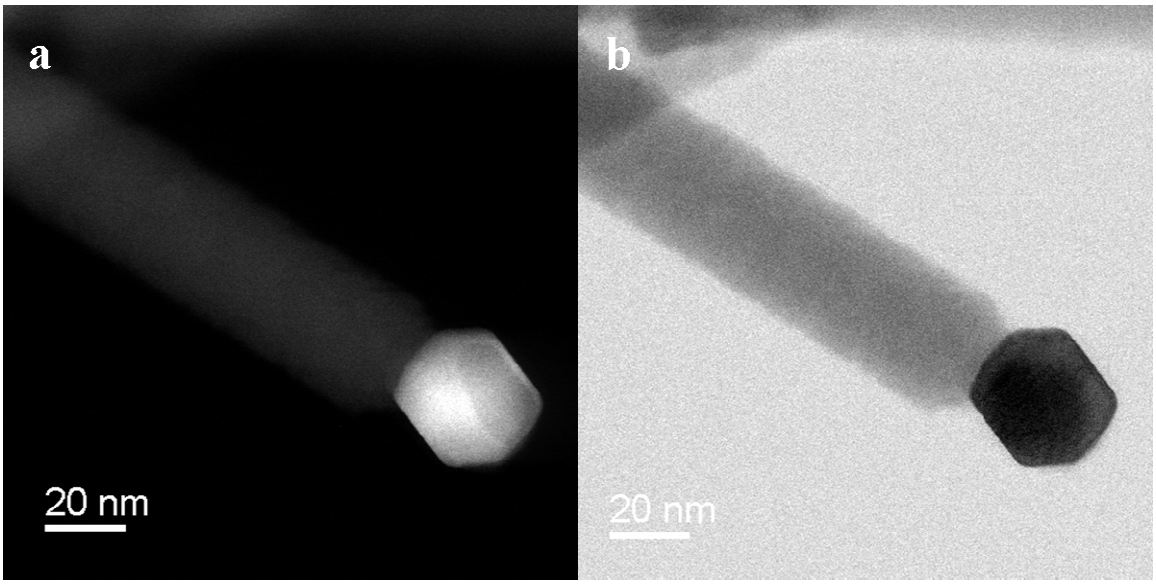

Figure 2.22 Low magnification STEM images of PdAu-ZnO nanowire image. (a) High angle annular darkfield (HA-ADF) image. (b) The corresponding bright field image (2007, J. Liu).

Nanoscale energy dispersive X-ray spectroscopy (EDS) analysis was conducted to investigate the chemical element information as shown in figure 2.23. The spectra were obtained from different areas of the PdAu particle and ZnO nanowire. Spectra from PdAu suggest that there was no Zn signal. No Pd or Au peak was found in the zinc oxide nanowire portion either. The tin peak comes from the Ti TEM grid. Several different nanowires confirm the result.

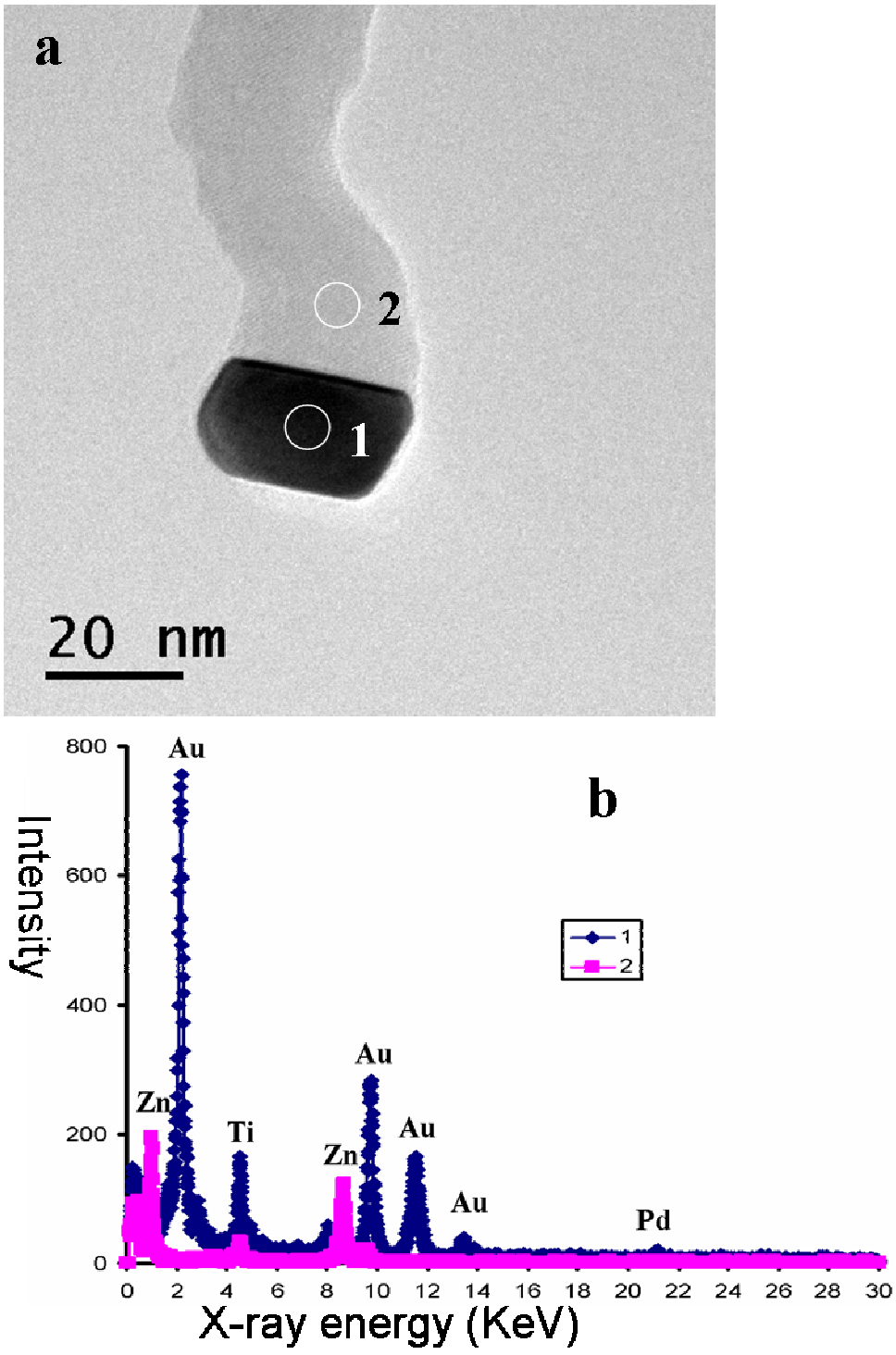

Figure 2.23. Low magnification TEM image (a) shows a nanoparticle located at the tip of a ZnO nanowire. EDS spectra (2007, J. Liu) (b) show the element information on different locations. Location 1 is mainly at PdAu particle position. Location 2 is located at ZnO nanowire. (Ti peak comes from the Ti TEM grid). 2 has Zn peak without apparent PdAu peak.

The third catalyst we used is tin. We used the same experimental parameters as previous experiments. We used an evaporator to coat the tin particles on mica substrates. Figure 2.24 shows mica substrate with tin particles. The particle size is around 100nm in diameter. Using the same experimental parameters, we get zinc oxide nanobelts at 600ºC-850ºC region. The nanobelts were nucleated at tin catalyst region only as shown in figure 2.25a. From the high magnification SEM image, we found that the belt-shaped structures are about 2 micrometers in width, about 10 micrometers in length, and less than 100nm in thickness. In our experiment, we also observed that the catalyst thickness had an impact to the structures, as discussed in chapter 4.

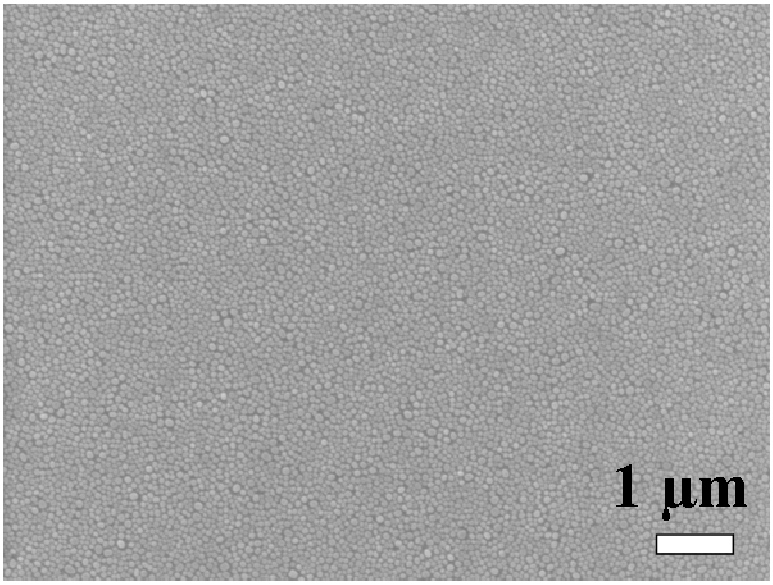

Figure 2.24 SEM image of tin catalyst particle.

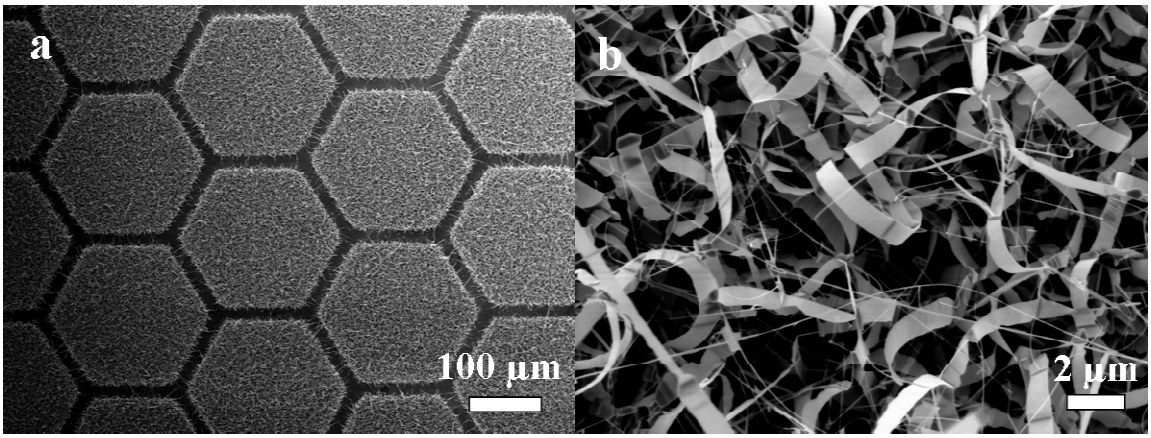

Figure 2.25 (a) Low magnification SEM image of tin catalyzed zinc oxide nanobelts with TEM grid as mask. (b) High magnification SEM image of zinc oxide nanobelts (2007, J. Liu).

High resolution scanning transmission electron microscope images reveal that the zinc oxide nanobelts are single crystals without extended defects, as shown in figure 2.26. The nanobelt grows along $\{10.0\}$ direction, with the top and bottom flat surface $\pm\{11.0\}$, and side surface $\pm\{00.1\}$, as illustrated in the diagram 2.27.

In this chapter, we mainly discussed our experimental result with different substrates. Aligned zinc oxide nanowires, randomly oriented zinc oxide nanowires and zinc oxide nanobelts have been synthesized successfully in our experiments. Table 2.2 summarizes the different nanostructure formation temperatures, lengths, diameters and number densities.

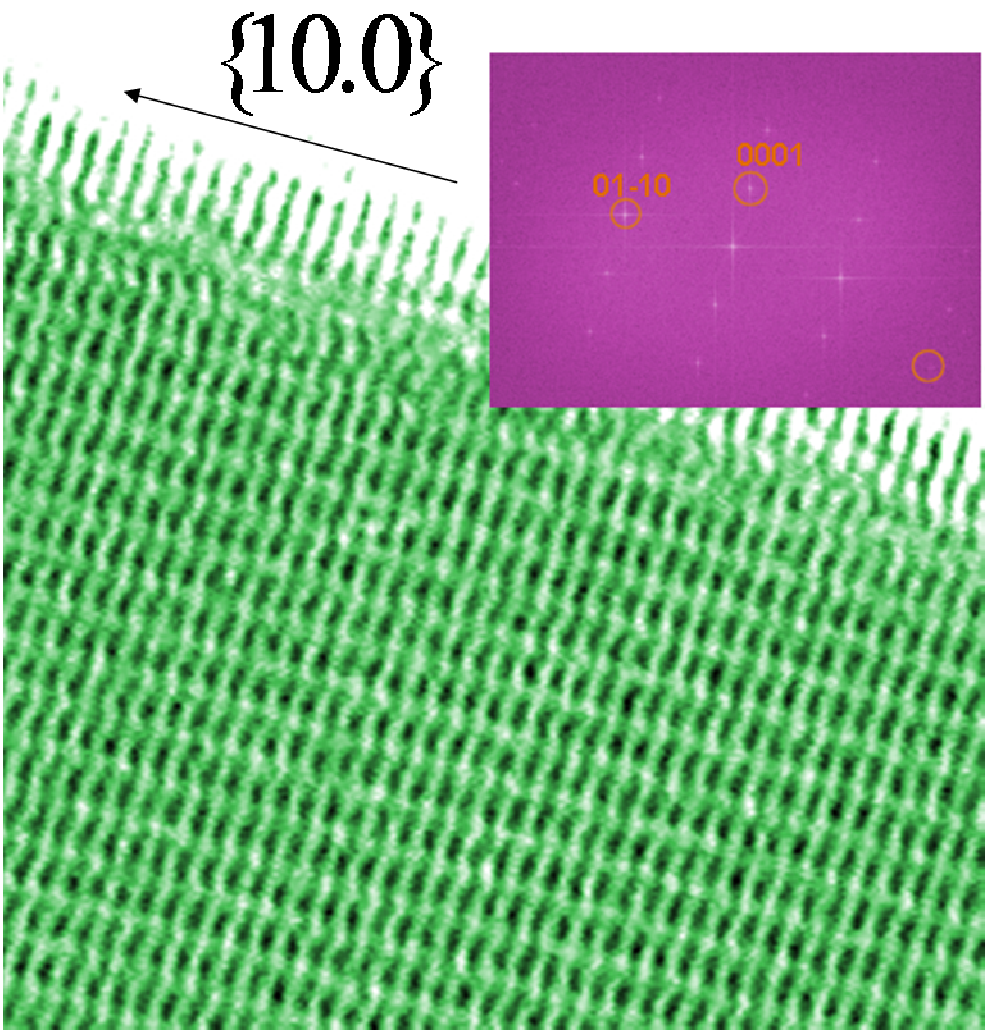

Figure 2.26 High resolution transmission electron microscope image of zinc oxide nanobelt. The inset shows that zinc oxide grows along the {10.0} direction (2006, P. Fraundorf).

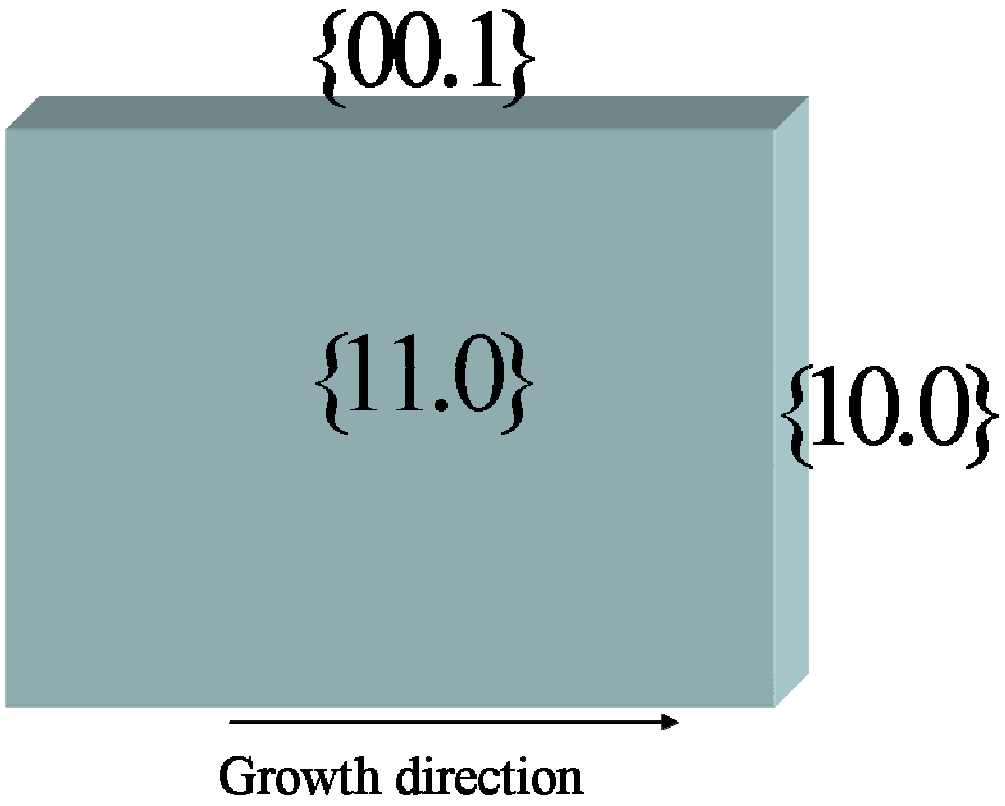

Figure 2.27 ZnO nanobelt diagram.

Table 2.2 Comparison of zinc oxide nanostructures length, width, formation temperature and number density.

Nanostructures	Number density (per cm^2)	Length	Width	Substrate Temperature
Aligned Au-ZnO nanowires	$10^{10} - 10^{11}$	1µm-10µm	20nm-100nm	600ºC-850ºC
Randomly orientated Au-ZnO nanowires	$10^{8} - 10^{10}$	100µm-1000µm	20nm-100nm	Below 600ºC
Aligned PdAu-ZnO nanowires	$10^{10} - 10^{11}$	1µm-10µm	20nm-100nm	600ºC-850ºC
Randomly orientated PdAu-ZnO nanowires	$10^{8} - 10^{10}$	100µm-1000µm	20nm-100nm	Below 600ºC
Tin catalyzed zinc oxide nanobelts	$10^{6} - 10^{7}$	2µm-10µm	1µm-2µm	600ºC-850ºC

PAPER
1. LATTICE FRINGE SIGNATURES OF EPITAXY ON NANOTUBES

1.1. INTRODUCTION

Direct methanol fuel cells are regarded as potential mobile power sources because of the high energy density, easy operation, and their simple fuel supply (Chien et al. 2006). Pt on carbon black is recognized as a promising electrode material for low temperature fuel cells. Carbon black is used as support for fuel cell catalysts because of the electronic conductivity and surface area (Liu et al. 2004). Pt reduces oxygen in a fuel cell, to solve the catalyst poisoning problems caused by CO and other intermediates under low temperature reaction conditions. In order to increase activity and the efficiency of the catalyst, a new support is needed to replace carbon black. Carbon nanotubes are recently used as new supports for metal catalysts due to their small size, high chemical stability and large surface area to volume ratio (Ye et al. 2003; Xing et al. 2004). Carbon nanotubes decorated with metal catalyst particles combine properties of the two nanomaterials to get wider applications (Qu et al. 2006; Wildgoose et al. 2006; Ye et al. 2006). Also Pt nanoparticles on carbon nanotubes have generated higher maximum power density than Pt on carbon black (Li et al. 2003c). Various methods have been used in loading Pt or other metal catalyst particles on the carbon nanotube surface, including impregnation and chemical reduction, and electro deposition (Prabhuram et al. 2003; Liu et al. 2004; Vinodgopal et al. 2004). These synthesis methods provide uniformly dispersed particles on the carbon nanotubes.

Metal particles on the exterior of the carbon nanotubes have relatively more access to reactant molecules than interior particles. Thus loading the particles on the outer

wall of carbon nanotubes is preferred in most catalyst reactions. Good adhesion of the metal nanoparticles to carbon nanotubes is a key factor to determine the catalytic performance in methanol oxidation and oxygen reduction (Ye et al. 2003). The lattice relationship between metal catalyst nanoparticles and nanotube supports may affect their adhesion. Understanding this relationship will help us to design products whose properties are optimized (Han et al. 2004a). Transmission electron microscopy (TEM) is a tool that can analyze this assembly. The interaction between catalyst and nanotube will impact the pattern of lattice fringes in high resolution TEM images, and therefore detect the catalyst and nanotubes crystallographic relationship.

Carbon nanotubes have advantages for electron microscopy work, because their near cylindrical symmetry and propensity of lie perpendicular to the electron beam makes data acquisition and interpretation much simpler than for single crystal supports. With the help of lattice fringe visibility theory, we can find the crystallographic relationship between catalyst particle and carbon nanotube, as shown in Figure 1 (Qin et al. 2003; Fraundorf et al. 2005). If the relationship is epitaxial, one might conversely decorate tubes in order to determine the chirality of their outer sheet. We illustrate the approach with specific case: Growth of FCC metals on the top of (0002) graphite (or graphene) surface of a carbon nanotube. The theory is easily extended to growth of other lattice types. Application to experimental images of Pt fuel cell catalyst crystals, on carbon nanotube supports, illustrates the strategy.

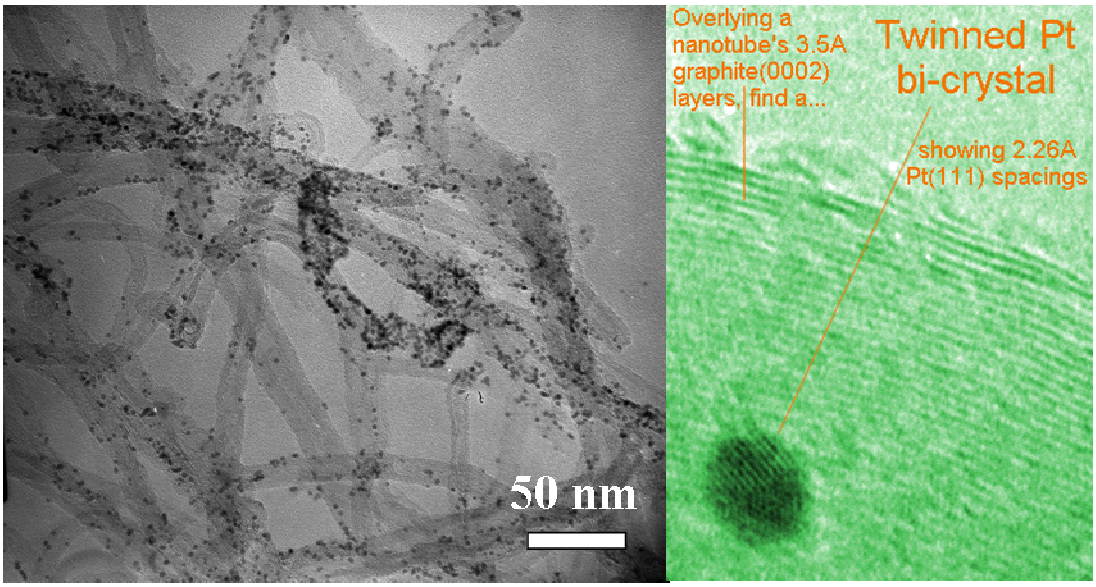

Figure 1.1. Low magnification (left) and high magnification (right) TEM image of Pt particles supported by carbon nanotubes (2006, S. Lin, P. Fraundorf).

The lattice fringe relationship between Pt particles and carbon nanotubes can be easily identified by counting the distribution of FCC lattice fringe angles in images of a nanotube support and the relative location compare the axis of the tube. Digital darkfield techniques also provide a way to automate this analysis.

1.2. THEORY

1.2.1. Fringe visibility theory As aberration-correction makes it possible for electron microscope images to provide resolutions into sub-Angstrom range, quantitative information contained in lattice image will become increasingly robust. In particular, on tilting away from the edge-on view of a lattice-plane in the transmission electron microscope (TEM), one might encounter a range of electron angles within which the lattice plane's reciprocal lattice spots continue to intersect with Ewald sphere. Hence the

lattice fringes associated with those planes remain visible. The upper bound of this "visibility band half-angle" (with the largest term first in the "thin specimen" limit) is

$$\alpha = \sin^{-1}[d\frac{\Gamma}{t} + \frac{\lambda}{2d}(1-(d\frac{\Gamma}{t})^2)]. \quad (1)$$

Here d is the spacing of lattice planes, t is the crystal thickness, λ is the wavelength of the electron, and Γ is a " visibility factor" on the order of 1 that empirically accounts for the signal-to-noise in the method used to detect fringes. The effective radius of the reciprocal lattice spot in this model (or excitation error s at which the fringe fades to background) is $\frac{\Gamma}{t}$.

We apply the theory to three types of relationship between supported FCC nanocrystals and underlying carbon and/or BN nanotubes: randomly oriented, (111) columnar, and (111) epitaxy. The objective is to illustrate the distribution of (111) lattice fringe orientations expected on a nanotube encountered by the electron beam "side on". The result is expected to be insensitive to slight deviations of the beam from perpendicularity to the tube axis.

1.2.2. Predictions from visibility theory For the random orientation case, each nanoparticle orients randomly to the electron beam. This might occur, for example, if the nanoparticles grow or accumulate with no regard to the underlying surface. Each nanoparticle has four sets of (111) lattice planes, in tetrahedral orientation to each other. From the equation 1, the fringe will show up in the center of a 28 nm diameter particle only when the electron beam is tilted by less than a α value of about 5 degrees out of that plane. For sufficiently thin particles, this result is relatively insensitive to the high energy of the electrons that the microscope is using. For random growth, most of the particles

have no visible (111) lattice fringes, but the (111) lattice fringe has equal visible opportunities at all different positions from the center of the tube to the edge part of the tube if beam is tilted at certain angle. Also the azimuthal angle between (111) fringes and tube edge ranges from -90 degree to 90 degree.

Figure 1.2 shows projected atom positions of columnar growth model particles on the carbon nanotube. Since the particles are on the tube surface, the relative location of the particle is described by the fraction radial distance $\frac{r}{R}$ from center of the tube (0) to the edge of the tube (1). The angle ϕ_{view} between a given particle fringe and the tube ranges from -90º to 90º, and is set to zero when the fringe is parallel to the tube axis.

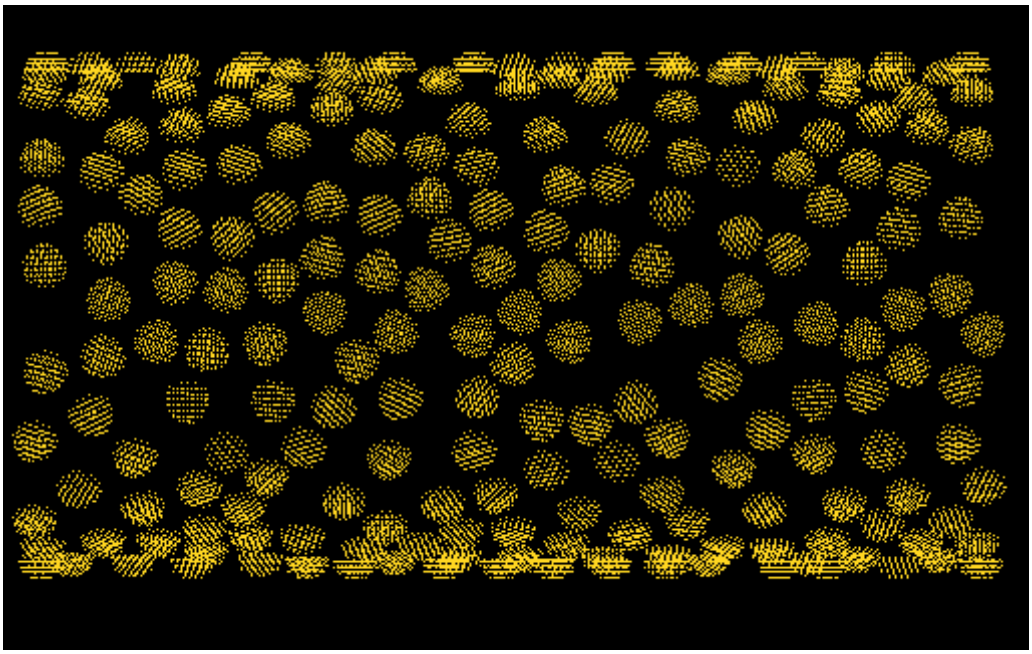

Figure 1.2. Illustrated Pt lattice fringe patterns expected on carbon nanotube (2006, P. Fraundorf).

The data we want to analyze is the projected angle of observed lattice fringes and their positions with respect to the projected tube axis. This data is plotted on a graph as

shown in Figure 1.3a. The random growth case in this plot expected to show fringes at all points across the field of this plot. Near the edge part $(r = 1)$ the number of fringes will be large because more particles will be seen there in projection. In the columnar growth case, predicting where fringes will be seen depends on several other parameters. These include the local azimuth of a lattice fringes' tilt axis with respect to a nanotube on which it resides ϕ_{local}, the angle between that lattice plane's normal and a reference or growth plane ζ, the angle between the growth plane and the viewing direction θ, and the angle between the beam direction and the fringe plane normal θ_{beam}. When θ_{beam} is equal to 90º, the fringes will be visible.

The relative distance from the center of tube axis determines angle between the growth plane and the viewing direction θ. The azimuth of projected fringe and tube axis ϕ_{view}, combined with θ, determines the lattice plane's local azimuth angle ϕ_{local} and angle between fringe plane and the beam θ_{beam}. The result of this analysis is that fringe visibility plots on these graphs as a one parameter family of curves which depends only on ζ, the angle between the fringe plane and the growth plane. Figure 1.3a illustrates for our specific example of FCC columnar growth on (111) planes.

FCC crystals have four (111) planes which pairwise intersect down each of six $\langle 110 \rangle$ beam directions at an angle of $\theta_g = \cos^{-1}(\frac{1}{3}) \cong 70.5$ degree. At the edge of the tube, the (111) growth plane is either parallel to the tube wall (0º degree) or has $\pm 70.5^{\circ}$ degree with tube wall as shown in Figure 1.4. FCC crystals have three (200) planes which pairwise intersect down each of six $\langle 110 \rangle$ beam directions at an angle of $\pm 54.7^{\circ}$ degree

angle with tube wall as shown in Figure 1.4. FCC crystals have six (220) planes which pairwise intersect down each of six ⟨110⟩ beam directions, half at an angle of $\pm 30^{\circ}$ and half at 90º with tube wall as shown in Figure 1.4.

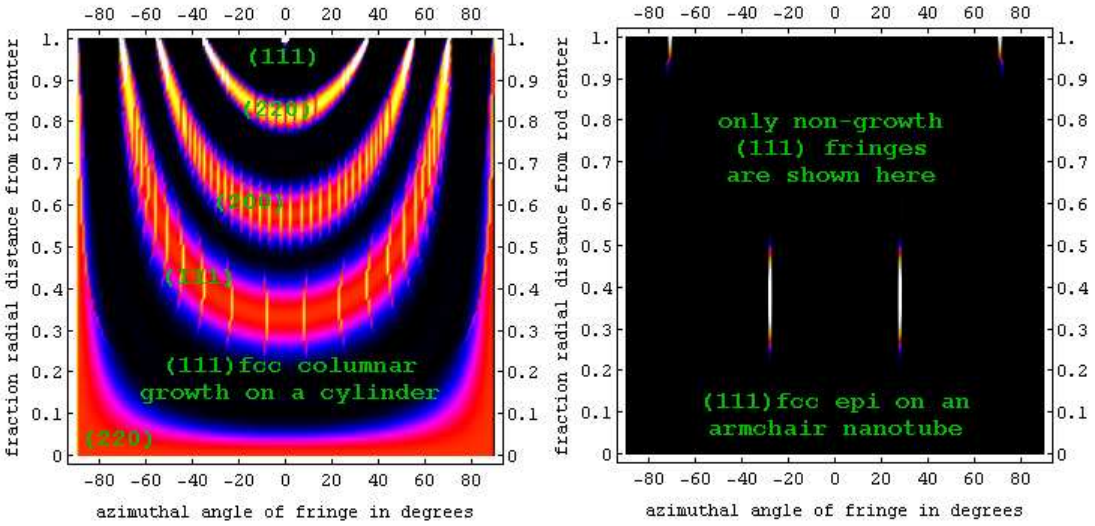

Figure 1.3. The diagram showed the relationship between azimuthal angle of (111), (200) and (220) FCC Pt crystals and the fraction radial distance from the center of the tube in the columnar growth model (left). Right was relationship between azimuthal angle of (111) FCC fringe and fraction radial distance from the center of the tube in epitaxally growth model on armchair nanotube (2006, P. Fraundorf).

For epitaxial growth, according to the diffraction data in the literature, FCC Pd on single crystal graphite (0002) planes typically takes place with $(111)_{\mathrm{Pd}}$ parallel to $(0002)_{\mathrm{graphite}}$ in the growth direction, and $\langle 112 \rangle_{Pd}$ parallel to $\langle 010 \rangle_{graphite}$ in the plane of the substrate (Humbert et al. 1991). If Pt particles also epitaxially grow on the carbon nanotubes, there is only one azimuthal angle at various positions as illustrated for an armchair nanotube in Figure 1.3. These allowed angles differ with tube chirality, so that analysis of epitaxial particles would also determine outer graphene-layer orientation.

1.2.3. Computer experiment results

1.2.3.1. Manual count result The relationship between (111) lattice fringe with carbon nanotube can be measured directly according to the angle distribution and the distance fraction from the center of the tube. After counting the azimuthal angle and fraction radial distance from the center of tube like that in Figure 1.2, we can find this relationship as shown in Figure 1.4. From Figure 1.4, we find that at the different tube positions, only certain angles of the (111) lattice fringes show up. For example, at the edge of the tube part (the fractional radial distance is the radius of the tube) there are 0 degree and 70.5 degrees between Pt (111) lattice fringe and tube edge. Other particles will show no fringes. When the fractional radial is about 0.3, the angle there is 0 degree between (111) lattice fringe and tube edge.

The data is consistent with theoretical data we get from the model, as shown in Figure 1.3. The (200) and (220) lattice fringe maps can be obtained by the same method.

1.2.3.2. Digital darkfield imaging technique result Digital darkfield imaging techniques can provide an alternative to counting the angles manually. Optical darkfield imaging in microscopy involves forming images of a specimen using a back focal-plane (scattering angle) aperture that excludes the unscattered beam. It's called "dark field" because the field surrounding the specimen doesn't scatter, so it's dark. The digital darkfield animation below illustrates this by placing an aperture (centered in the orange figure below) over the power spectrum (a digital substitute for the back focal-plane's optical diffraction pattern) here shown with the DC peak (or unscattered beam) below center (Fraundorf 2008). In this example, only nanocystals with projected periodicities

that diffract into the aperture light up in the darkfield image at right, and this varies with aperture position. Figure 1.5 shows that using this technique, the (111) lattice fringes light up after moving the aperture at different angles.

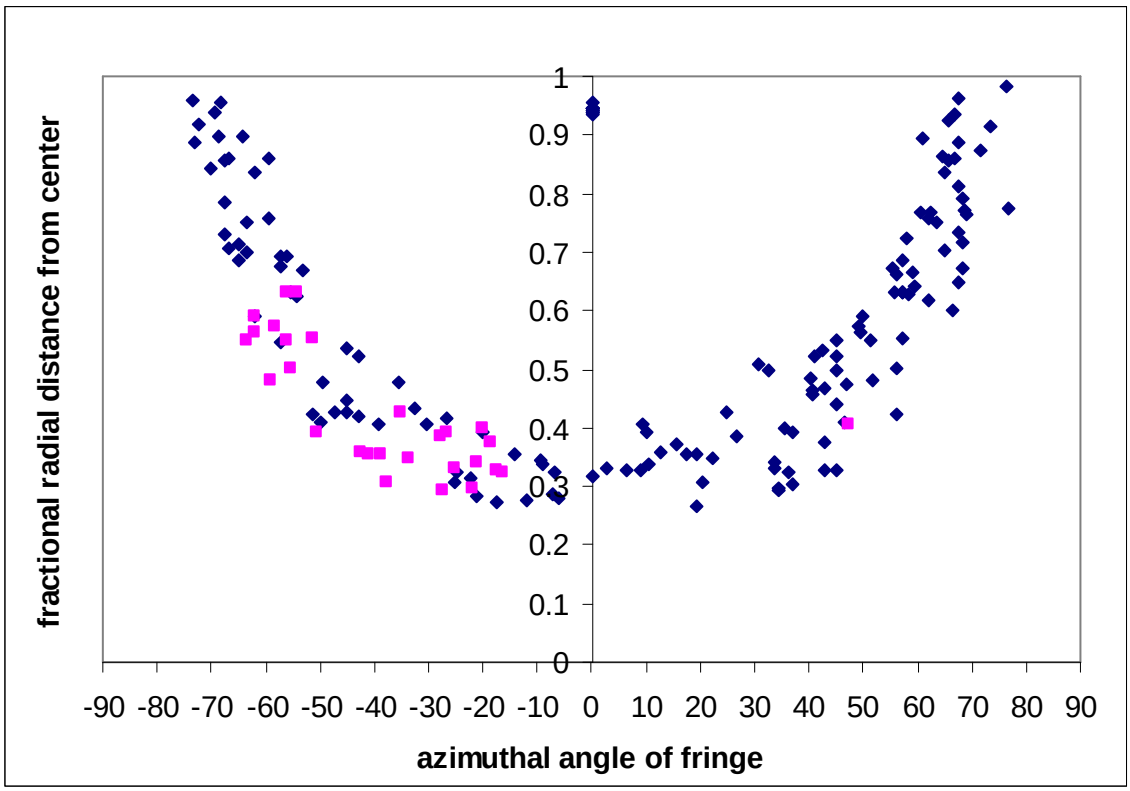

Figure 1.4. The azimuthal angle of (111) Pt lattice fringes versus projected distance from the tube axis for a columnar growth model specimen. The fractional radial distance was from center of the tube (0) to the edge of the tube wall (1).

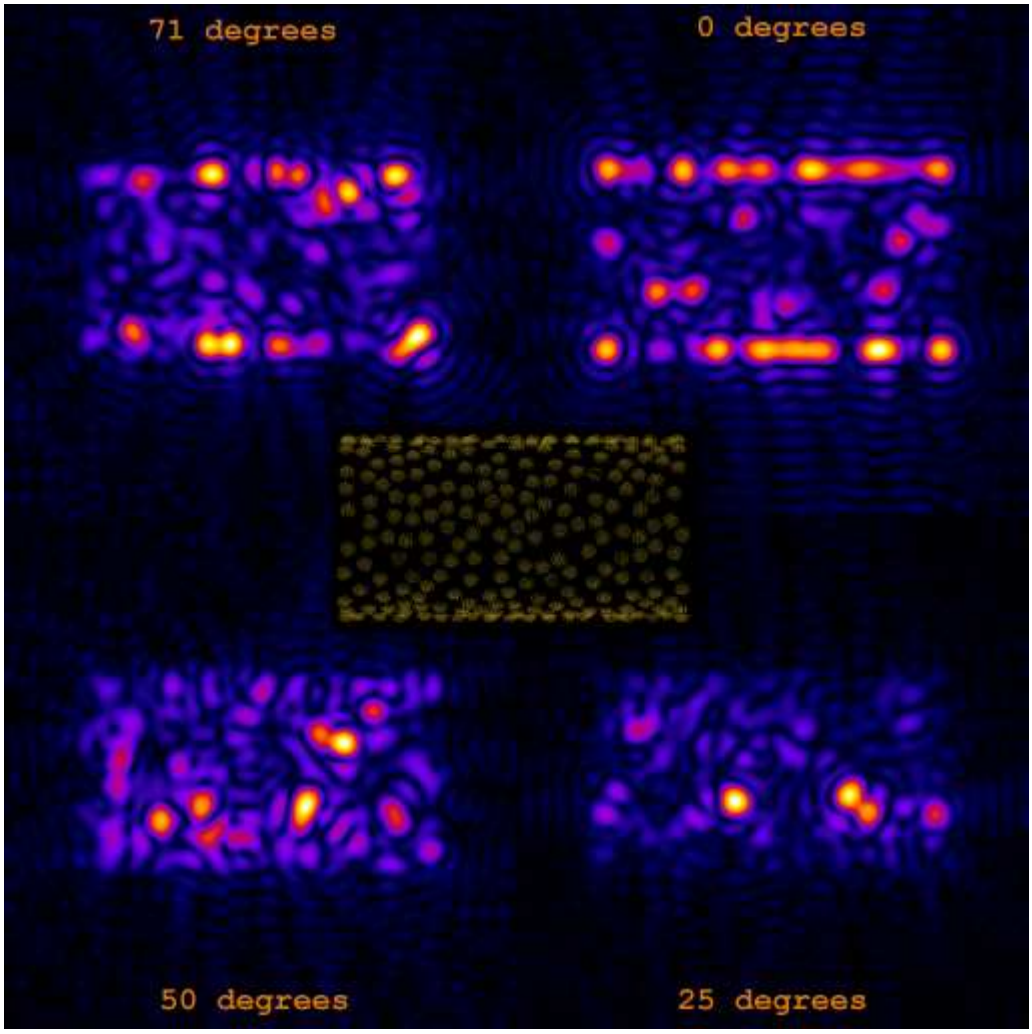

Figure 1.5. Using digital darkfield image technique, (111) lattice fringes were light up at the direction (2006, P. Fraundorf).

If we add all the intensities together after moving the digital darkfield aperture by 1.25 degree increments around the power spectrum ring from the Pt (111) lattice spacings, we get a relationship between azimuthal angle of (111) lattice fringes and fractional radial distance from the tube center (Figure 1.6). The digital darkfield imaging technique results illustrate the method and confirm the prediction as well.

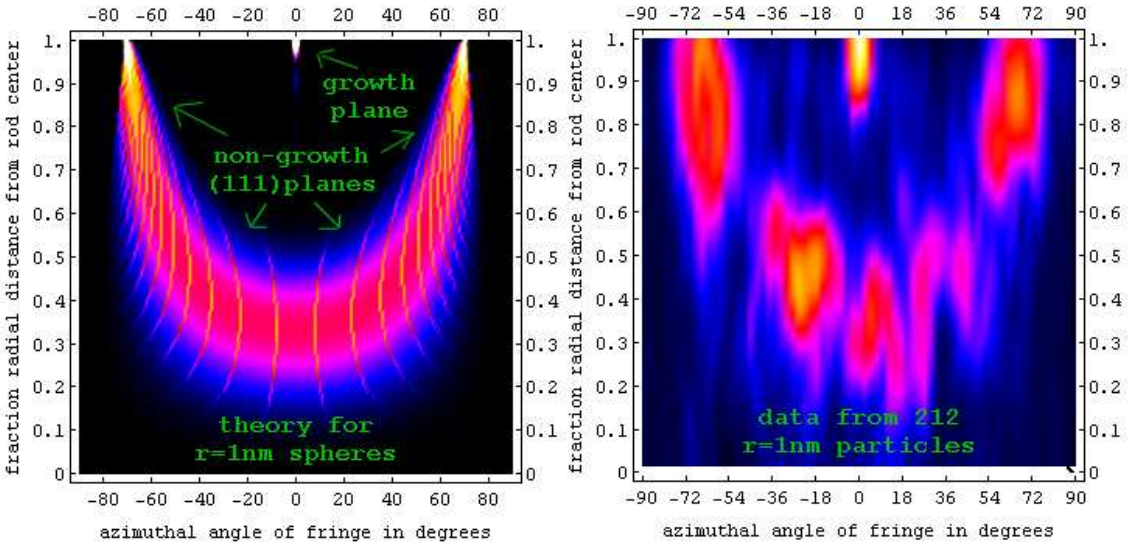

Figure 1.6. 2.3 Angstrom periodicity along various directions in a lattice image, combine with fringe visibility theory to analyze the crystallographic relationship between some nanoparticles and a cylindrical structure on which they lie (2006, P. Fraundorf).

1.3. EXPERIMENTAL TEST

In this experiment, we use a Philips EM430ST with point resolution near 0.2 nm to image Pt nanoparticles on nanotubes. In the high resolution image, the Pt nanoparticles lattice fringes and carbon tube fringes can be observed simultaneously. After counting the azimuthal angle between (111) lattice fringes with tube edge, we found that the Pt fringe angles are randomly distributed on the carbon nanotube as shown in Figure 1.7. So in this case, the nanoparticle growth is not along (111) columns.

1.4. DISCUSSION AND CONCLUSIONS

FCC particles and carbon nanotube lattice fringes can be observed under high resolution transmission electron work. Three different types of growth are discussed here. The relationship of azimuthal angle between (111) lattice planes and tube edge at various positions is different in random growth, columnar growth and epitaxial growth cases.

Digital darkfield imaging technique reveals the relationship efficiently. The preferential orientation on carbon nanotubes is more complicated by two factors.

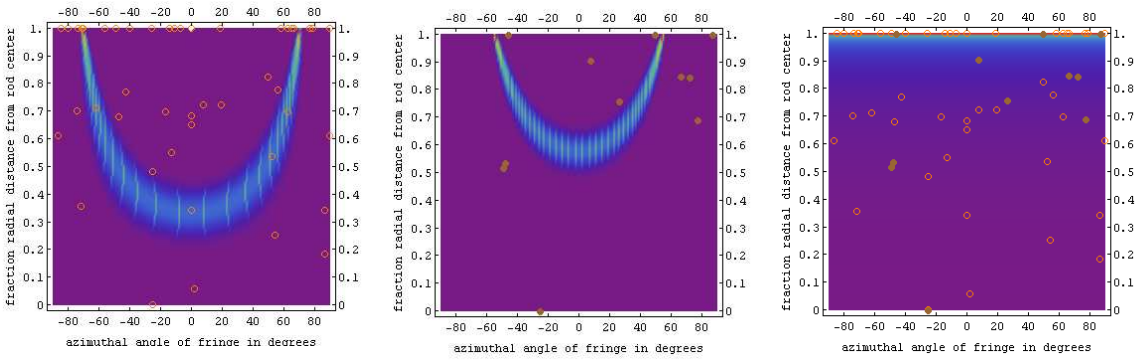

Figure 1.7. Experimental data was superimposed on the previous model data.

The first factor is surface integrity. For example in the experimental specimens above, it is easy to see that intact graphene layers only make it within a few atomic layers of the surface. This is likely due to an intentional roughening treatment designed to improve particle adhesion. Hence epitaxial growth would be impossible on these specimens, although columnar growth is still conceivable.

The second complication is surface curvature. We are not aware of experimental data on the effects of graphene sheet curvature on epitaxy. For example, it may be possible only on larger diameter tubes. On the other hand, the technique of detecting epitaxy suggests that nanotubes substrates serve as an excellent candidate for experimental investigation of these sheet curvature effects.

In summary, the study of the azimuthal angle with tube edge is very important to investigate the relationship of particles on tube or rod surfaces. This method can also be

easily used to explore other various catalyst particles on different substrates. It is very helpful to understand catalyst activities at specific surface orientations.

1.5. FUTURE WORK

These fringe visibility models for analyzing experimental data provide a deeper insight into the relationship between metal particles and supports. In some cases the symmetry of the metal catalyst and support will affect material properties a great deal. If we can design experiments to control catalyst particle orientation on nanosupports, catalyst efficiencies may increased a lot. We need evaluate the model from more experimental data.

CHARACTERIZATION ZINC OXIDE NANOSTRUCTURES

In order to investigate zinc oxide structures and their formation mechanism, further characterization is described in the upcoming sections, Papers 2, 3, and 4. Understanding the chemical and physical process involved is important to designing an efficient synthesis process for the desired structures. In the following sections (Papers 2, 3, and 4) abstracts are included because these sections represent different papers in preparation.

PAPER
2. GROWING ZnO NANOWIRES VIA DIFFUSION ON AU

(Coauthor: P. Fraundorf, L.F. Allard, J.Y. Howe, and J. Liu)

ABSTRACT: ZnO nanowires were synthesized by thermal evaporation. Lattice imaging shows that Au {111} planes are typically parallel to ZnO {0001} at an interface that lies perpendicular to the wire's growth direction. Au {224} planes lie parallel to ZnO $\{01\bar{1}0\}$ in the growth direction. Energy dispersive X-ray (EDX) nano-analysis shows that pure gold particles remain at the tip of ZnO nanowires after growth. Aberration-corrected high angle annular darkfield (HAADF) scanning transmission electron microscope (STEM) images show that a single layer of atoms at the interface is modulated by clear atom columns separated by a dark region with a misfit Burger's vector of one Au atom column separation ($3d_{224}$). Only this layer and adjacent Au layer shows evidence for mixing between Au and ZnO. These observations indicate that vapor liquid solid growth does not drive ZnO nanowire formation, but instead that the source vapor is transported along gold particle surfaces, including the buried Au (111) interface during growth of the wire. The observations suggest a coherence-zone mechanism for nanowire catalysis that depends on the large interface misfit, and that may have wide applications.

Zinc oxide nanowires have potential to be building blocks for future electronic and optoelectronic devices, such as photodetectors (Pettersson et al. 2006), field emissions transistors (Zhu et al. 2003), single electron memory devices (Thelander et al. 2005), UV light emitters (Tseng et al. 2003b), sensors (Wan et al. 2004; Zheng et al. 2005), piezoelectric nanogenerators (Qin et al. 2008), lasers (Duan et al. 2003), and solar cells (Law et al. 2005). Various methods have been applied to fabricate aligned zinc

oxide nanowires, including thermal evaporation (Huang et al. 2001b), metal organic chemical vapor deposition (MOCVD) (Park et al. 2004), pulsed laser deposition (Sun et al. 2006), and template-based growth (Wang et al. 2006a). Vertically-oriented zinc oxide nanowires can be obtained by selecting an appropriate crystalline substrate whose lattice constant matches spacing in the ZnO (0001) plane, like sapphire (Yang et al. 2002), GaN (Fan et al. 2006), AlGaN/AlN (Wang et al. 2005), and ZnO film (Jie et al. 2005). Aligned ZnO nanowire can also be fabricated on (100) silicon substrates (Geng et al. 2004).

Gold nanoparticles are generally used as a catalyst in growing one-dimensional nanowires of semiconductor or metal oxide materials (Morales et al. 1998; Huang et al. 2001b). The nanowires growth mechanism is attributed to the vapor-liquid-solid (VLS) process (Wagner et al. 1964; Dick et al. 2005). It has recently been reported that the vapor-solid-solid process may also be apply to the Au-catalyzed growth of ZnO nanowires (Kirkham et al. 2007). Fundamental understanding of Au-ZnO system is still a challenge, which limits the scale-up of desired structures fabrication. We report here, using aberration-corrected and nano-analytical electron microscopy technique, a detailed study of the Au-catalyzed growth process of ZnO nanowires as well as the interface between Au and ZnO.

ZnO nanowires were grown by a simple standard thermal evaporation-condensation process. Mixtures of commercial ZnO (99.99%, Alfa Aesar) and carbon black in selected ratios were placed in an alumina boat as source material, located in the center of a tube furnace. Freshly-cleaved mica substrates coated with a thin gold film were put in a lower temperature zone of the furnace downstream. We set the source material temperature at 1000° C with heating rate at about 30°C/minute, and then held

the temperature constant about one hour. The argon gas flow rate was set at 15 sccm in the experiment, after purging the tube.

Nanowires were deposited on the substrates in the temperature range of 800^{o} C-650^{o} C. The pressure was kept at one atmosphere during the experiment. The system is cooled down quickly at the end of the experiment.

The morphology of as-synthesized products was examined by field emission scanning electron microscope (JEOL 6320FX). High angle annular dark-field (HA-ADF) STEM images were acquired using a JEOL 2200FS instrument equipped with a CEOS Co. (Heidelburg, Ger.) aberration corrector on the probe-forming optics that provide a nominal probe diameter for STEM imaging of 0.07nm, at an illumination acceptance semi-angle of 26.5 mrad (O'Keefe et al. 2005). Nanoscale EDS analyses (Thermo-Noran) were performed on a Hitachi HF-3300 cold field-emission analytical TEM, operated at 300kV.

Field emission scanning electron microscopy (FESEM) provided data on the morphology of the ZnO nanowires and their relationship to the substrate. A typical FESEM image for nanowires, grown on a substrate coated with Au, is shown in Figure 2.1. The image shows that uniform ZnO nanowires were formed on the gold-coated substrate in high yield. This means that the technique can be scaled up for large area production. Gold particles trigger nanowire growth. Nanowire diameters normally range from 20-60nm, with lengths about 1-2 micrometers.

Gold particles 50-100nm in diameter are observed clearly at high magnification in backscattered FESEM images. In regions where the ZnO nanowires are very dense, the tips of the nanowires are found at widely varying distances from the substrates (Figure

2.1b). Gold particle diameters are bigger than ZnO nanowire diameters. Hence gold particles may not control ZnO nanowire sizes as earlier reported (Huang et al. 2001b). Backscattered electron images show that gold particles as bright spots due to their high atomic number (Figure 2.1c). By focusing on different heights in the nanowire specimen, gold particles can be found at the tip of all nanowires, as shown in Figure 2.1d.

If the substrate temperature is over 850°C, one finds film-like structures without nanowires. We find that in lower temperature regions the ZnO nanowires increase in length. Smaller diameter nanowires are found, with kinks nearer the tip than the base. This may be due to less source vapor available at the end of the experiment. This phenomenon is also seen in the scanning transmission electron microscope (STEM). Some literature reports that such kinking can be attributed to growth instabilities, and thermal fluctuations or surface/interface energies (Wu et al. 2003; Burki 2007; Dick et al. 2007).

The crystal structure and orientation of nanowires removed from the substrate was investigated in the scanning transmission electron microscope. Figure 2.2 shows some STEM images of an Au-ZnO nanowire. Figure 2.2a is a low magnification HA-ADF image, showing a faceted Au nanoparticle at the tip of a ZnO nanowire. The gold is much brighter than ZnO in high angle annual dark field images, because of its high atomic number. The diameter of ZnO nanowires is around 20-30 nm. The high resolution HA-ADF image in Figure 2.2d shows atomic structures of both the Au nanoparticle and the ZnO nanowire. STEM images show that both the gold particles and the ZnO nanowires are single crystal structures without extended defects, like dislocations and stacking faults.

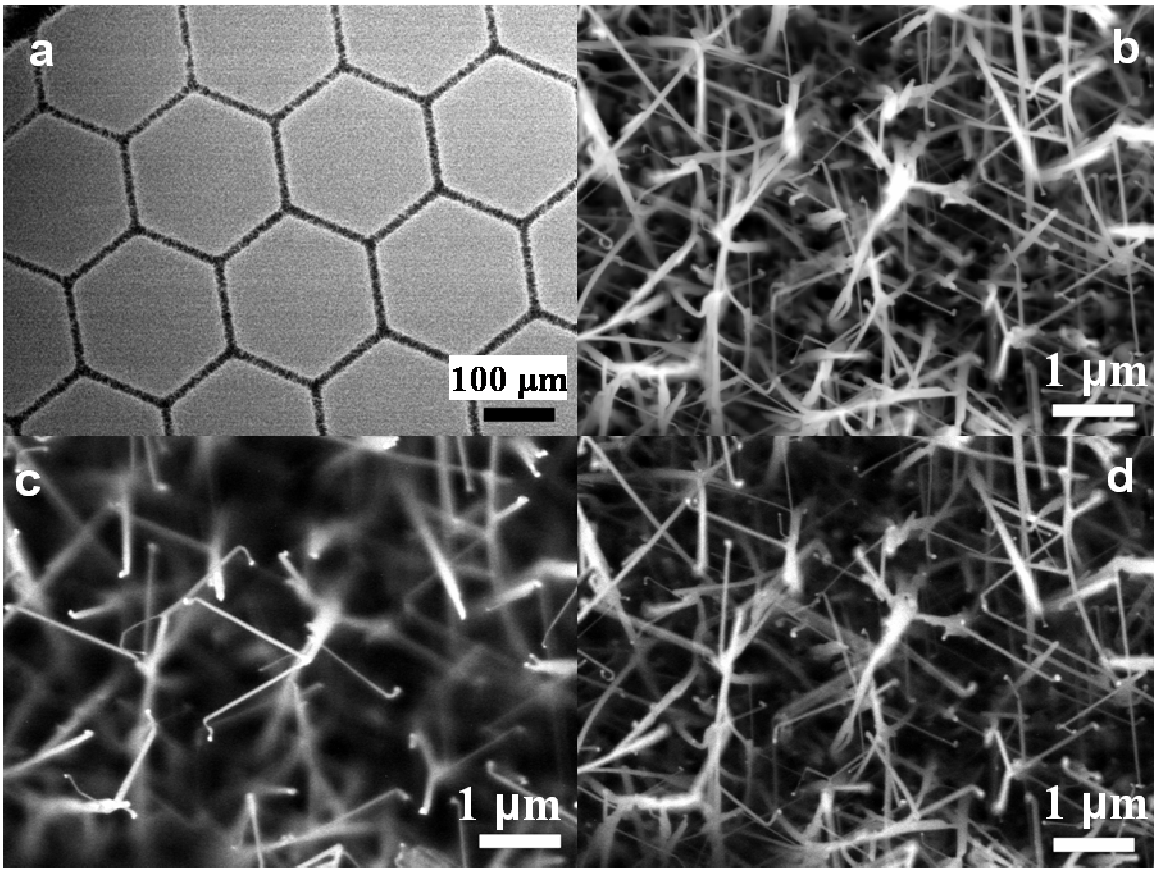

Figure 2.1. FESEM image of zinc oxide nanowires. (a) Low magnification SEM image of ZnO nanowire grown from the patterned Au. (b) High magnification SEM image of ZnO nanowire, showing that the nanowires have uniform diameters and clean smooth surface with gold catalysts on the tip of the nanowires. (c) High magnification backscattering SEM image of nanowire structures. Gold particles show up clearly due to the high atomic number. (d) Backscattering SEM image of the same area at different focus. Gold particles exist on inner layer individual nanowire (2007, J. Liu).

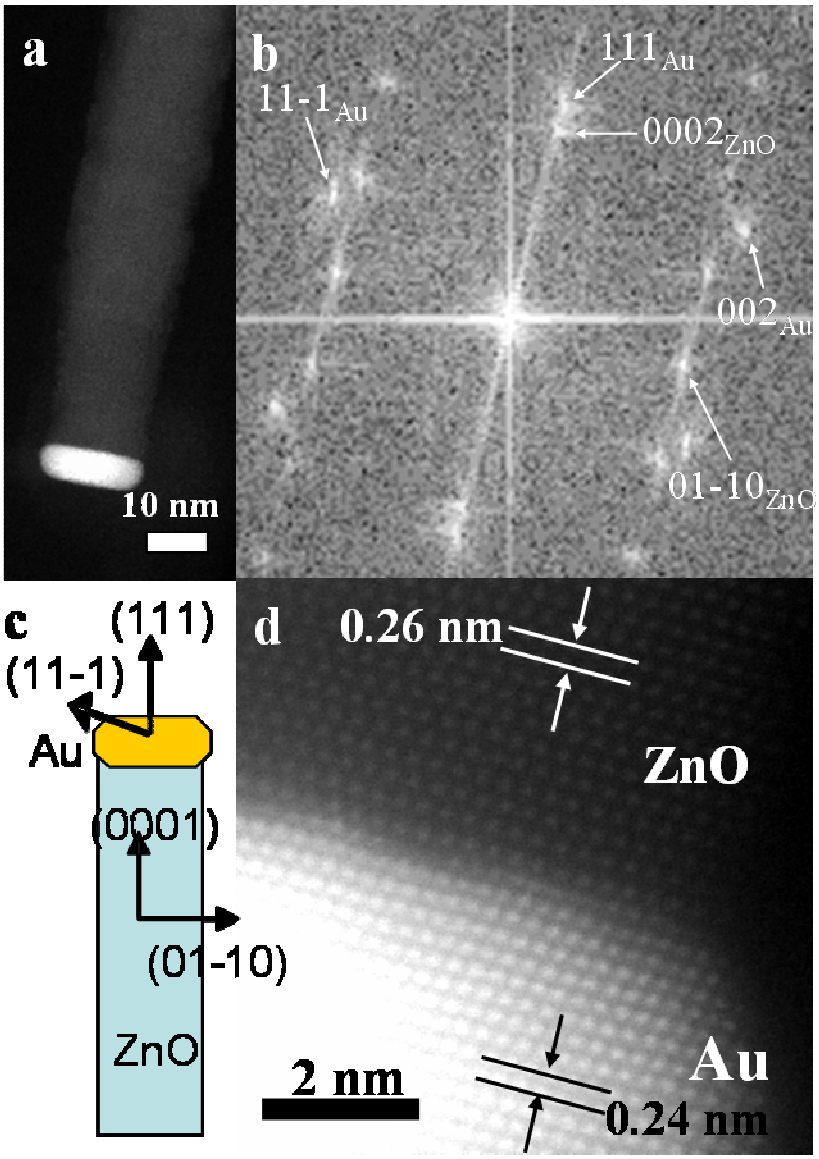

Figure 2.2. Low magnification HA-ADF image (a) shows a faceted Au nanoparticle located at the tip of a ZnO nanowire. Optical diffractogram (b) shows the structure relationship between Au catalyst particle and ZnO nanowires. Diagram schematics image (c) shows the relationship between Au and ZnO nanowire. High resolution HA-ADF image (d) shows the interfacial structure between the Au nanoparticle and the ZnO nanowire (2007, J. Liu).

Detailed analysis of several high resolution images shows that the ZnO nanowires have a wurtzite structure. The nanowire 0.26 nm lattice spacing corresponds to the d-spacing of an (0002) ZnO crystal plane: the ZnO nanowire's preferred growth direction. Side facets of the ZnO nanowire are $\{01\bar{1}0\}$, so that the electron beam is along ZnO $[2\bar{1}\bar{1}0]$. The particle on the tip shows the expected 0.24 nm cross-fringes at 70.5 degrees for Au (111) planes viewed down Au $\langle\bar{1}10\rangle$. Figure 2.2b shows the power spectrum of Figure 2.2d, confirming the epitaxial relationship between faceted Au nanocrystals and the ZnO nanowire: $(0001)_{ZnO} \parallel (111)_{Au}$, $(01\bar{1}0)_{ZnO} \parallel (22\bar{4})_{Au}$ and $[2\bar{1}\bar{1}0]_{ZnO} \parallel [\bar{1}10]_{Au}$. The diagram of Figure 2.2c illustrates this relationship between gold particle and ZnO nanowire. Several other gold/zinc oxide nanowires have been found to have the same orientation relationship. The relationship is consistent with earlier reports using X-ray diffraction and TEM (Fan et al. 2006; Wu et al. 2006; Kirkham et al. 2007).

Figure 2.3a is an intensity profile of periodic rows in the dark field image (Figure 2.2d). The periodicity of rows above and below the transition layer is uniform, while the periodicity in the atomic-thick transition later is modulated with the misfit periodicity expected between Au and ZnO lattices. Figure 2.3b shows the expected gold atom periodicity ($3*Au_{d224}$) in rows below that transition, the expected ZnO periodicity ($ZnO_{d01\text{-}10}$) above it. Figure 3b also shows evidence for both ZnO and Au periodicity only in the modulated layer, and in the Au layer immediately adjacent. This suggests that the catalytic action of the Au may be confined to these two atomic layers.

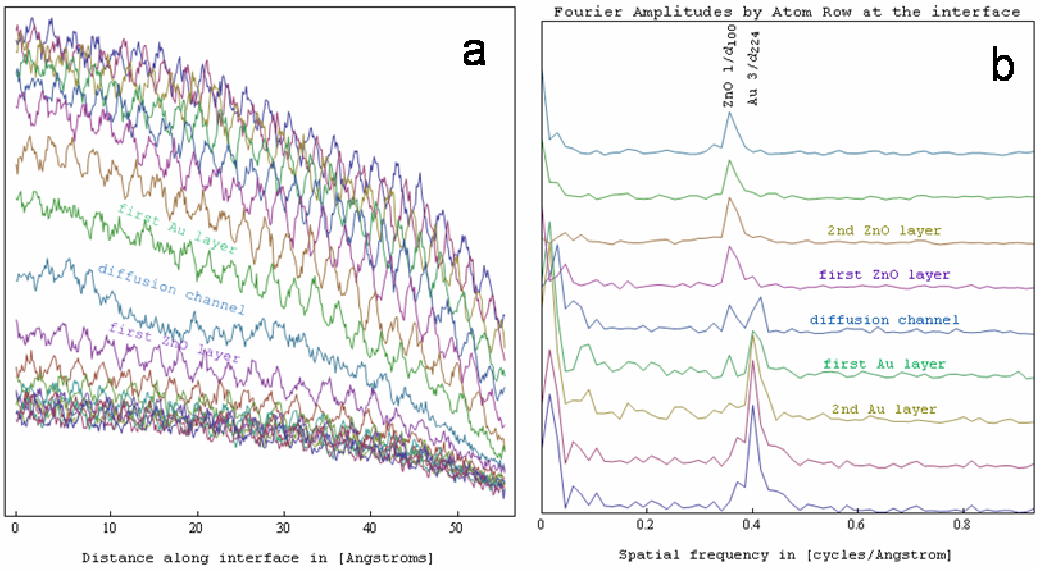

Figure 2.3. Figure (a) shows the profile of HAADF intensity along rows of atoms parallel to the interface. The gradual decrease of intensity in moving from Au to ZnO likely comes from C contamination on the specimen. Fourier transform amplitude spectra from rows on either side of that anomalous layer are shown in Figure (b). Note that there is evidence for a mixing of Au and ZnO periodicities only in the modulated layer, and in the Au layer immediately below that (2007, P. Fraundorf).

Although gold particles at nanowire tips are most common, HAADF images reveal that gold particles also occur at other places (Figure 2.4). Some nanowires are kinked near the tip, as mentioned earlier in SEM. High resolution STEM images (Figure 2.4b) reveals this crystallographic relationship between Au catalyst and ZnO nanowire: $(10\bar{1}\,\bar{1})_{ZnO} \parallel (1\bar{1}\,\bar{1})_{Au}$, $(10\bar{1}3)_{ZnO} \parallel (311)_{Au}$, $(0004)_{ZnO} \parallel (222)_{Au}$ and $[\bar{1}2\bar{1}0]_{ZnO} \parallel [01\bar{1}]_{Au}$. We also found one gold particle embedded in a ZnO nanowire (Figure 2.4c and 2.4d). High resolution images (Figure 2.4e) suggests that there is ~6º between the Au (111) lattice fringe and ZnO (0002) lattice fringe in this projection.

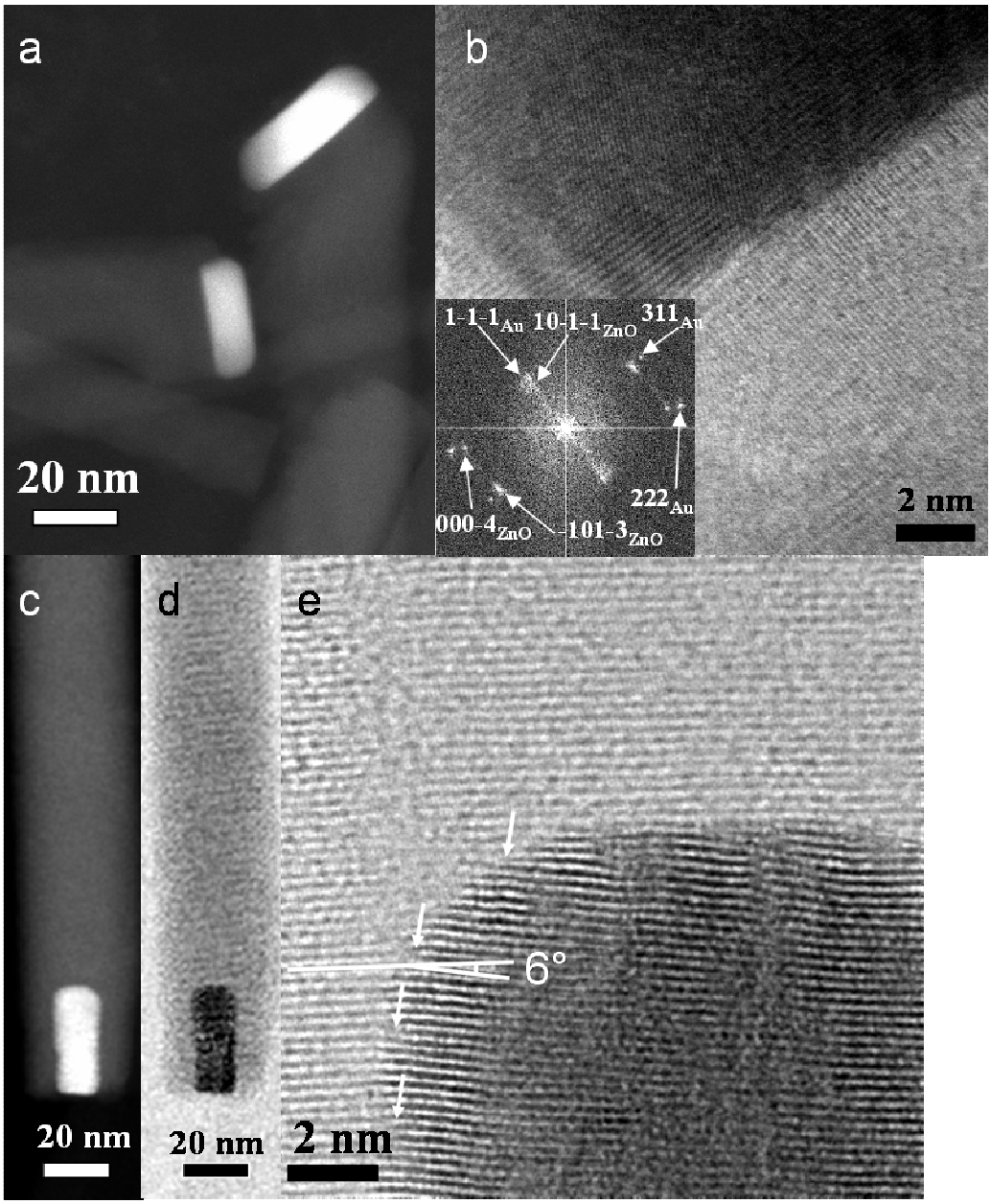

Figure 2.4. HA-ADF image (a) shows the Au nanoparticles are locating off the direction of the nanowire's growth direction. High resolution STEM image (b) shows that the epitaxial relationship between Au and ZnO nanowire. HA-ADF image (c) and bright field image (d) shows that gold particle is embedded in the nanowire. High resolution STEM image (e) shows that there is 6 degree angle between Au (111) lattice fringe and ZnO (0002) lattice fringe (2007, J. Liu).

The modulated contrast layer in Figure 2.2d also shows that the large misfit between Au and ZnO lattices is accommodated by an edge-dislocation Burger's vector in the plane of the interface, rather than by lattice strain, since around each channel one finds 10 Au columns for every 9 Zn columns. This is illustrated also in Figure 2.5, which shows periodic arrays of dislocations (arrowed) about every 5nm along an Au/ZnO interface. The fact that the spacing between coherence zones in images down Au $<110>$ averages around 3nm (a bit larger than the 2.216nm expected from bulk lattice parameters) suggests that ZnO/Au compression (due to either doping or strain) in the plane of the interface is on the order of 3%. You can also see from Fig. 2.2d that the image incoherence associated with this dislocation is confined to the modulated plane of the atoms, instead of being shared with atom layers above and below.

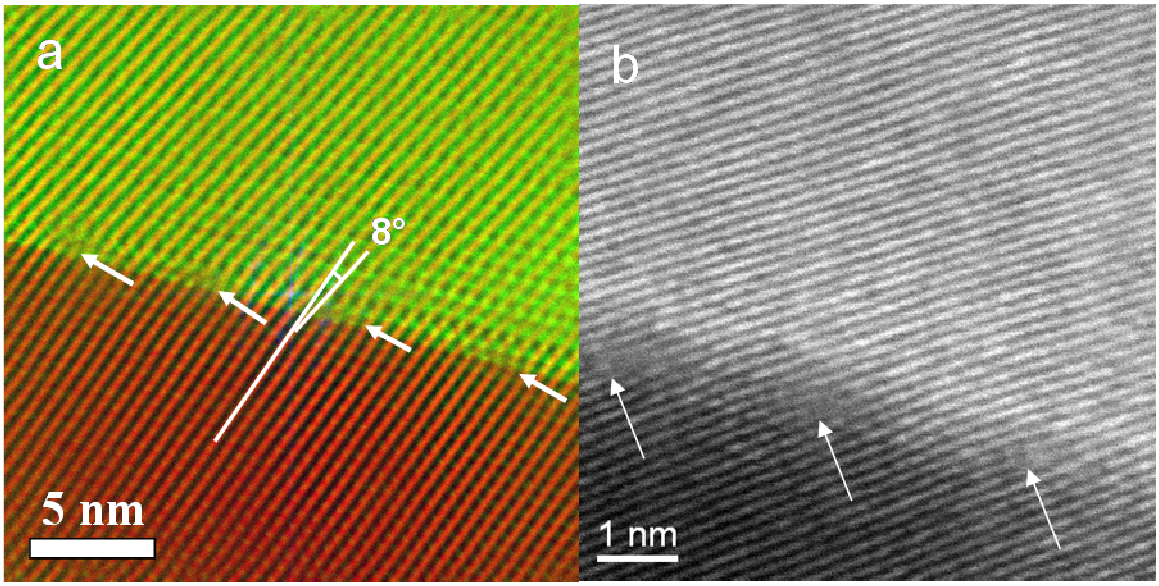

Figure 2.5. At lower magnifications and off-zone orientations, a periodic array of dislocations is apparent, as illustrated here with images of two different regions.

From the geometry of the ZnO {0001} direction in the bulk, oxygen atom rows might lie either just above or just below the Zn atom rows in Figure 2.2d. In addition, a single atom (Zn or O) or a pair of atoms (Zn/O or O/Zn) in projection might lie at the interface with Au if there is no reconstruction. Ground state energy calculations have been reported in the literature to investigate these 4 alternatives, and three types of symmetric lateral alignment that might be preferred by these terminations on Au (111) (Murakami et al. 2003; Meyer et al. 2004; Zaoui 2004; Lin et al. 2007; Wei et al. 2007b).

These lateral zones are illustrated in Figure 2.6, which is a growth-direction view of interfacial atoms azimuthally rotated so that $Au\{224\} \parallel ZnO\{01\bar{1}0\}$ as observed. The bulk lattice parameter mismatch is undisturbed in this figure, with a region of fcc-hollow alignment placed in the center. The figure depicts only the interface between a single layer of Au on a single layer of ZnO. The beam direction in the HRSTEM image of Figure 2.2d runs from lower left to upper right in Figure 2.6, showing that there are about ten gold columns (each separated by 3 times the d-spacing for Au (d224) of around 0.25nm) between “coherent zones” projected in the beam direction. The spacing between Zn atom columns on the other side of the interface is the d-spacing for ZnO $\{01\bar{1}0\}$ of around 0.28nm. As mentioned earlier this beat periodicity is supported by the interface modulation in Figure 2.2d, but detailed models of the observed interface in these specimens (e.g. coherence zone alignment, atom density fluctuations in the diffusion layer, etc.) are the subject of a separate paper.

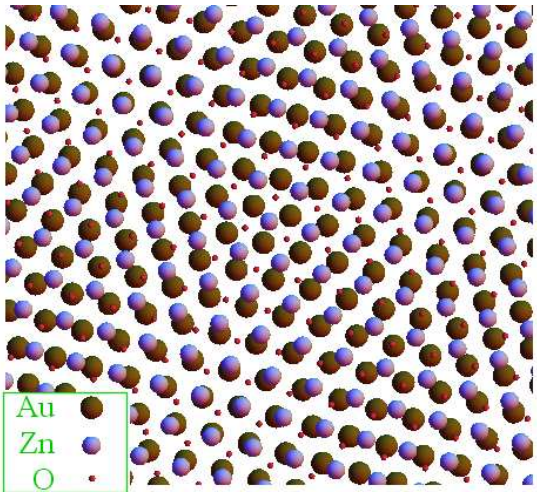

Figure 2.6. Schematic of atoms at a ZnO {0001} on Au {111} interface viewed face-on, with relative azimuthal rotation that agrees with data reported. Note that there are three types of alignment which have 3-fold symmetry: Zn over Au (upper left), O over Au (center left), and neither over Au (center). HAADF contrast in the modulated interface layer suggests that one of the alignments may be preferred for catalytic incorporation of ZnO into the growing nanowire. The field with is 4nm (2007, P. Fraundorf).

In summary, structural observations of the Au/ZnO interface suggest an array of dislocation pipes, possibly ordered around a hexagonally-distributed array of coherence zones creating broad disorder bands in projection that are confined to a single atomic layer at the interface. The lack of Z-contrast intensity in that layer between coherence zones may reflect a reduction in material density as well, since the modulation persists with minor changes in specimen orientation. In any case the disorder in that layer may facilitate the ZnO transport during wire growth beneath the gold, and also help explain why gold particles are often seen in FESEM images to have fallen off the nanowire tip.

To further explore the possibility of a surface diffusion mechanism for ZnO transport to catalyst sites across the interface, compositions of the Au nanoparticles and the ZnO nanowires were analyzed by nanoscale energy dispersive X-ray spectroscopy (EDS). In Figure 2.7 find spectra obtained from different areas of Au particle and ZnO

nanowires. Spectra from edge and center of Au nanoparticle confirmed that there was no Zn signal. Previous literature suggested that an Au and ZnO alloy may be formed at the end of the experiment. That is not the case here. No detected Au or other impurities were found in the ZnO portions of the nanowire either. The Ti peak originates from the Ti TEM grid. EDS data from several different nanowires confirmed that this was not an isolated incident.

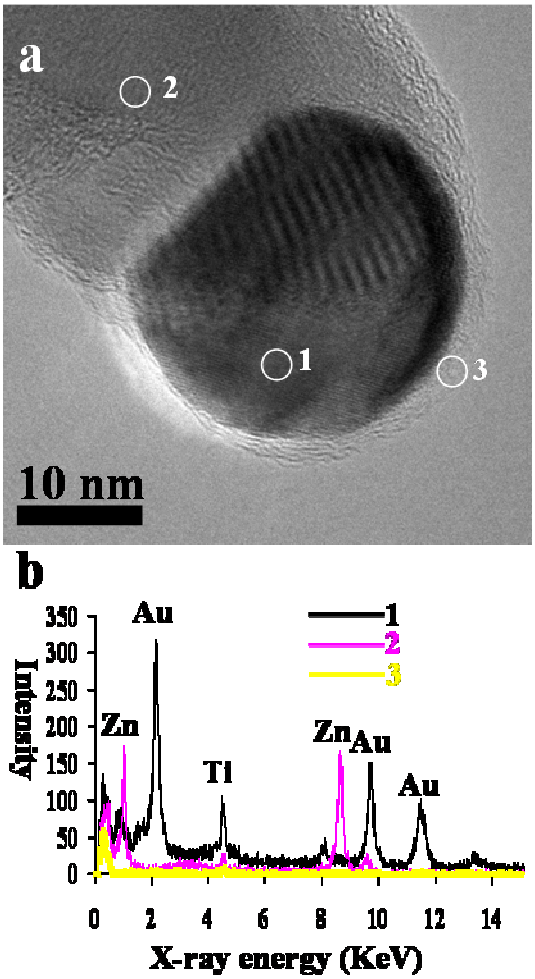

Figure 2.7. Low magnification TEM image (a) shows a nanoparticle located at the tip of a ZnO nanowire (2007, J. Liu). EDS spectra (b) show the element information on different location. Location 1 is mainly at gold particle position. Location 2 is located at ZnO nanowire. (Ti peak comes from the Ti TEM grid). 2 has Zn peak without apparent Au peak. Electron beam builds carbon contamination around sample surface as shown in location 3.

The consistency of the observed Au lattice parameter with the Wyckoff value (Wyckoff 1982), the near-bulk Au/ZnO parameter ratio inferred from the misfit periodicity, and the EDS spectra discussed above all indicate that major amounts of Zn are not present in the gold catalyst particle. Thus the gold particles did not deliver ZnO to the growth interface, and may have been solid during the nanowire growth. Although the substrates are located in the below 850°C region, where the temperature is far below the Au melting point, the melting point of an Au-Zn binary system is very complicated. For example, the alloy melting point is below 800°C if the Zn concentration is around 25% in the alloy (Massalski 1986; Liu et al. 2003b). Solid Au may also help catalyze the growth of semiconductor nanowires (Persson et al. 2004; Dick et al. 2005). Hence, the temperature alone can not determine if the gold was solid during the growth process. Our observations of pure gold rule out the Au-Zn melt alloy process for our nanowires.

The growth of one dimensional semiconductor nanowires has been explained by the BCF mechanism (Chapter 1) and by the vapor liquid solid mechanism (Burton et al. 1951; Wagner et al. 1964). The BCF mechanism uses a screw dislocation to aid nanowire growth. The screw dislocation provides a growth step for the next layer. This theory was developed by Sears for illustrating the growth of mercury (Hg) whisker (Sears 1955). In our system, there is no screw dislocation along the ZnO growth axis. Hence the BCF mechanism is not operating here. Another theory is the vapor liquid solid growth model proposed by Wagner and Ellis for silicon whiskers growth (Wagner et al. 1964). In this model, Au-Si droplets form when the temperature is around 950°C. The liquid droplet works as a seed to absorb arriving silicon atoms. The incoming silicon condenses at the interface between Au-Si alloy and silicon whisker. Consequently, silicon whiskers

formed. Much previous literature has used this theory to explain ZnO nanowire formation. Since there is no significant ZnO in the gold tip, it is hard to explain our specimens in term of the vapor liquid solid growth mechanism. The gold may instead be solid during nanowire formation, in which case a vapor-solid-solid mechanism may be needed to describe the process.

In our system, source material vapor is generated when the furnace is heated to 1000°C. Zinc oxide has reactions with carbon black and forms source vapor Zn and carbon oxide or carbon monoxide gas. The source vapor diffuses to the cooler temperature zone of the furnace due to the density gradient, since the lower temperature zone has relative less source vapor than the center of the furnace. Compared with a clean substrate, gold particles provide a low energy interface to collect ZnO vapor and form nanowires epitaxially (Dick et al. 2005). In terms of the source vapor deposited on the gold particles, there are at least two possible categories of wire growth.

In the first, source vapor diffuses through the gold particle to form single crystal nanowires. The source vapor diffuses along a concentration gradient created by nanowire growth at the ZnO interface.

The other process is shown in Figure 2.8. The source vapor deposits on the surface of the gold particle. Instead of diffusing into the gold particle, ZnO molecules travel on the surface of the gold particle to the Au/ZnO interface. There they are pulled into diffusion pipes lying in the atomic-thick modulated interface-layer shown above, by a concentration gradient created by nanowire growth at a hexagonal array of coherent zones described above. The source adatoms do not penetrate into the gold particle, so the gold particle has no reaction with ZnO during the nucleation process. Moreover, the large

lattice misfit between ZnO and Au atom rows at the interface, rather than serving as a disincentive to growth, is a key to both the dense network of observed diffusion pipes, and a high density of small catalyst-optimized coherence zones i.e. places where the ZnO lattice and Au lattice on opposite sides of the diffusion layer are aligned so as to favor creation of new layers. A closer lattice match would mean fewer and larger coherence zones, with a less dense array of diffusion pipes to facilitate transport to growth sites across the buried interface.

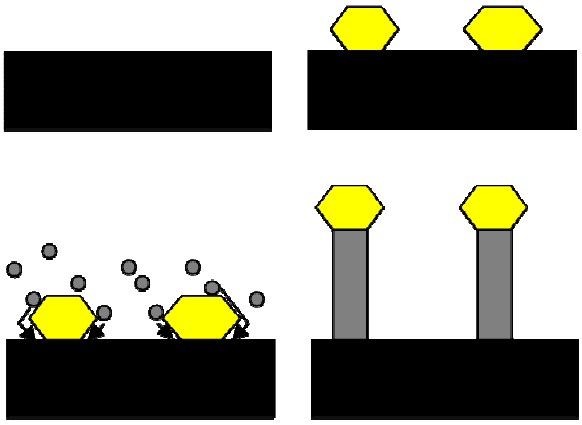

Figure 2.8. The proposed formation mechanism: ZnO vapor diffuses over the gold particle and forms the nanowire.

In summary, the thermal vapor deposition method produces high-density uniform ZnO nanowires. ZnO nanowires mostly exhibit an {0001} growth direction. The gold particles in our experiment are single crystal Au without significant ZnO. Using high resolution scanning transmission electron microscope and nanoscale EDS, an epitaxial relation between Au and ZnO nanowires is reported. Au (111) plane is parallel to ZnO (0002) . HAADF imaging revealed a single modulated atom layer at the interface

between Au and ZnO, with defined atom-column regions separated by dark regions insensitive to beam orientation in Z-contrast which show an edge-dislocation Burgers' vector of one gold column spacing ($3\times d_{224}$). The rows of Zn and Au atom columns above and below this layer look healthy, although minor ZnO periodicity was detected in the first Au layer only. These results suggest that ZnO is delivered to the growth interface not by diffusion through the Au particle, but by surface diffusion along Au surfaces including the buried Au (111) interface. They further suggest the possible existence of a hexagonal network of coherence zones at the interface, whose Au and ZnO alignments above and below are optimized for catalysis of new layers while the regions between those coherence zones provide channels for transport of ZnO to the growth interface. The bearing of this data on such a coherence-zone model, and its implications for nanoscale synthesis in other systems, will be discussed more fully elsewhere.

PAPER
3. EFFECTS OF CATALYST THICKNESS ON THE GROWTH OF ZINC OXIDE NANOSTRUCTURES

(Coauthor: S. Liu and J. Liu)

ABSTRACT. Various ZnO nanostructures have been synthesized using a tin-catalyzed vapor transport deposition process. Catalyst thickness has a direct impact on the final product morphology. In this paper, we show that under the same experimental conditions, very different nanostructures deposit on a clean mica substrate, a tin particle coated substrate, and a tin film coated substrate. Particles-shaped structures form on the clean mica substrate, aligned nanowires are found on tin particle coated substrate, and belt shape structures are found on tin film coated substrate in the same temperature zone. At the same substrate, nanostructure sizes decrease from high temperature to low temperature. The substrates with more catalyst may have stronger absorbing capability, and thus bigger and longer nanostructures are shown in our experimental results.

Controlled synthesis of zinc oxide nanostructures has gained a lot of attention due to its wide range applications as: fundamental building blocks for future electronic components (Kuoni et al. 2003), ultrasensitive gas sensors (Comini et al. 2002; Arnold et al. 2003), field emission displays (Banerjee et al. 2004), UV detectors (Konenkamp et al. 2004), nanostructured catalysts (Yumoto et al. 1999), solar cells (Keis et al. 1999) etc. Many chemical and physical methods can be used to synthesize ZnO nanostructures. Direct vapor transport method in a tube furnace is simple and easily accessible. Vapor-liquid-solid and vapor-solid processes have been proposed as the main growth mechanism of zinc oxide nanostructures in this system (Huang et al. 2001b; Pan et al.

2001). The fundamental understanding of nucleation and growth processes is still not well understood. Therefore controlled synthesis of desired nanostructures is a big challenge. In the synthesis system, several parameters may have a big influence on the final structure including total and partial pressure in the tube, substrate temperature, gas flow rate, and substrate material. Some parameters may couple with each other. For an example, gas flow rate may also have an impact on the substrate temperature. In order to understand the system more clearly, we need understand each parameter's function in the experiment.

Various metals, such as gold (Huang et al. 2001a), tin (Gao et al. 2003a), etc. have been used as the catalyst to get zinc oxide nanostructures. At the same experiment, the influence of different catalyst thickness is not well understood. In this letter, we report a simple method to investigate the impact of a different thickness of catalysts on the zinc oxide nanostructures.

The experimental apparatus includes a horizontal tube furnace, and gas supply system. The mixture of commercial ZnO and carbon black in a certain ratio was placed in an alumina boat as source material and located in the center of the tube furnace. Clean mica, tin particle coated mica, and thick tin film coated mica were used as substrates put in the lower temperature zone of the furnace. These three kinds of substrates actually come from the same piece of mica with different coating times. We set the furnace at 1000°C with the heating rate at about 30°C/minute and kept the temperature about one hour. Argon gas was used as the carrier gas with flow rate at 15 sccm in one set of experiments. The nanostructures were deposited on the substrates in the temperature range of 650^{o} C-850^{o} C. The pressure was kept at one atmosphere during the experiment.

Morphologies of as-synthesized sample were characterized by high resolution field emission scanning electron microscope (FESEM JEOL 6320FX).

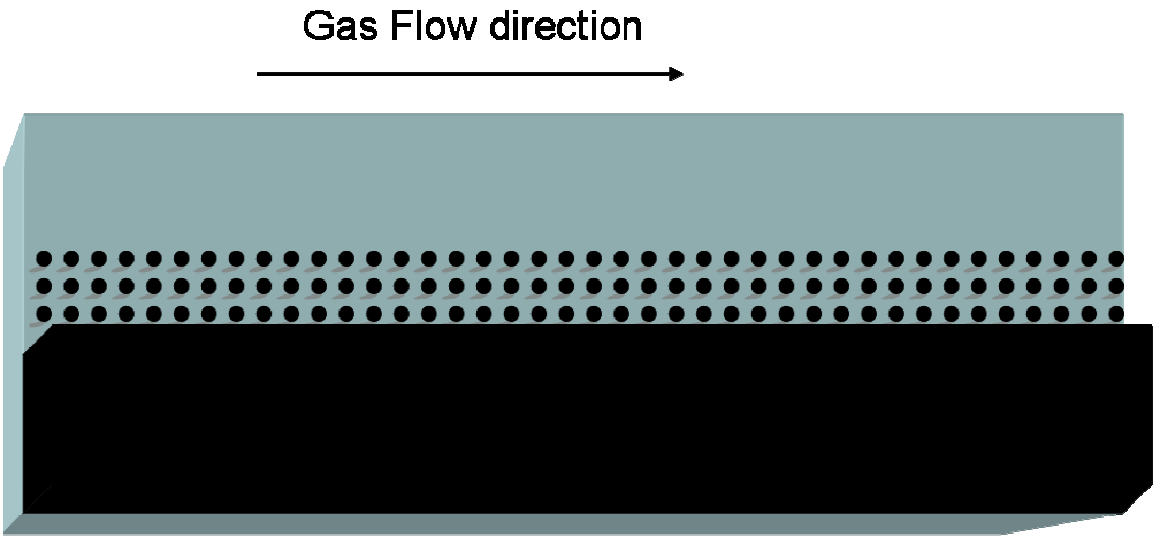

Figure 3.1. The substrate is divided by three parts. One third of the substrate is the tin film coated region, one third of the substrate is tin particle coated part and one third of the substrate has no catalyst.

Figure 3.1 shows that the substrate coating diagram. One third of the substrate is coated with tin film, one third of the substrate is coated with tin particles, and one third is clean substrate without coating. The substrate temperature ranged from 650ºC-850ºC.

Figure 3.2 is a group of typical SEM images of the ZnO nanostructures at 850º C with gas flow rate at 15 sccm (standard cubic centimeters per minute). At the same temperature region, very different ZnO nanostructures deposit on the different substrates. Large faceted ZnO particles cover the surface of the clean mica substrate as Figure 3.2a. In contrast, mica substrates initially covered with tin particle seeds exhibit short nanowires with a conical shape at this region as shown in Figure 3.2b. The nanowires are 1-2 micrometers in length, and around 100nm in diameter. All the nanowires are formed on flat hexagonal-shaped ZnO platforms and perpendicular to the substrates. On the other

hand, mica substrates covered with thick tin films show the belt shape structures presented in Figure 3.2c. The images suggest that deposited materials have a certain relationship with catalyst thickness. The belt shape structures have 1-2 micrometers in width, 10 micrometers in length, and a thickness below 100 nm. The experimental condition is same for these different substrates. The images show that the thicker catalyst has more material deposited.

Figure 3.3 records that various ZnO nanostructures form on three different substrates at temperature of 750^{o}C. Figure 3.3a describes the faceted shape particles on the clean mica substrate. The structure is similar to 850^{o}C region although the temperature is lower. Well aligned shape zinc oxide nanowires form on the thin coating mica substrate in Figure 3.3b. The uniform nanowire diameter is about 100nm and the average length is about 5 micrometer. The orientation of nanowires is perpendicular to the (001) mica substrate. The nanowire is longer in this temperature zone compare with the product in 850ºC. Large thin nanobelt nucleates on the thick coating mica substrate as shown in Figure 3.3c. The length of nanobelt is more than 10 micrometers, the width is 3-5 micrometers, and the thickness is below 50nm. The nanobelts in this temperature region are wider and longer than nanobelts at 850ºC, likely because of the greater source material.

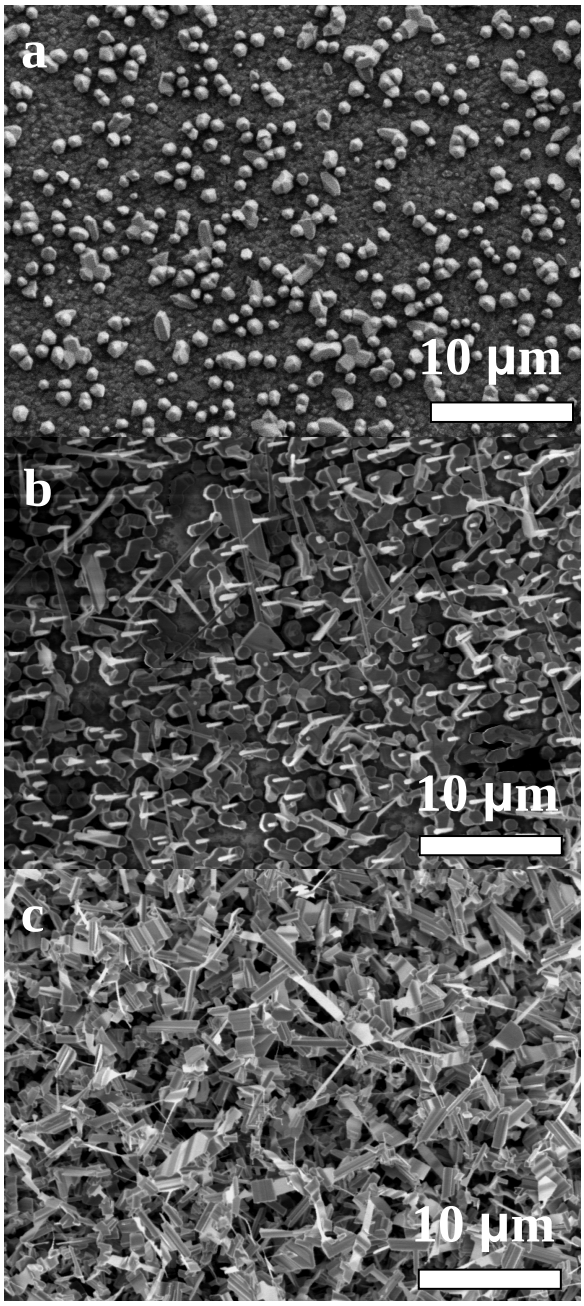

Figure 3.2. Various ZnO nanostructures were fabricated at 850ºC on the different substrates. ZnO particles deposit on the clean substrate without coating as shown in Figure a. Short aligned nanowires with conical shape form on the tin particle coated substrate as shown in Figure b. Belt shape structures are concentrated in the thick tin film coated substrate as shown in Figure c. All the experimental conditions are the same except for the catalyst coating.

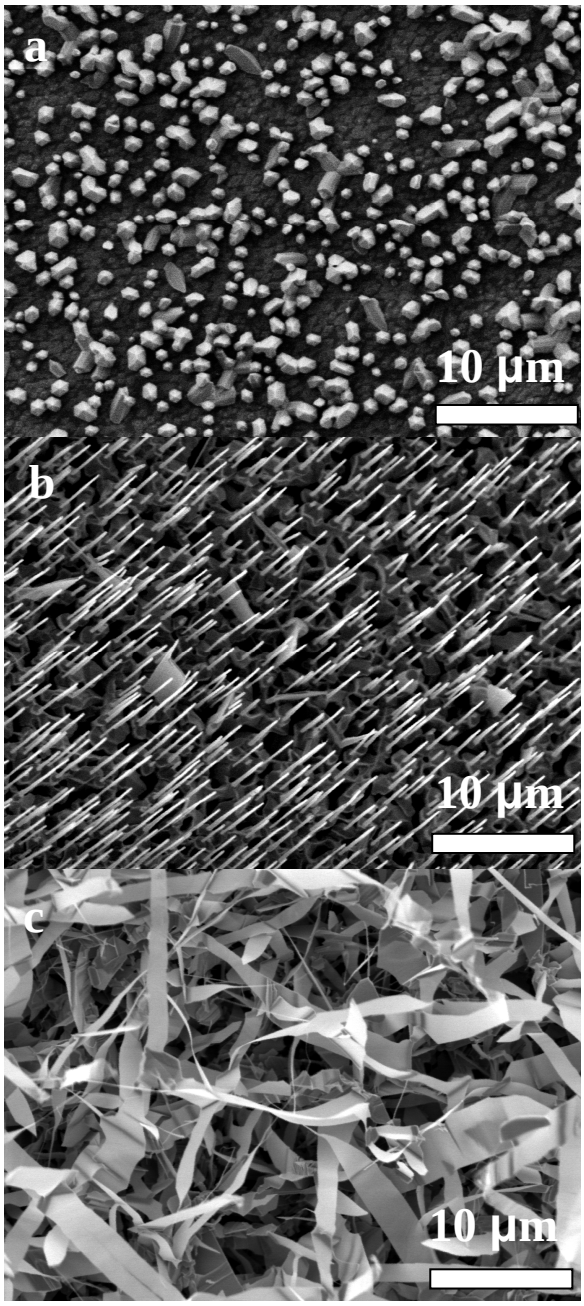

Figure 3.3. Various ZnO nanostructures are fabricated on 750ºC on the different substrates. ZnO particles deposit on the clean substrate without coating as shown in Figure a. Figure b exhibits the long aligned nanowires on the tin particle coated substrates. Figure c shows that belt shape structures are formed on the thick tin film coated substrates.

Figure 3.4 is a representative group of images for different nanostructures on three substrates at 650^{o} C region. Figure 3.4a records similar shape structures as before on the clean mica except the concentration is higher than previous results. Some particles are connected together and form honeycomb structures. More source vapor deposits in this temperature region than 750^{o}C region. Long nanowires randomly orient on the thin film coating mica substrate (Figure 3.4b). The diameter is similar to the well aligned nanowires at 750^{o} C region. The length is more than 20 micrometers but orientation is not uniform. Figure 3.4c shows that on tin film coated substrate, big nanorods are present in this temperature zone. The length of these nanorods is more than 20 micrometers and the diameter is around 1 micrometer.

On the clean mica substrates, from high to low temperature zone, there is not much change in morphologies of the final product except the density of the particles. The faceted shape of the particles means that zinc oxide has an epitaxial relationship to the mica substrate as shown in Figure 3.5. Vapor solid growth mechanism is the main growth process in regions free of catalyst. Zinc oxide vapor nucleates on the mica surface directly, and forms a minimum surface energy shape. From 650^{o} C to 850^{o} C, different shape structures form in different temperature regions. Individual faceted particles are found at 850^{o} C region, denser faceted ZnO particles deposit at 750^{o} C region, and thick continuous film shaped structures form at 650^{o} C.

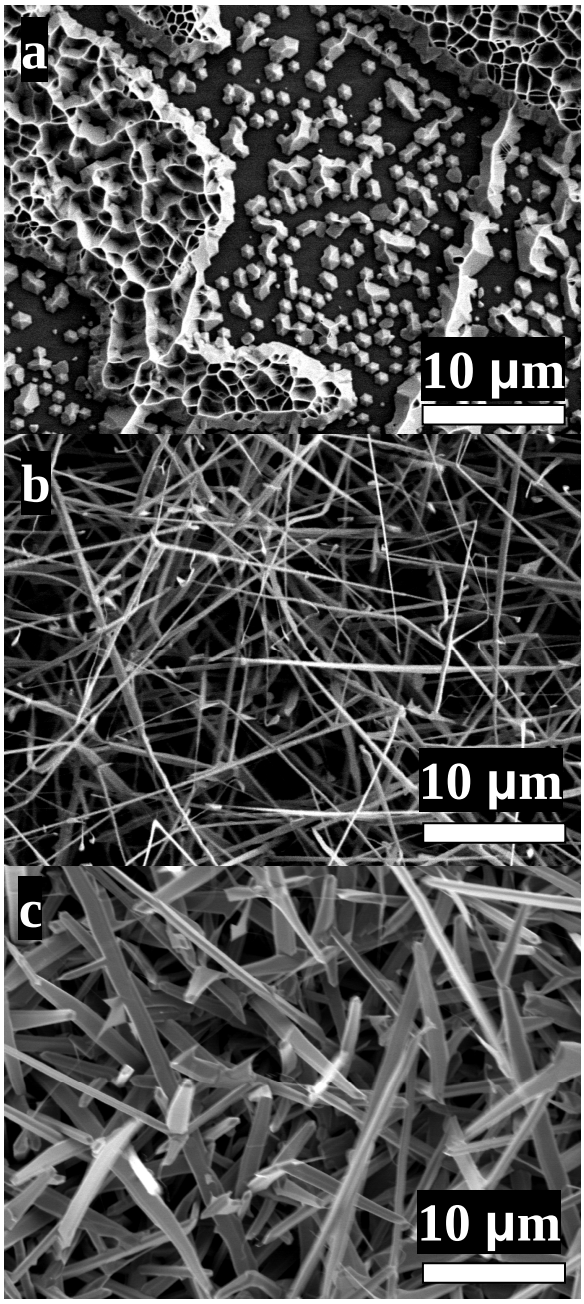

Figure 3.4. Various ZnO nanostructures are fabricated on 650ºC on the different substrates.

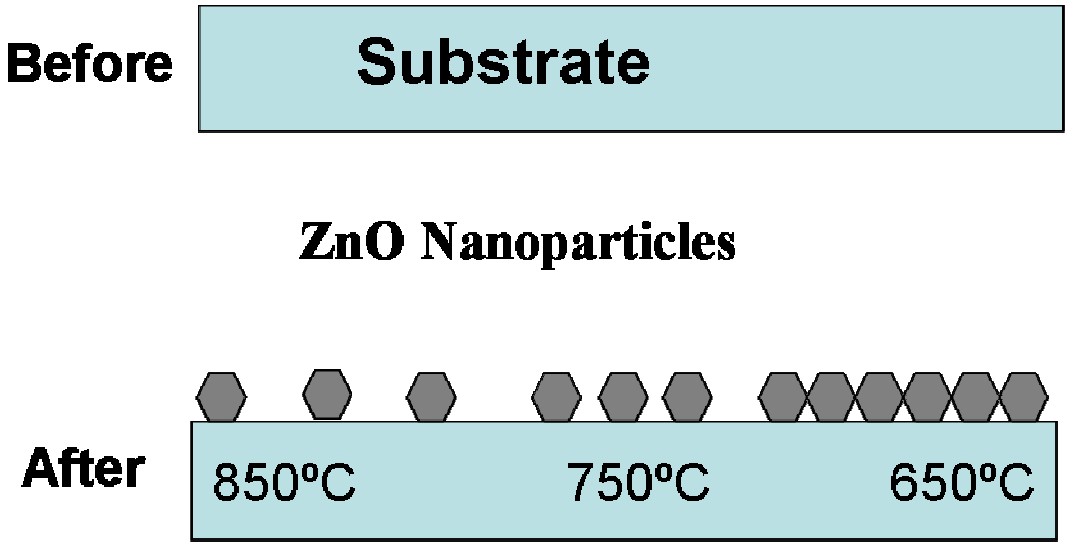

Figure 3.5. The diagram shows that faceted individual nanoparticles formation process on mica substrate.

On the tin particle coated mica substrate, nanostructures change from short zinc oxide nanowires to aligned zinc oxide nanowires and long nanowires without preferred orientation. At high temperature region, very small amount of source vapor deposit on the substrate and form aligned nanowires as shown in Figure 3.6. In lower temperature regions, longer aligned zinc oxide nanowires form because more source material deposits in this temperature zone.

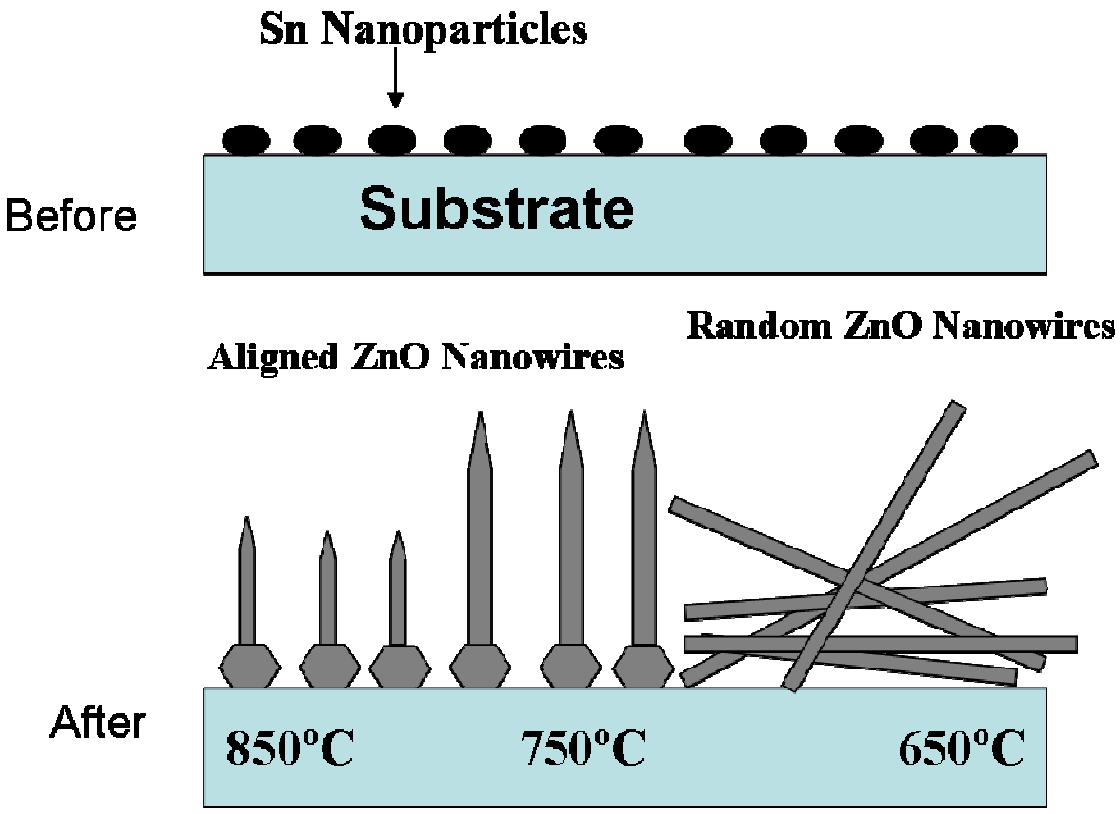

Figure 3.6. The diagram shows that aligned nanowire formation process on tin particles coated mica substrate.

Morphologies of nanostructures on the tin film coated mica also change from high to low temperature gradually. From small nanobelt, big nanobelt to nanorods, the variance is relative to the substrate temperature decreasing. In high temperature region, source vapor is absorbed by the tin film and nucleates on the substrate to form the belt shape. At lower temperature region, more source vapor is absorbed than high temperature region, which results in the large thin nanobelts found at this area, as shown in Figure 3.7.

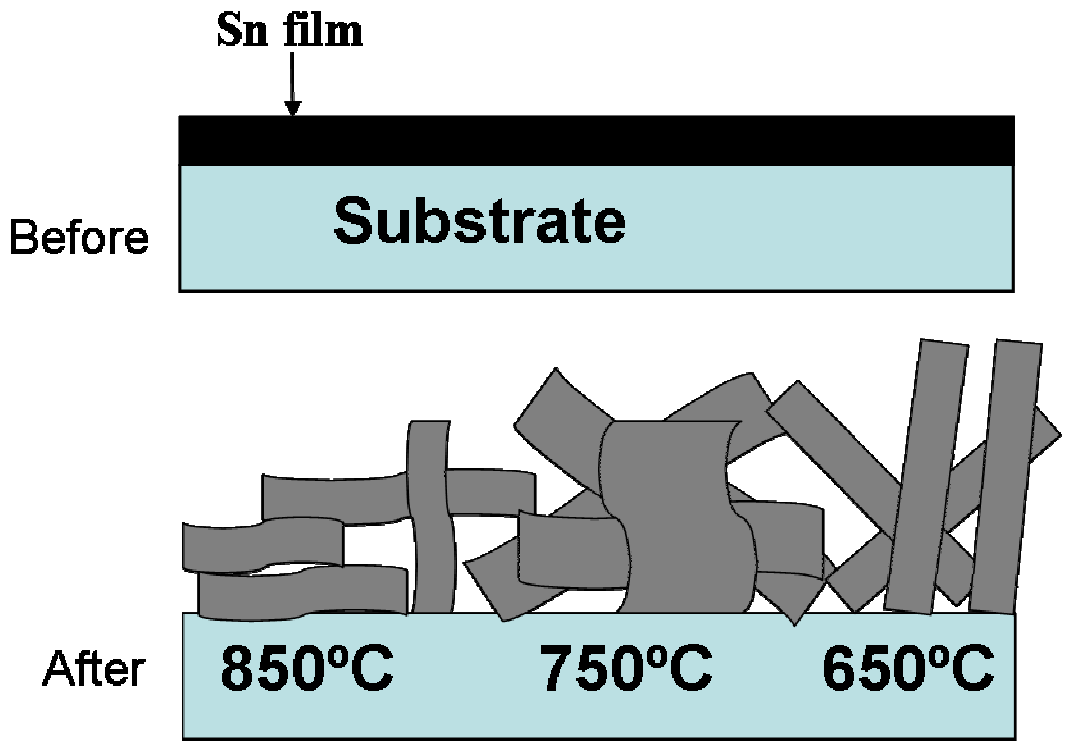

Figure 3.7. The diagram shows that nanobelt formation process on thick tin film coated mica substrate.

Substrate temperature has a big impact on the morphology of the nanostructures from the SEM images (Li et al. 2006; Umar et al. 2007). On the other hand, in the same temperature region, the nanostructures morphologies are mainly determined by the substrate material since other parameters are quite similar. The morphologies of the final products are different due to the catalyst thickness difference.

On the catalyst substrate, the nanostructure growth process is via vapor liquid solid and vapor solid mechanism (Pan et al. 2001). When the temperature is high enough, source material is vaporized. The vapor of the source material diffuses away from the center area due to the high pressure. Source vapor is highly sensitive to the temperature.

At high temperature, vapor has a small chance to nucleate and deposit. In low temperature regions (below 300ºC) a very small amount of vapor arrives since most of the material is absorbed by the substrate upstream.

The thickness of the catalyst determines the amount of source material initially deposited on the substrates. Thicker coated substrates absorb more source material vapor directly than the thinner coated substrates under the same experimental conditions. The zinc oxide film forms after absorbing enough material. Tin and zinc oxide alloy supersaturates and the zinc oxide nanobelt deposits on the sites (Li et al. 2003b; Zhang et al. 2005). Nanobelt size and shape is determined by the amount of directly absorbed source vapor. This is why at 850^{o} C, tin particle coated substrates have zinc oxide nanowires and thick coated tin film substrates have nanobelts.

At 750^{o} C, source material increases a lot compare to 850ºC temperature region. On tin particle coated substrates, source material is concentrated in this region and forms long nanowires. On tin film coated substrates, tin and zinc oxide alloy absorbs more source vapor at 850ºC and we get big nanobelts.

At 650° C region, a relative small amount of vapor reaches this region and nucleates on the substrates. Both tin particle coated substrates and tin film coated substrates show long nanowires or nanorods. Again, the tin film coated area absorbs more material than tin particle coated area and clean substrates. The diameter of the nanowires in tin film coated regions is larger than in the tin particle coated region. Only a small amount of source vapor deposits on clean mica directly. This is why there is little variation with the temperature on clean mica.

Figure 3.8 shows the interface between zinc oxide nanoparticles, and aligned zinc oxide nanowires, in the same substrate temperature region. All the experimental parameters are same except substrate coating. On clean mica, only zinc oxide nanoparticles are nucleated. In contrast, aligned zinc oxide nanowires are found on the tin particle coated region.

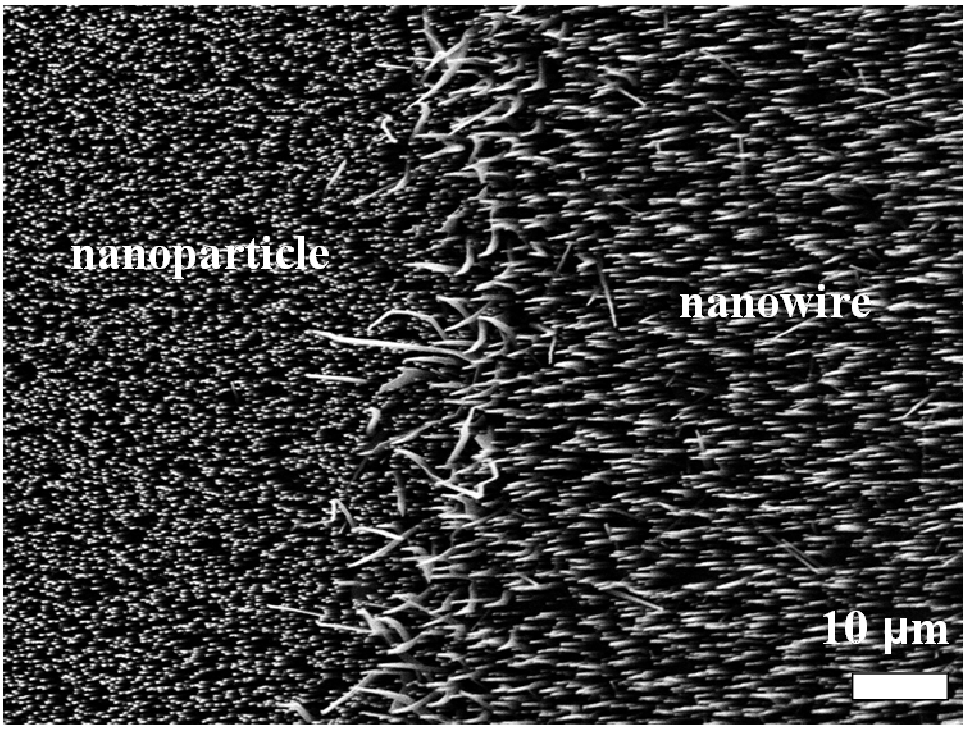

Figure 3.8 Low magnification SEM image shows the interface between nanoparticles and aligned zinc oxide nanowires.

Figure 3.9 shows that at the interface between tin particle and tin film coated substrate, zinc oxide nanowire and zinc oxide nanobelt make a clear transition. Thus catalyst thickness difference results in very different structures.

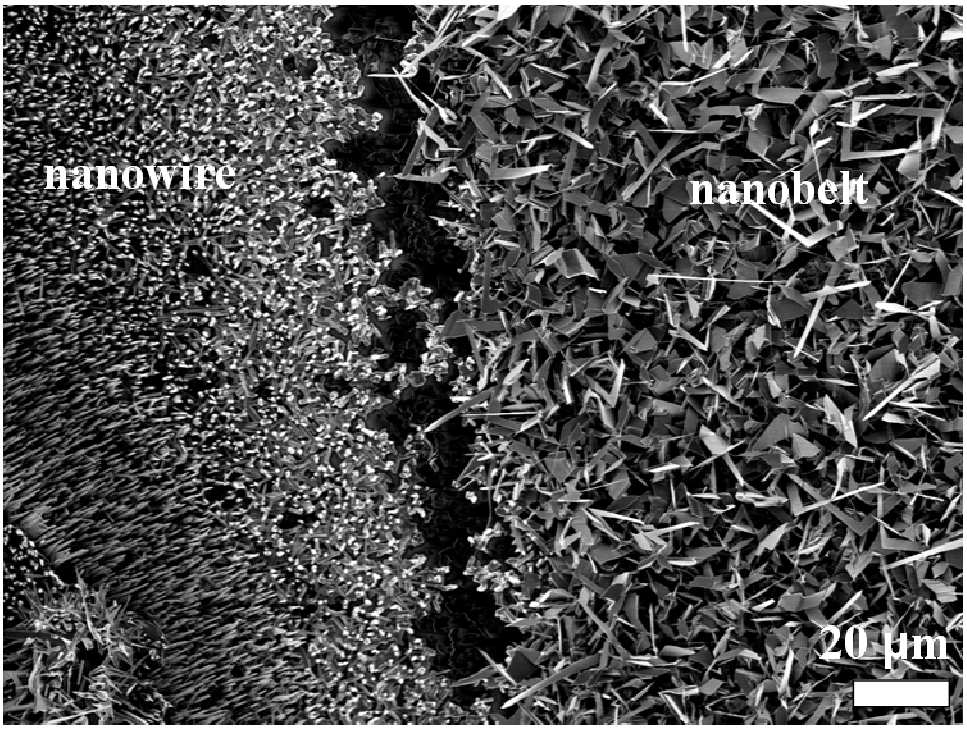

Figure 3.9 Low magnification SEM image shows the interface between aligned zinc oxide nanowires and zinc oxide nanobelts.

In summary, various zinc oxide nanostructures were synthesized in a vapor transport deposition system on different thickness catalyst coated substrates. Catalyst thickness decides the capability of the substrate to capture source vapor. The deposited source amount helps determine the final structures. On clean mica, limited source vapor is absorbed. There are no nanobelts or long nanowires on the surface. On tin particle coated substrates, the amount of source material absorbed results in short aligned nanowires, long aligned nanowires, and randomly oriented nanowires. Similar variation is found on the tin film coated mica substrate. The final structures are mainly determined by the absorbing vapor amount. The thickness of catalyst has a direct impact on the absorbing coefficient.

PAPER
4. VERTICALLY ORIENTED ZINC OXIDE NANOCONTAINERS GROWN ON MICA SUBSTRATES

(Coauthor: J. Liu)

ABSTRACT: A simple chemical vapor deposition method has been used to fabricate hollow zinc oxide structures. The process begins with a clean mica surface without any metal catalyst. The vapor solid growth mechanism determines the final states. A simple fabrication method makes an enabling technology, for applications in electronics and pharmaceutical research.

Zinc oxide nanostructures have been synthesized and investigated by many groups due to their potential applications in optoelectronics (Huang et al. 2001a), sensors (Yu et al. 2005), and nanoscale heterojunction (Park et al. 2003). Uniform size and shape are very important for all applications. Here we demonstrate a simple method for the fabrication of zinc oxide nanocontainers. The process takes place on the clean mica substrates. Mica plays an important role for growth of aligned shape zinc oxide nanostructures, since it is a layered silicate material with highly ordered surfaces whose layers are parallel to (001) planes. The container shape has strong potential for use in drug delivery.

A simple procedure was devised for nanocontainer growth. Wang et al. synthesized zinc oxide nanocastles through carbon-thermal evaporation method (Wang et al. 2006b). The shapes of products are similar, but our nanocontainers are much smaller than theirs. The same mass of zinc oxide powders mixed with carbon black as the source

materials. The source material was loaded into an alumina tube furnace. A fresh cleaved mica sheet was put downstream of the argon gas flow direction. After purging the tube using argon gas for about 20 minutes, the furnace was heated up to 1000ºC at the rate of 20^{o} C/min. At the same time, the gas flow rate was set to 20 sccm. The temperature and gas flow were held constant for about 60 minutes. Then the furnace was turned off and the system cooled down quickly. Zinc oxide nanocontainers are obtained at the 700ºC-800^{o} C.

The nanostructures are characterized by scanning electron microscope. Figure 4.1 (a) is a low magnification SEM image showing the uniform distribute aligned growth container shape structures. Figure 4.1 (b) shows that each container size is around 200-400nm. Most of the containers are empty inside and have hexagonal outer edge shape walls. The wall thickness is below 100nm.

While investigating some lower temperature regions, we found that some of the nanocontainers are covered and form hexagonal shape columns (Figure 4.2). Below 20nm in diameter nanofibers grow in the center of these containers. From Figure 4.2, the container is covered gradually until totally covered since some of the containers are partly covered in Figure 4.2b.

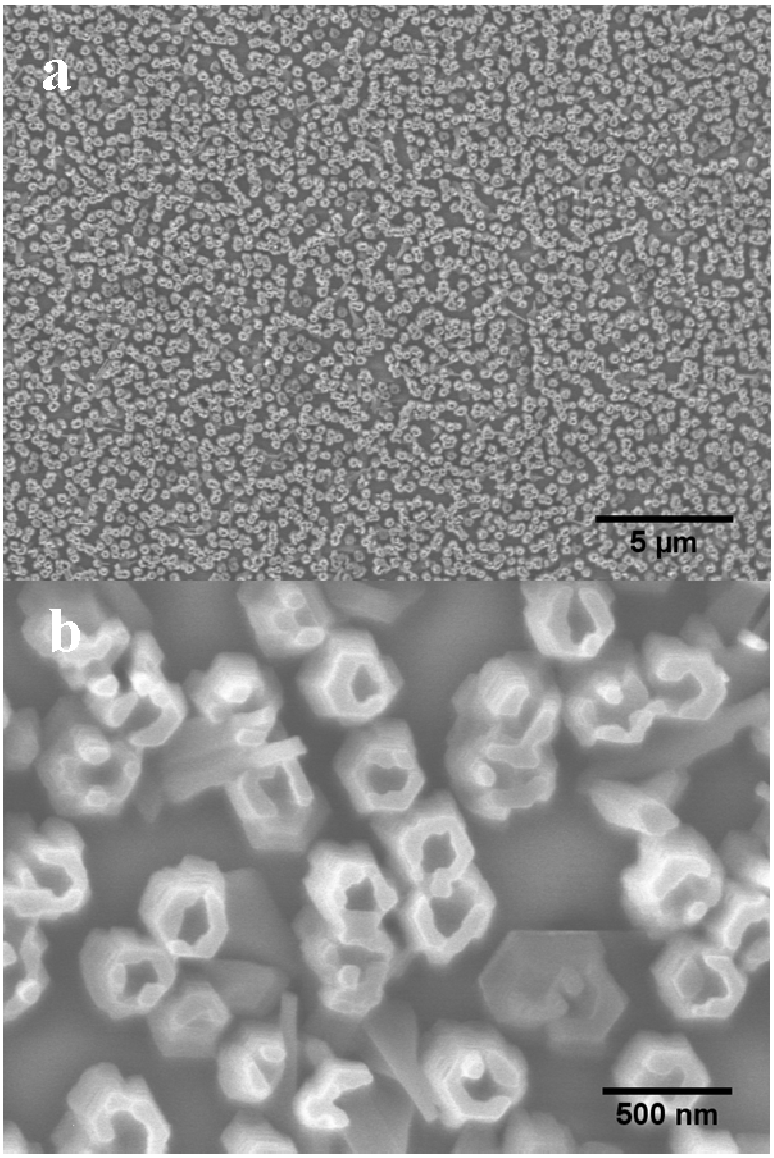

Figure 4.1. (a) Low magnification SEM image of zinc oxide nanocontainers grown on mica substrate; (b) higher magnification SEM image of top view nanocontainers (2007, J. Liu).

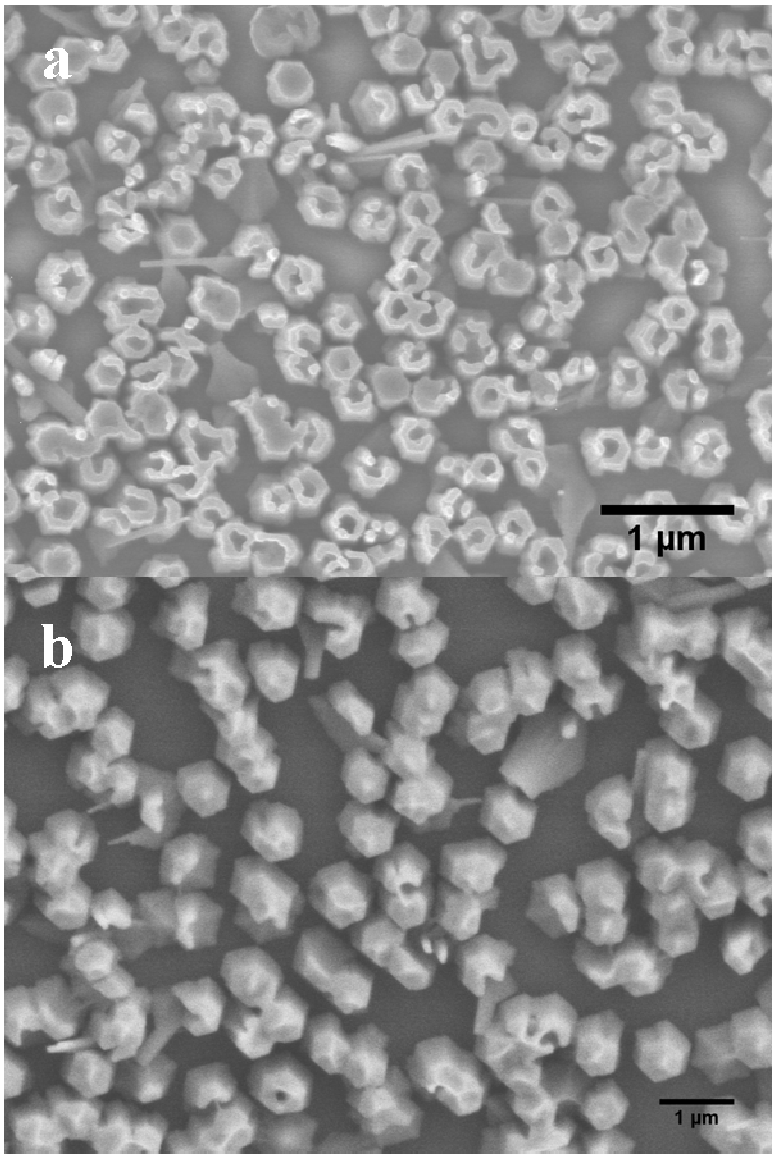

Figure 4.2. (a) Some of nanocontainers are covered (2007, J. Liu); (b) most of the lids are covered and form a tip on each container.

Another experiment used the same process except the gas flow rate was set to zero after temperature reached 1000ºC. The scanning electron microscope recorded the results, as shown in Figure 4.3.

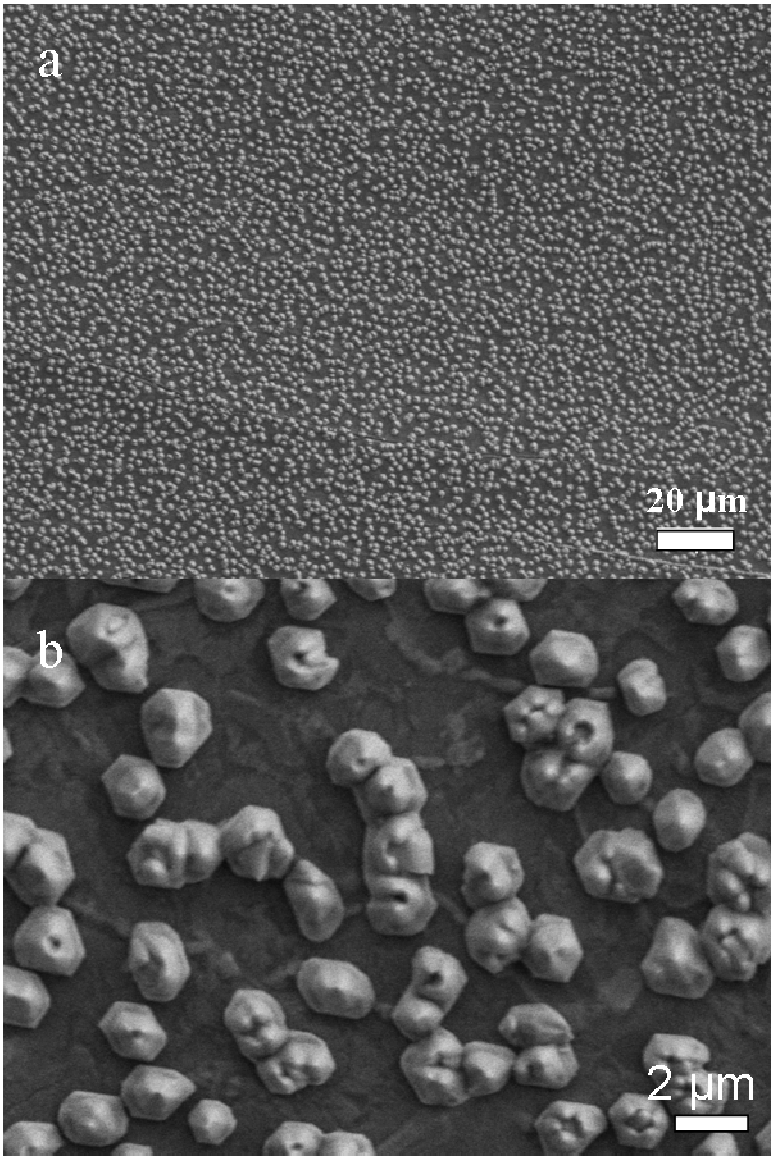

Figure 4.3. SEM images of cone shape nanocontainers. (a) is the low magnification SEM image of the containers. High magnification SEM image (b) shows that the diameter of the container is around 2 micrometers.

From the low magnification SEM image Figure 4.3, we can see the distribution of zinc oxide containers. These containers have a hexagonal shaped base, as in the last

experiment. Different from the previous results, most of “wall” parts of the containers are very short, which may be because much less source vapor is collected by the sites in comparison with the last experiment.

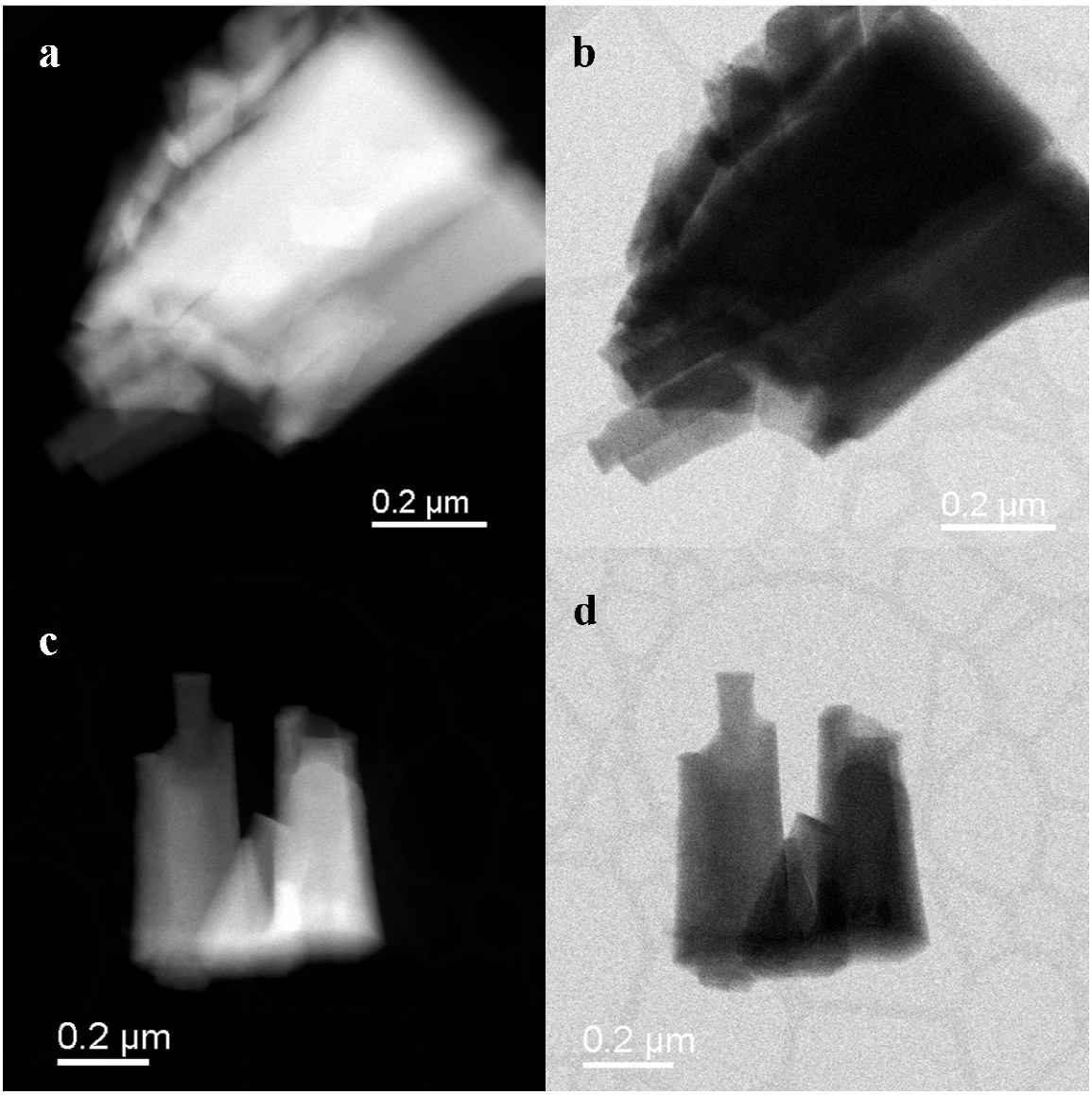

Figure 4.4. Scanning transmission electron microscope images of zinc oxide nanocontainers. (a) is high angle annular darkfield image of the container and (b) is the bright field image. (c) is high angle annular darkfield image of another container and (d) is the bright field image (2007, J. Liu).

Zinc oxide nanocontainers were investigated by scanning transmission electron microscope as shown in Figure 4.4. Figure 4.4a shows a typical low magnification dark field image of container shape structures. Figure 4.4b shows the bright field image. From the images, we can tell the shape is consistent with SEM results. The structure has solid hexagonal crystal base and rods or belts shape surrounding the base. The diameter of the base is around 1 micrometer.

In lower temperature regions, more source material vapor nucleates on the products. The nanocontainers are closed. On possible model: Zinc oxide nanocrystals first deposit on the mica surface, and form a minimum surface energy shape (Figure 4.5). Later source materials build on the hexagonal base directly. When the source temperature decreases, much less source material is evaporated. Some of the containers absorb vapor and form closed containers with needle-shaped structures on the top. Some of the containers are not fully covered.

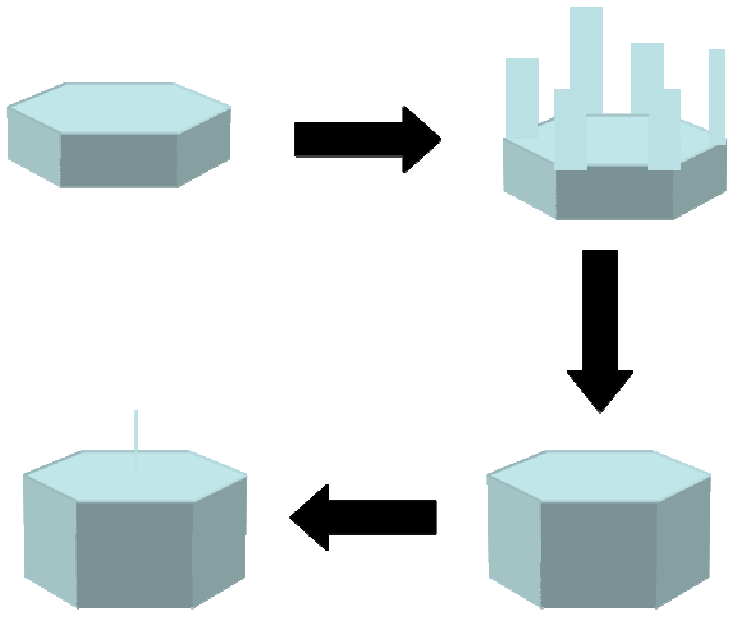

Figure 4.5. Schematic steps of formation of nanocontainers.

Since no catalyst particles are used in our experiment, it is clear that the synthesis proceeds via the vapor solid process. Zinc oxide atoms nucleate on the substrate surface first and form nanocrystallites. The width of the containers becomes smaller and smaller, with nucleation of more and more zinc oxide layers. The last layer of zinc oxide fully covers the nanocontainers.

In conclusion, we have successfully grown vertically oriented zinc oxide nanocontainers on clean mica substrates using simple chemical vapor deposition method. Clean mica sheets are keys for the epitaxial growth. These nanocontainers have uniform size and shape. More investigation is needed to find the relationship between the first layer of nanocontainers and mica substrates. More work is needed to find different products on the catalyzed mica substrates. Since mica is easy to cleave, it will be a good candidate for nanomaterials fabrication. This simple synthesis method may also be easy to be applied to other nanomaterials.

3. SUMMARY AND OUTLOOK

A systemic study has been conducted in the synthesis and characterization of nanoscale materials. We have achieved several goals. Using the digital darkfield imaging analysis method, we can quickly identify the lattice fringe relationship between catalyst particles and carbon nanotubes. Various controllable zinc oxide nanostructures have been synthesized through thermal evaporation. Atomic structure relationship between gold catalyst particles and zinc oxide nanowires have been analyzed through aberration corrected scanning transmission electron microscopy and energy dispersive X-ray nano-analysis. Catalyst effect on the final products has been investigated by scanning electron microscopy.

3.1. NANOSTRUCTURE APPLICATIONS

Our work is not just about getting nanoscale materials. More importantly, we want to understand the formation mechanism of these structures. We further utilized zinc oxide nanostructures synthesized in our system to do some fuel cell experiments.

Zinc oxide nanobelts or nanoribbons are perfect candidates for the support of the catalyst particles, due to their special morphology. Catalyst particles are easily attached to the nanobelts and stabilized. Here we put palladium particles on a ZnO surface to be used as catalyst for onboard steam reforming of methanol to produce hydrogen gas (Iwasa et al. 1995).

After putting the palladium particles on nanoribbons, there is no clear change for the zinc oxide nanobelts in low magnification scanning electron microscope image as shown in Figure 3.1. High resolution SEM images (Figure 3.2) reveal palladium particle

size and distribution. The average diameter of the palladium particles on the ribbon supports was 20nm.

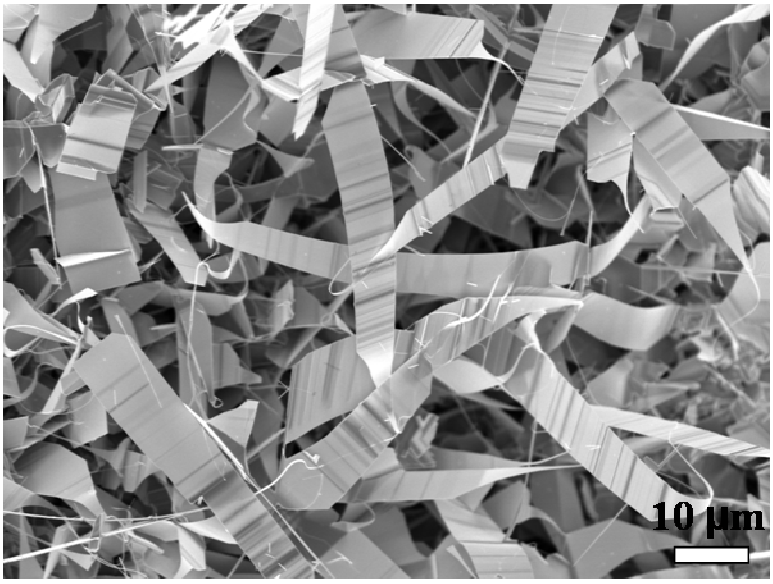

Figure 3.1 Low magnification SEM image of Pd particles on zinc oxide nanobelt (2008, J. Liu).

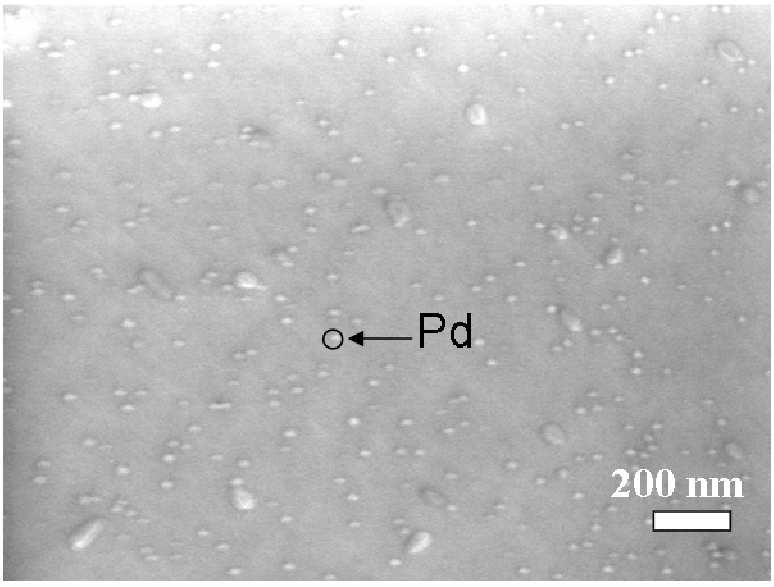

Figure 3.2 High magnification SEM image of Pd particles on zinc oxide nanobelt (2008, J. Liu).

More structure information can be revealed by scanning transmission electron microscopy. In Figure 3.3, images give us clear image of Pd particles located on various

places of zinc oxide nanobelt. After heat treatment, the palladium and zinc alloy is formed on the zinc oxide nanobelt as shown in Figure 3.3 c and Figure 3.3.d.

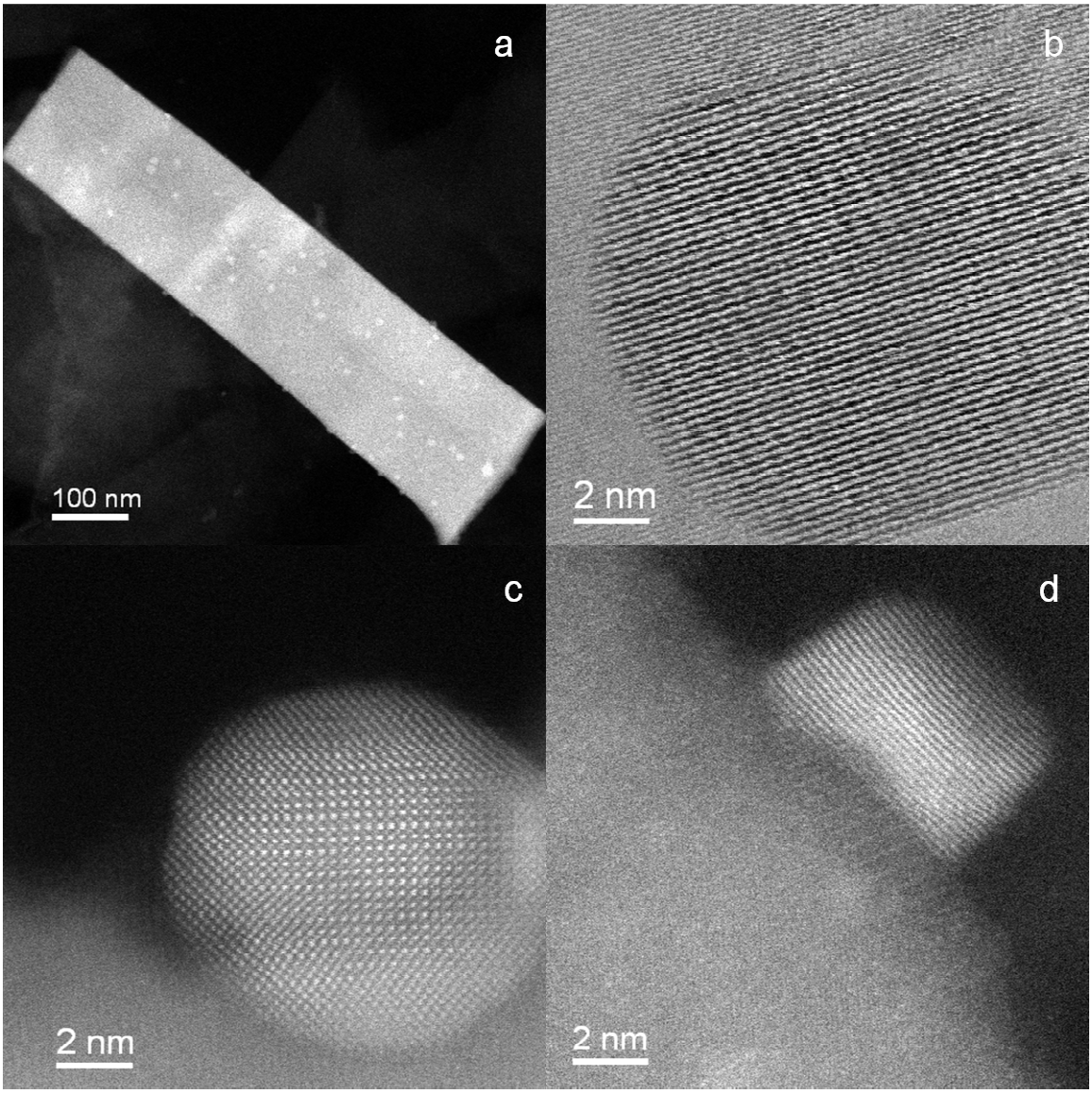

Figure 3.3 (a) Low magnification high angle annual darkfield STEM (HA-ADF) image of Pd on ZnO nanobelt. (b) High magnification STEM bright field image of Pd particle on the center of the nanobelt. (c) and (d) are HA-ADF images of Pd particle on the side of the nanobelt (2008, J. Liu).

This is one of the applications of the zinc oxide nanobelts in our experiment. More and more application in other areas will be developed by researchers later.

3.2. CHALLENGES AND OUTLOOK

We have investigated the structure relationship between gold catalyst particles and zinc oxide nanowires. Some literature has reported that the orientation of nanowires is determined by the substrate lattice parameter. Most of their work is based on theoretical calculations. High resolution TEM work is needed to solve the problem.

Another problem is tin induced zinc oxide nanobelts. Under scanning transmission electron microscope, the nanobelts are single crystal and without defects. Our tin catalyzed nanobelts have standard ZnO structures as shown in Figure 3.4.

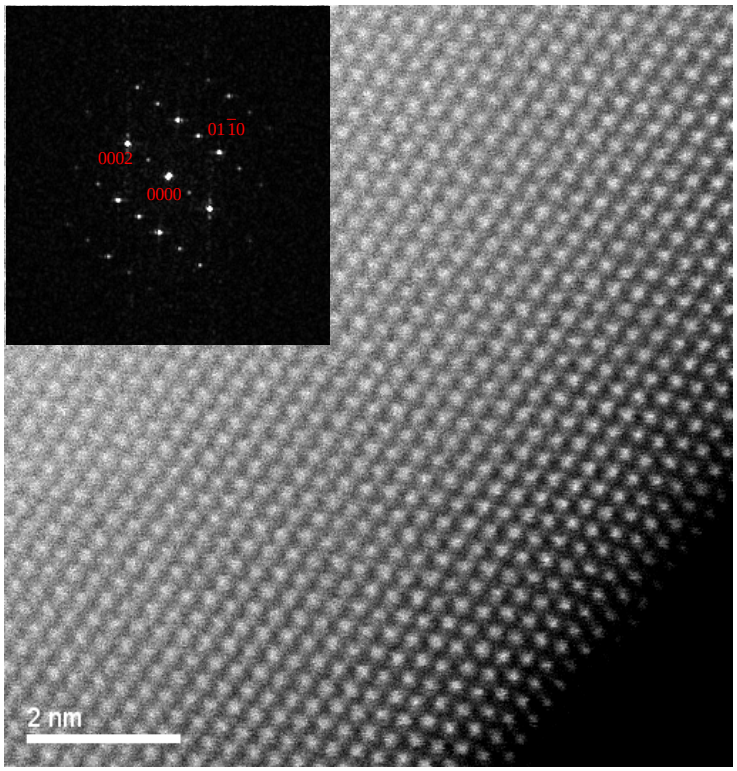

Figure 3.4. High resolution STEM image of tin catalyzed zinc oxide nanobelt (2007, J. Liu).

From energy dispersive spectra obtained from the zinc oxide nanobelts, we could not find the tin signal as shown in Figure 3.5. The Ti peak comes from a Ti TEM support grid. Hence future work is needed to investigate the interface between the belt and the tin catalyst particles on the substrates.

From our work, we get some results but we also encounter many challenges. Some difficulties come from experimental designs and operations. Some difficulties come from the challenge of explaining experimental results.

Delicate instruments must be designed to control the experiments more carefully. The problems originate from the repeatability of the experimental results by the same parameters. Part of the problem arises because the nanostructures are so sensitive to minor changes of the parameters like gas flow rate, source material temperature, and substrate temperature etc. Compared with the traditional low pressure chemical vapor deposition experiment setup, our experiment minimizes the influence of pressure variation. Still effects are apparent in the experimental results. Delicate instruments will be needed for a wider range of nanostructure synthesis work.

In understanding the formation mechanism for various structures, vapor-liquid-solid, vapor-solid, and vapor-solid-solid mechanism have illustrated some results. In situ observation during growth may help to confirm the theory. Also some of the results are artistically impressive, but remain hard to explain.

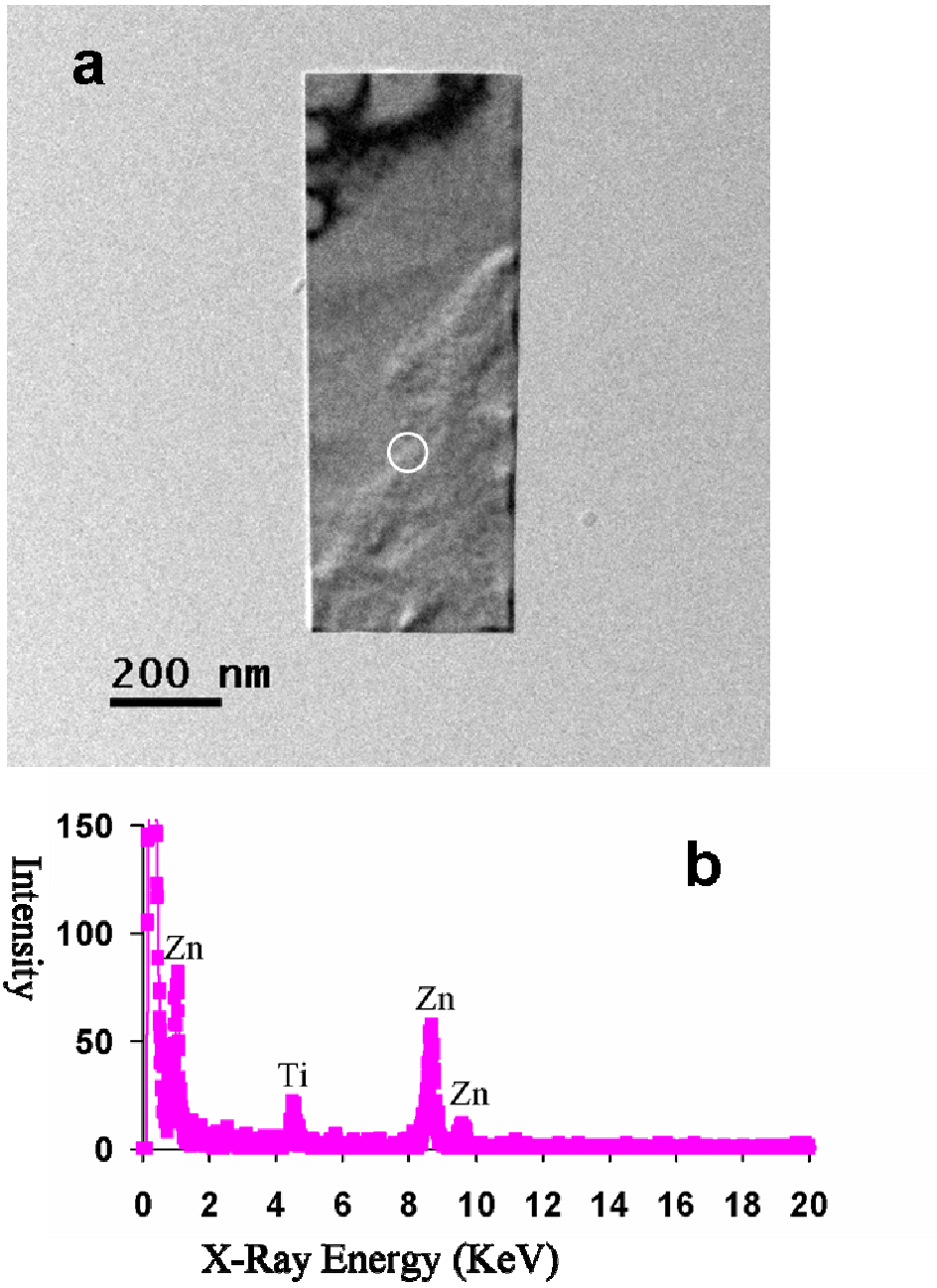

Figure 3.5 (a).Low magnification transmission electron microscope image of zinc oxide nanobelt supported on a continuous carbon film. (b). Energy dispersive spectra obtained from the zinc oxide nanobelt.

In our experiments, we synthesized aligned zinc oxide nanowires, zinc oxide nanobelts, castles and long fibers. We also get some byproducts like zinc oxide hollow spheres. In the SEM images, the diameter of the spheres is around 500nm. Some of the spheres are partly open as shown in Figure 3.6. There are some particles on the sphere surface. In order to identify if the sphere is solid or hollow, we put the sample into the transmission electron microscope. Under TEM, we find that most of the spheres are hollow shape, as shown in Figure 3. 7.

It is hard to understand the process of hollow sphere formation. In our experiment, we did not intentionally design hollow spheres.

Besides hollow spheres, there are many interesting morphologies formed in our experiments as shown in Figure 3.8. High symmetry triangle shaped zinc oxide rods have been observed as shown in Figure 3.8a. The length of the rod is around 40 micrometers. It is very interesting to find that the structure has rods in three symmetric directions. Hexagonal zinc oxide rod cross-section is also observed as shown in Figure 3.8b. The nanorod has six sides, and at the top the rod there is a tip. Figure 3.8c shows that nanorod flower-like structures. The nanorods have similar length and originate from the same point. Another kind of flower-like structures is also shown from our experiments in Figure 3.8d. Different from the rod shape, the structures have flake structures attached together.

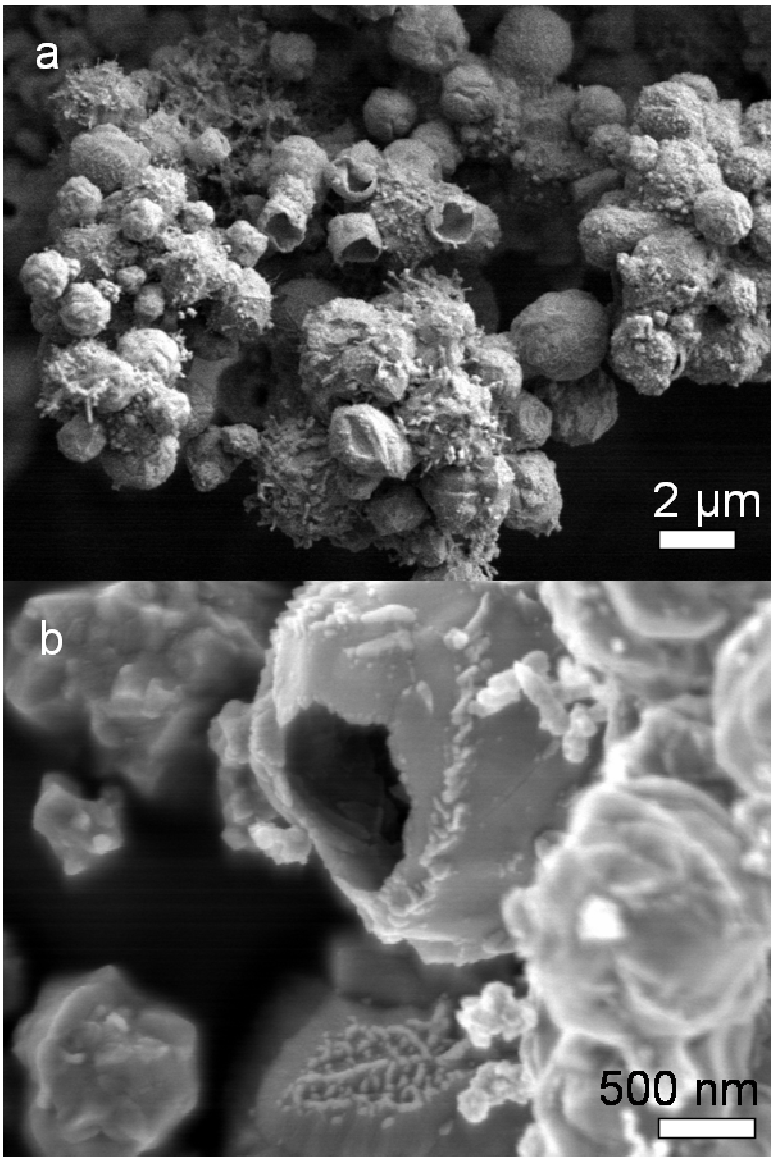

Figure 3.6 SEM image of zinc oxide hollow sphere structures (2006, J. Liu).

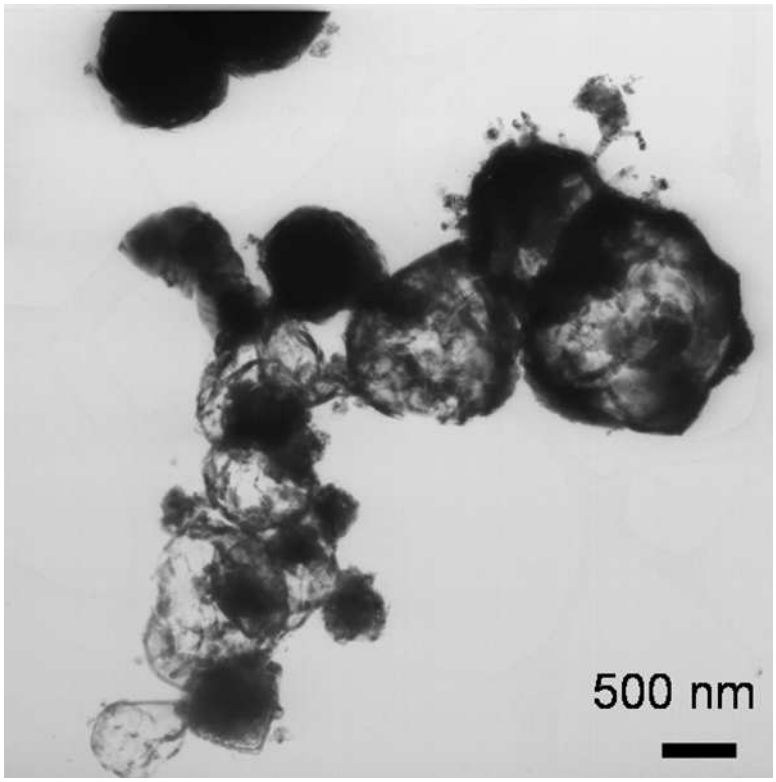

Figure 3.7 TEM image of the zinc oxide spheres. From the images, we can see that some of the spheres are hollow inside.

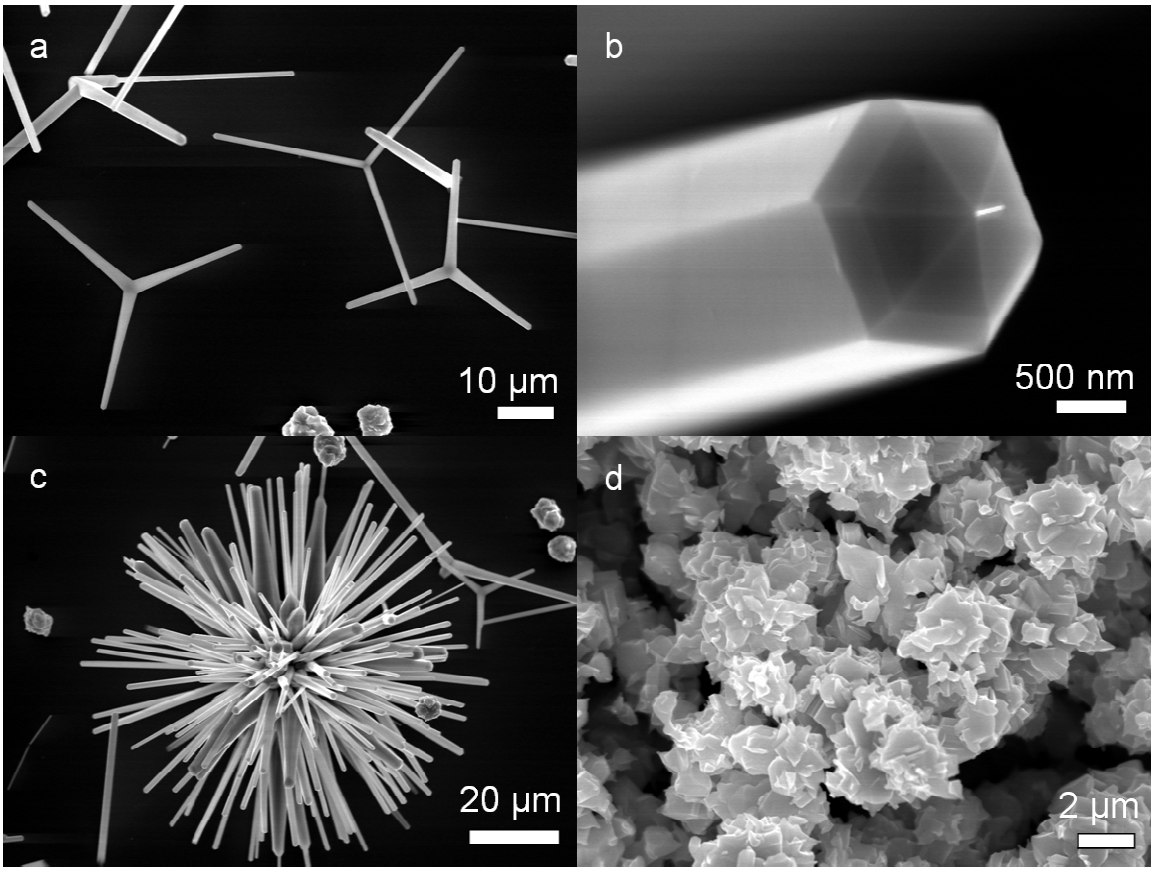

Figure 3.8 (a) Zinc oxide triangle shape needles. (b) Zinc oxide hexagonal shape nanorods with a sharp tip. (c) Zinc oxide needle flowers. (d) Zinc oxide flower like shape structures (2006, J. Liu).

Some zinc oxide structures look impressive but hard to understand, like the zinc oxide golf club structure shown in Figure 3.9. There are about two 10 micrometer diameter rings on the top and bottom sides with about 50 micrometer length fiber supported. Another one is zinc oxide fence-shape structures, as shown in Figure 3.10. The circle is about 30 micrometers in radius, and there is a cluster shape in the center of the circle. All these shape results are hard to understand.

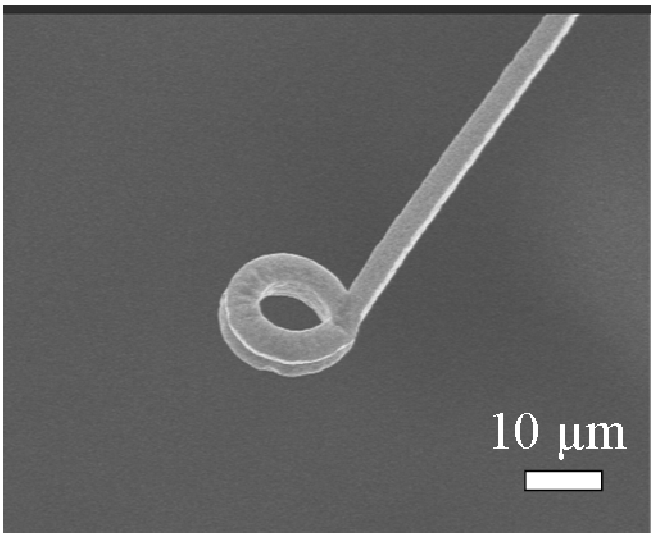

Figure 3.9 Zinc oxide golf rod shape structures (2006, J. Liu).

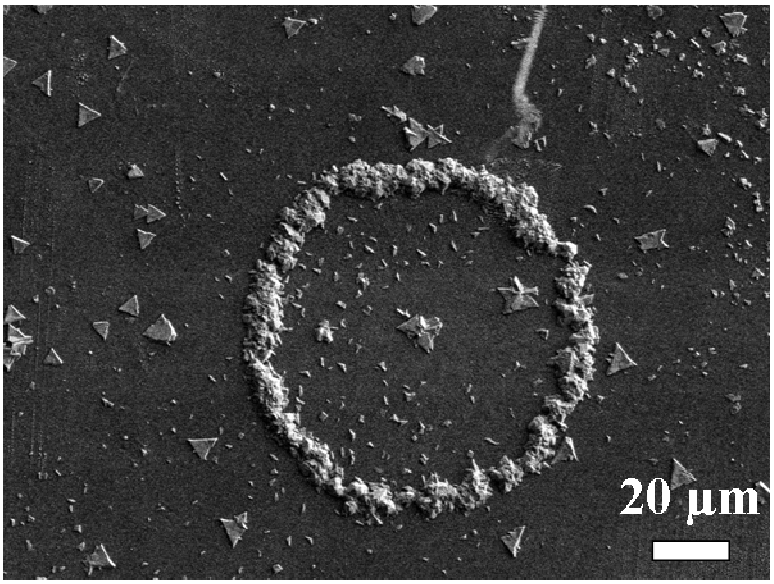

Figure 3.10 Zinc oxide fence structures (2006, J. Liu).

The foregoing structures are by-products of our zinc oxide synthesis work. Other materials have also been synthesized. The results show that we are still short of controlling the experiments. Understanding the systems, and the crystal growth mechanisms remain a challenge.

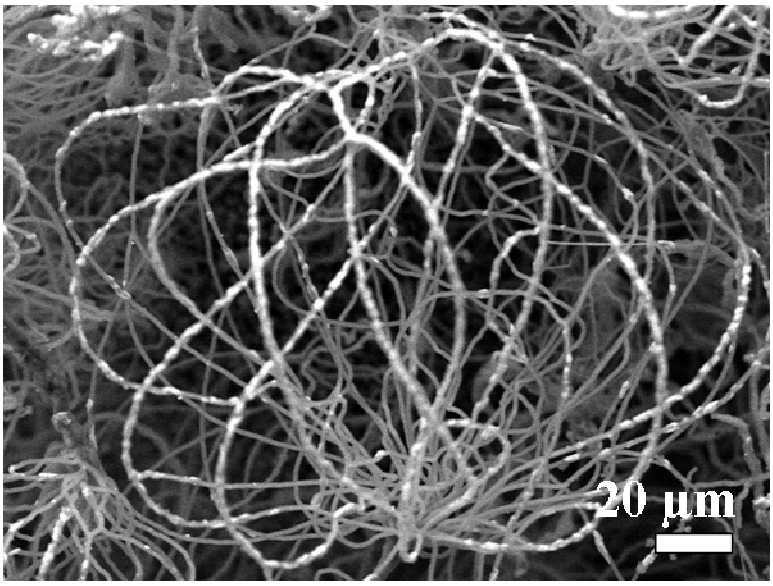

Figure 3.11 The lantern shape structures made of silicon oxide nanowire (2006, J. Liu).

Silica nanowires were synthesized in a thermal evaporation experiment. Figure 3.11 and Figure 3.12 show lantern and glasses shaped structures. These nanowires reconnect together after a comparable separation distance. How does this happen?

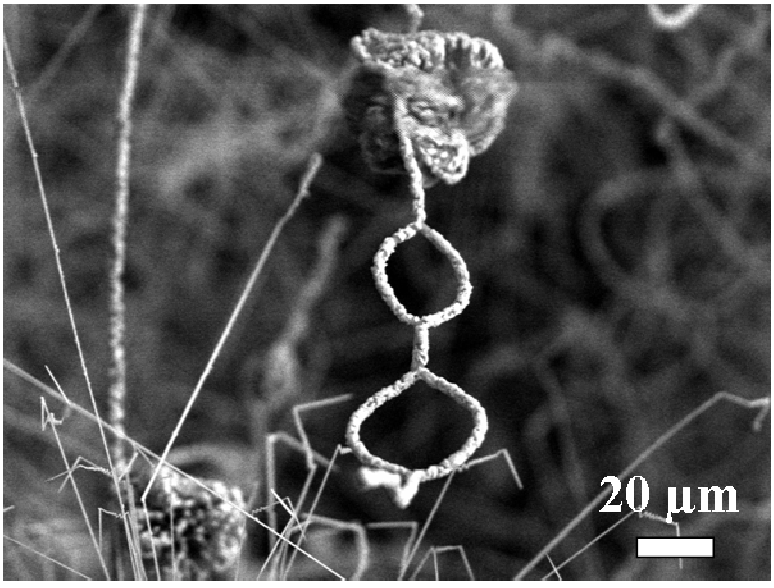

Figure 3.12 SEM image of silica “glasses”. The diameter of the glasses is around 20 micrometers (2006, J. Liu).

In our experiments, we also get zigzag tin oxide nanowires as shown in Figure 3. 13. About every 2 micrometers nanowires twist to about 75º and form the zigzag shape. The length of the nanowires is around one hundred micrometers. It is not clear how the zigzag structure forms and why this nanowire is not straight. It could happen because of minor gas flow change or temperature change. More work is required to understand the formation mechanism.

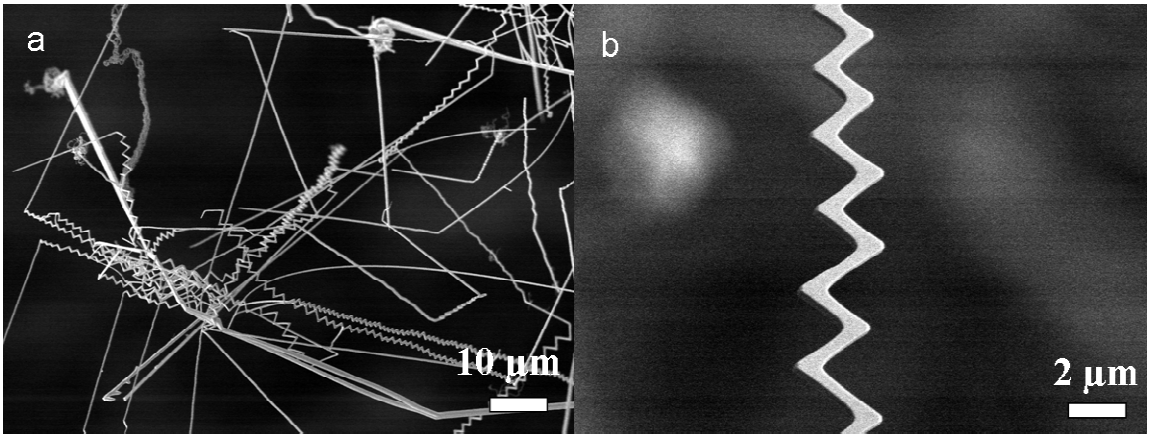

Figure 3.13 Tin oxide zigzag shape nanowires. Every about 2 micrometers there is a 75º kink and form the zigzag shape (2006, J. Liu).

This dissertation reviews novel nanoscale materials grown by thermal evaporation techniques. The various growth morphologies are summarized and characterized by electron microscope. Various growth mechanisms are proposed. These nanostructures have wide applications. The development of techniques for integration of nanostructures with other electromechanical and biosensor systems is needed.

Although there are some issues which are not well understood, with more and more work on this field people will gain deep insight. Further progress in nanoscale materials will require a closer collaboration between physicists, chemists, and biologists.

APPENDIX

SYNTHESIS AND CHARACTERIZATION OF ANTIMONY-DOPED TIN OXIDE NANOSTRUCTURES

(As appeared in Microscopy and Microanalysis (2007), pp 768)

J. Wang,[*] D. Zhou, [*,**] P. Fraundorf,[*,**] and J. Liu[*,**]

*Department of Physics and Astronomy, University of Missouri-St. Louis, One University Blvd, St. Louis, MO, 63121

** Center for Nanoscience, University of Missouri-St. Louis, One University Blvd, St. Louis, MO, 63121

INTRODUCTION

Antimony-doped tin oxide (ATO) possesses special electrical and optical properties and has applications in transparent electrodes, energy storage devices, print displays and heating elements. ATO nanostructures have been fabricated by treating colloids of tin antimony oxide in an autoclave (Nutz et al. 2000). Thermal evaporation technique has recently been used to synthesize unique metal oxide nanostructures (Pan et al. 2001). We report here the synthesis and characterization of ATO nanostructures using a technique similar to that reported in reference (Pan et al. 2001).

EXPERIMENT

The experimental setup for synthesizing the ATO nanostructures consists of a tube furnace, a gas controlling system, alumina tubes and a vacuum pump (Pan et al.

2001). Commercially available ATO (10wt%Sb_2O_3-90wt%SnO_2) powders are used as the source material (in the high temperature zone (HTZ)). Alumina plates and two kinds of silicon wafers are used as substrates, one kind of silicon substrates are clean silicon wafers and the other one are coated with Au particles with sizes ranging from 2nm to 50nm (Figure 1). The furnace temperature ranges between 1000ºC and 1400ºC and various substrates (silicon plates and alumina plates) were used to collect the product (from middle temperature (MTZ 700ºC-800ºC) to low temperature zone (LTZ 300ºC-400ºC)). The form of the final products varies with experimental condition. The as-synthesized products were characterized using field emission scanning electron microscopy (JEOL 6320FX) and transmission electron microscopy (PHILPS EM 430ST).

RESULTS AND DISCUSSION

We use 1050ºC as the experiment temperature. Also we put the two types of silicon wafer substrates at 600-700ºC temperature zone. The silicon substrates were put in parallel along the downstream of gas flow. Proper adjustment of gas flow rate is critical to the formation of the final products on the silicon substrates. Very different products are formed on different silicon wafers and different temperature zones.

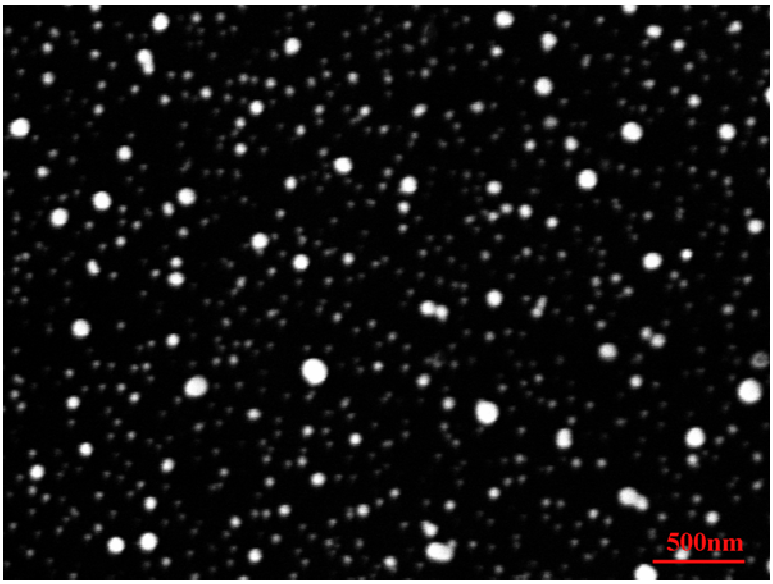

Figure A1 SEM image shows silicon substrate coated with gold nanoparticles.

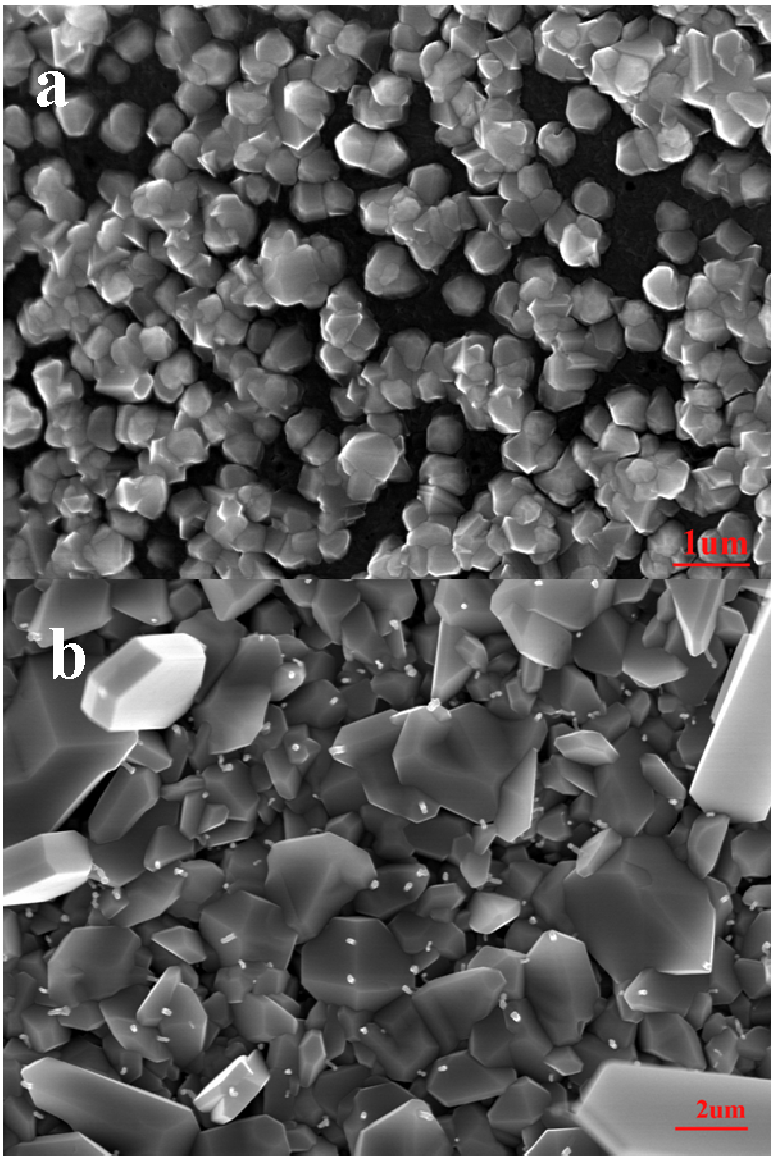

Figure A2. (a) ATO powders grow on the clean silicon substrate. **Figure A2. (b)** Shows growth of ATO powders on the Au/Si substrate, revealing the presence of large Au particles. The temperature of the silicon substrates was about 700ºC-800ºC.

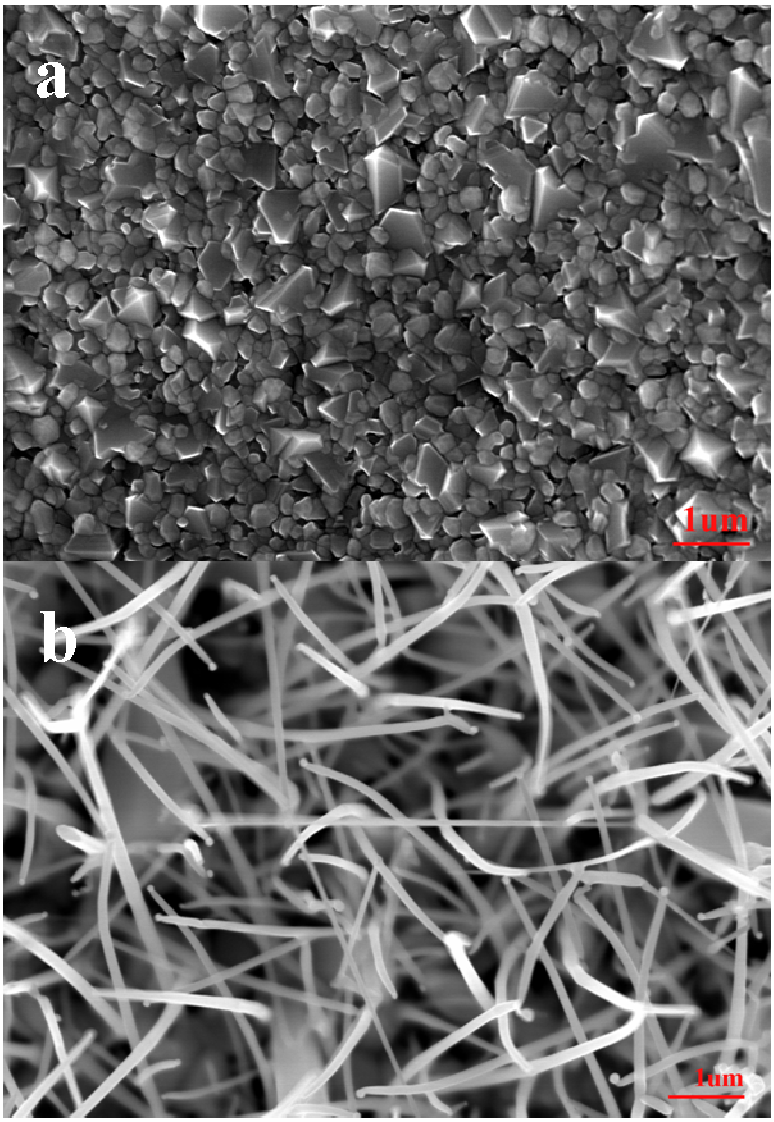

Figure A3. (a) ATO clusters on the clean silicon wafer at 600ºC -700ºC temperature zone. **Figure A3. (b)** Au-promoted growth of ATO nanowires at the same 600ºC -700ºC temperature zone.

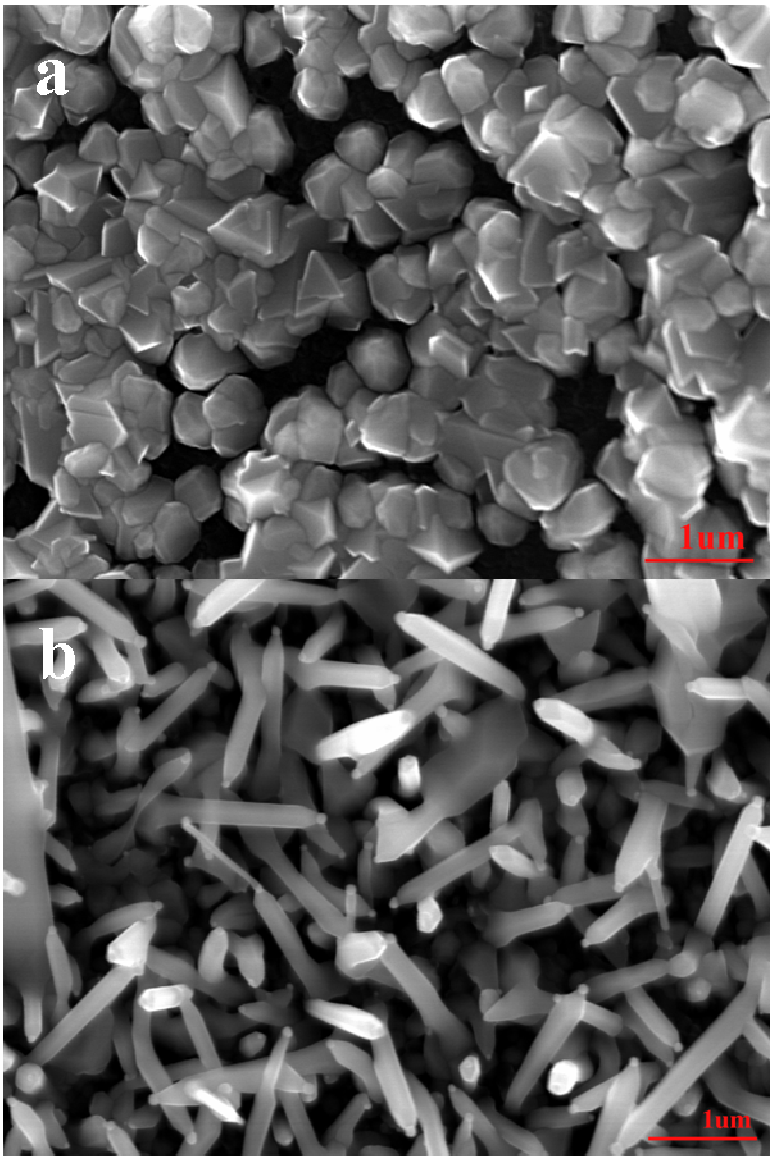

Figure A4. (a) ATO powders on the clean silicon wafer at 500ºC -600ºC temperature zone. **Figure A4. (b)** Au-promoted growth of ATO nanocones at the same 600ºC -700ºC temperature zone.

Different shapes of blocks form on the clean silicon surface at different temperature zones (Figure A2a, figure A3a and figure A4a). The sizes of these powders are about a few hundreds of nanometers. Small ATO clusters nucleate on the smooth Si surface first. Then these seeds absorb ATO atoms to form the lowest surface energy shapes of large powders.

On the Au/Si substrate, at the high temperature zone (700ºC-800ºC) Au nanoparticles sinter to form large particles as shown in figure A2b. It is not clear yet why the ATO powders were formed and the Au particles did not promote any controlled growth at this temperature zone.

In the lower temperature zone (600ºC -700ºC), however, the presence of Au nanoparticles promoted the growth of ATO nanowires/needles as shown in figure A3b. The Au particles are all at the top of the nanowires/needles.

At even lower temperatures (500ºC -600ºC), the Au nanoparticles promoted the growth of nanorods/nanocones (Figure A4b). The diameters of the nanorods/nanocones, however, are much larger than the sizes of the Au nanoparticles.

At 500ºC -600ºC temperature zone, the diameters of ATO nanowires are around 100nm. And the lengths of the nanowires are about 10-20um (Figure A6). Compare with 600ºC -700ºC (Figure A5) temperature zone product, these nanowires are shorter and bigger.

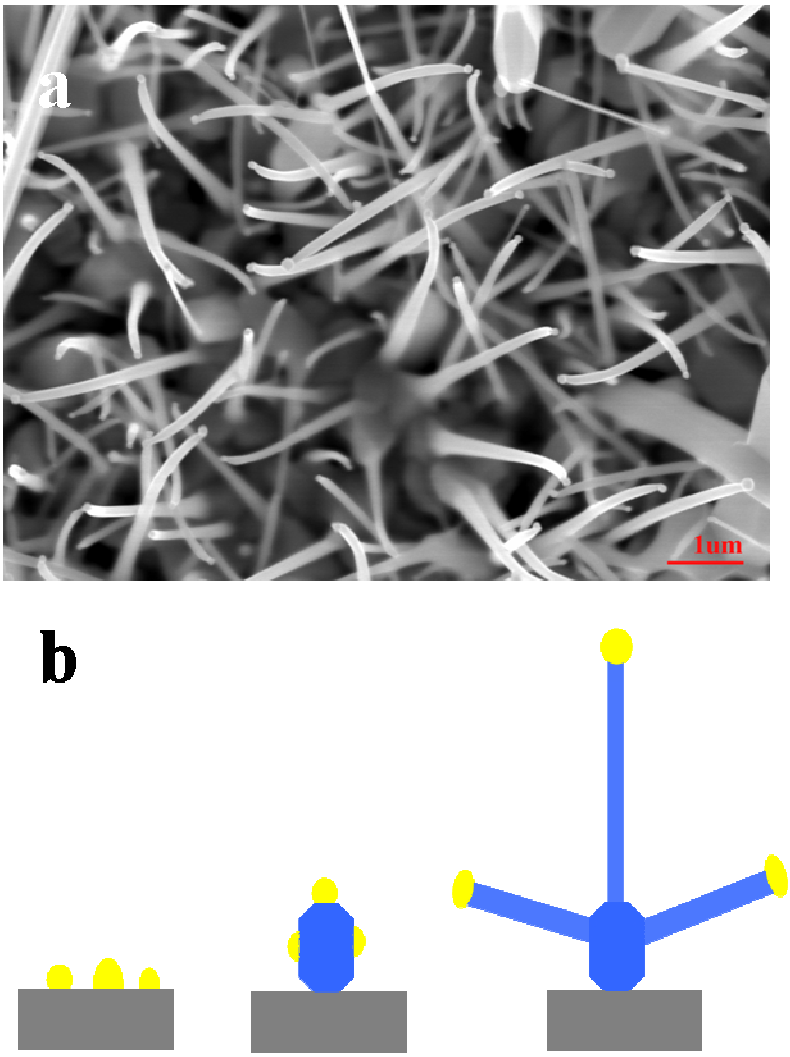

Figure A5 ATO nanowires formed on the gold coated silicon wafers at 600ºC -700ºC temperature zone.

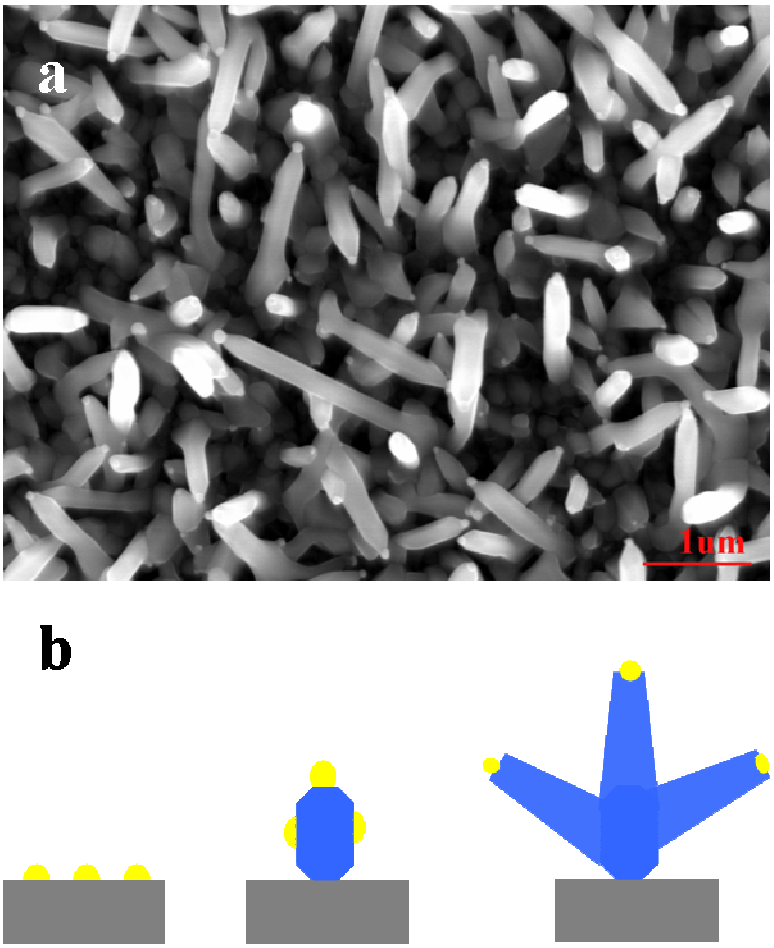

Figure A6 ATO nanocones formed at 500ºC -600ºC temperature zone.

TEM images also show the phenomena which we have observed in SEM (Figure A7). Gold particles are more clearly shown in TEM images.

HRTEM and electron diffraction pattern reveal that the nanowires are single crystalline (Figure A7). Electron diffraction and HRTEM lattice fringe analysis shows that the crystal structure of the nanowires is orthorhombic. And the growth direction of the nanowires is along [110] direction.

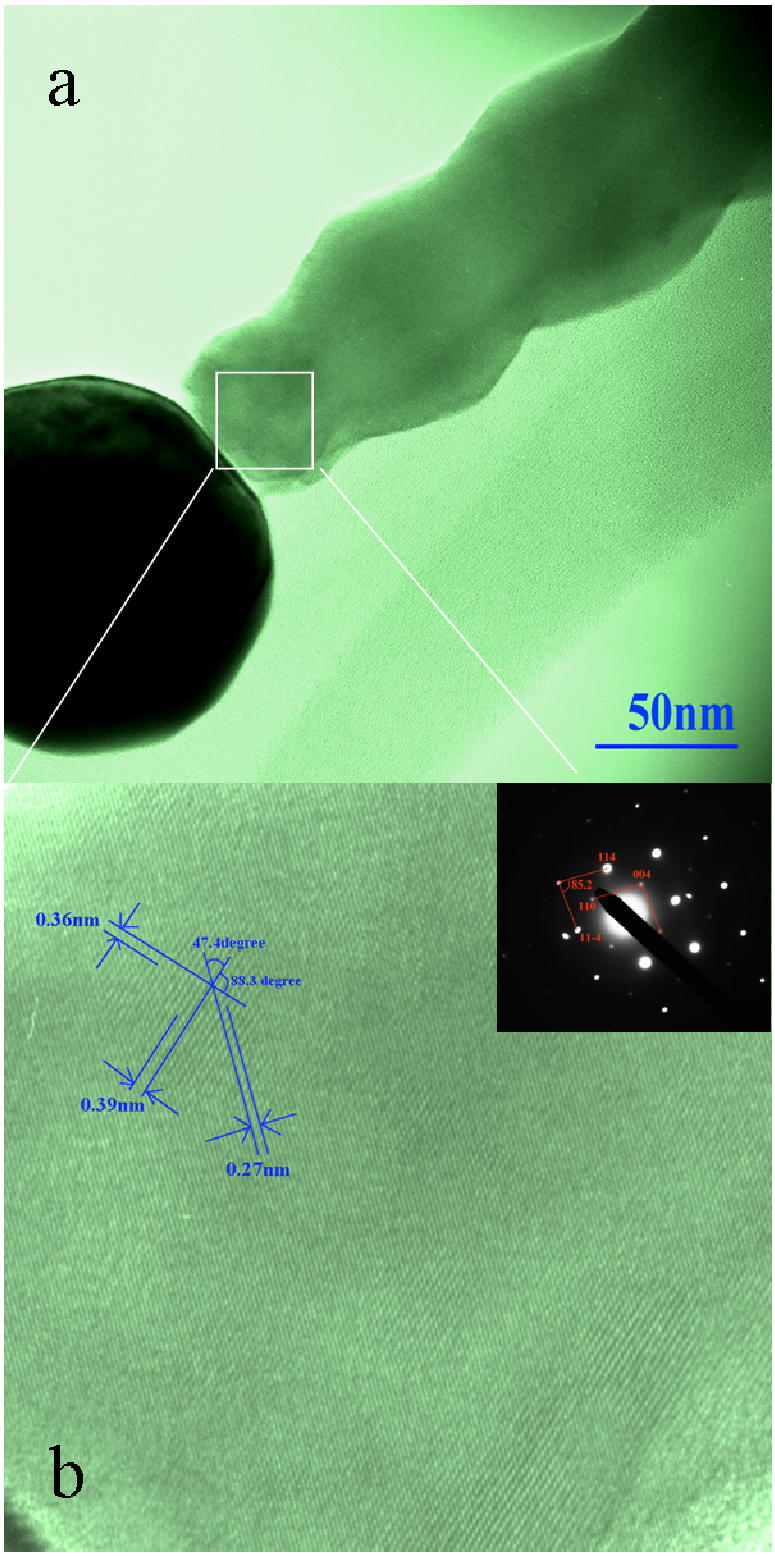

Figure A7 HRTEM image shows ATO nanowires lattice fringe. 0.27nm is tin oxide orthorhomic structure (114) spacing, 0.39nm is (004) spacing and 0.36nm is (110) spacing. The small inset is corresponding diffraction pattern of same location.

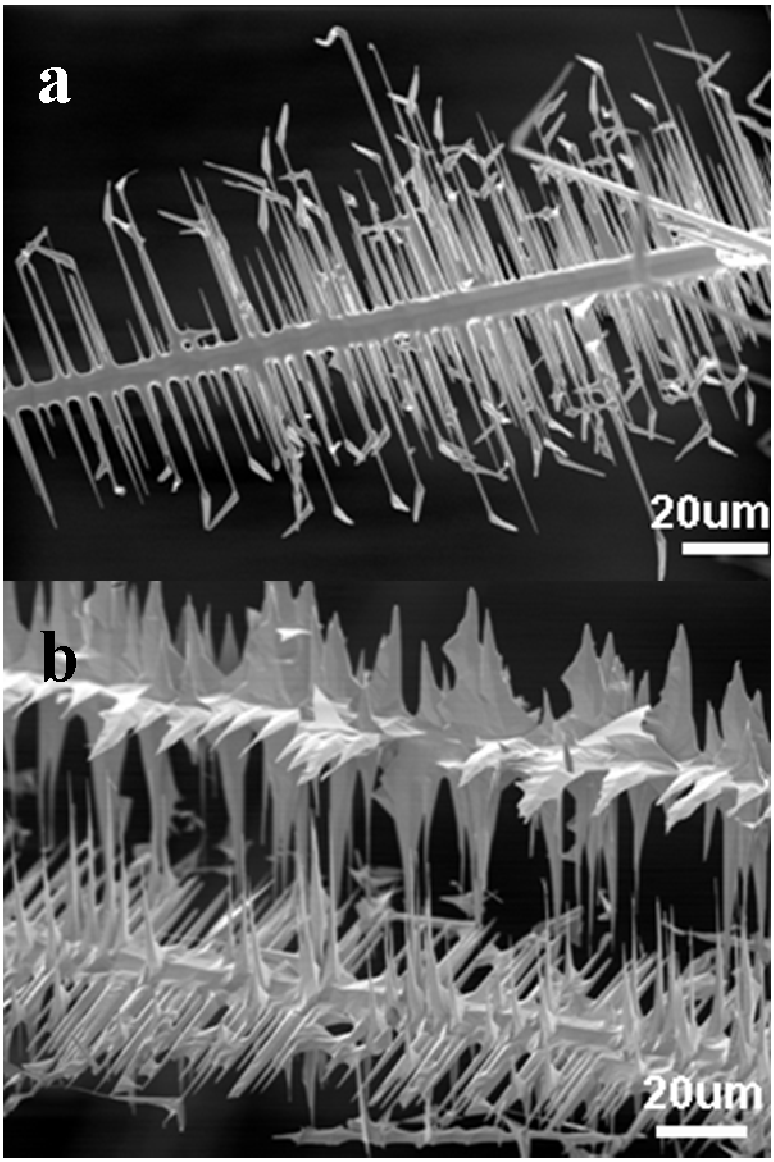

Figures A8a and A8b A representative SEM image of the fabricated ATO products. A unique tree-like structure was frequently observed. It is interesting to note that most of the tree branches have flag-like morphology at the tips of the branches. The dendritic (Figure A9) structures are artistically amusing, but the presence of these structures reduces the yield of the desired structures.

Figure A9. Unique hollow structures have also been observed. These tube structures seem to have a well-defined external shape (square prism).

We have also observed the growth of various types of morphologies of ATO: tree-like, dendrites, tubes of various shapes, etc. We are still working on understanding the growth processes of these different types of nanostructures and how to control the experimental conditions to optimize the yield of desired nanostructures.

A nanowire growth mechanism has been proposed by vapor liquid solid or vapor solid growth for many years (Wagner et al. 1964). Gold particles change to liquid state and absorb ATO atoms. ATO particles will deposit and crystallize on the silicon substrates. There are different model for the nanowires' growth (Dubrovskii et al. 2006). In our experiment, gold catalysts trigger the second step growth. ATO vapor may deposit on the clean silicon surface to form the lowest surface energy shape. Gold particles trigger the growth of the nanowires and nanocones.

CONCLUSIONS

Different ATO nanostructures have been fabricated and characterized. HRTEM and SAD analysis indicate that the nanowires are orthorhombic structure. The formation of nanowires can be interpreted by VLS growth mechanism. Our results show that the Au nanoparticles promote the growth of ATO nanowires or nanorods/nanocones.

BIBLIOGRAPHY

Andreazza-Vignolle, C., P. Andreazza, et al. (2006). "Catalyst effect on ZnO nanostructure shape". ***Superlattices and Microstructures*** **39**(1-4): 340-347.

Arnold, M. S., P. Avouris, et al. (2003). "Field-effect transistors based on single semiconducting oxide nanobelts". ***Journal of Physical Chemistry B*** **107**(3): 659-663.

Bagnall, D. M., Y. F. Chen, et al. (1997). "Optically pumped lasing of ZnO at room temperature". ***Applied Physics Letters*** **70**(17): 2230-2232.

Balaur, E., T. Djenizian, et al. (2004). "Electron beam-induced modification of organic monolayers on Si(111) surfaces used for selective electrodeposition". ***Electrochemistry Communications*** **6**(2): 153-157.

Banerjee, D., J. Y. Lao, et al. (2004). "Synthesis and photoluminescence studies on ZnO nanowires". ***Nanotechnology*** **15**(3): 404-409.

Bethune, D. S., C. H. Kiang, et al. (1993). "Cobalt-Catalyzed Growth of Carbon Nanotubes with Single-Atomic-Layerwalls". ***Nature*** **363**(6430): 605-607.

Bu, W. B., Z. L. Hua, et al. (2004). "Surfactant-assisted synthesis of lanthanide phosphates single-crystalline nanowires/nanorods". ***Journal of Materials Research*** **19**(10): 2807-2811.

Burki, J. (2007). "Discrete thinning dynamics in a continuum model of metallic nanowires". ***Physical Review B*** **75**(20): 205435-1-20543-9.

Burton, W. K., N. CABRERA, et al. (1949). "Role of Dislocations in Crystal Growth". ***Nature*** **163**: 398-399.

Burton, W. K., N. CABRERA, et al. (1951). "The growth of crystals and the equilibrium structures of their surfaces". ***Philos. Trans. R. Soc. London, Ser. A*** **243**: 299-358.

Cantalini, C., L. Valentini, et al. (2003). "Sensitivity to NO2 and cross-sensitivity analysis to NH3, ethanol and humidity of carbon nanotubes thin film prepared by PECVD". ***Sensors and Actuators B-Chemical*** **95**(1-3): 195-202.

Cao, G. (2004). "Nanostructures & Nanomaterials: Synthesis, Properties & Applications", Imperial College Press.

Cao, H., J. Y. Xu, et al. (2000). "Spatial confinement of laser light in active random media". ***Physical Review Letters*** **84**(24): 5584-5587.

Cao, L. M., K. Hahn, et al. (2002). "Template-catalyst-free growth of highly ordered boron nanowire arrays". ***Applied Physics Letters*** **80**(22): 4226-4228.

Cao, L. M., Z. Zhang, et al. (2001). "Well-aligned boron nanowire arrays". ***Advanced Materials*** **13**(22): 1701-1704.

Cao, L. Y., D. N. Barsic, et al. (2007). "Plasmon-assisted local temperature control to pattern individual semiconductor nanowires and carbon nanotubes". ***Nano Letters*** **7**(11): 3523-3527.

Chen, B. J., X. W. Sun, et al. (2004). "Fabrication of zinc oxide nanostructures on gold-coated silicon substrate by thermal chemical reactions vapor transport deposition in air". ***Ceramics International*** **30**(7): 1725-1729.

Chen, Z., N. Wu, et al. (2005). "Effect of N2 flow rate on morphology and structure of ZnO nanocrystals synthesized via vapor deposition". ***Scripta Materialia*** **52**(1): 63-67.

Chen, Z. H., J. Appenzeller, et al. (2006). "An integrated logic circuit assembled on a single carbon nanotube". ***Science*** **311**(5768): 1735-1735.

Cheng, B., J. M. Russell, et al. (2004). "Large-scale, solution-phase growth of single-crystalline SnO2 nanorods". ***Journal of the American Chemical Society*** **126**(19): 5972-5973.

Chien, C. C. and K. T. Jeng (2006). "Effective preparation of carbon nanotube-supported Pt-Ru electrocatalysts". ***Materials Chemistry and Physics*** **99**(1): 80-87.

Choy, J. H., E. S. Jang, et al. (2003). "Soft solution route to directionally grown ZnO nanorod arrays on Si wafer; room-temperature ultraviolet laser". ***Advanced Materials*** **15**(22): 1911-1914.

Comini, E., G. Faglia, et al. (2002). "Stable and highly sensitive gas sensors based on semiconducting oxide nanobelts". ***Applied Physics Letters*** **81**(10): 1869-1871.

Correia, A., M. Perez, et al. (2007). "Nanoscience and nanotechnology - driving research and applications". ***Physica Status Solidi-Rapid Research Letters*** **1**(4): A68-A72.

Couvreur, P. and C. Vauthier (2006). "Nanotechnology: Intelligent design to treat complex disease". ***Pharmaceutical Research*** **23**(7): 1417-1450.

Cui, Y., X. F. Duan, et al. (2000). "Doping and electrical transport in silicon nanowires". ***Journal of Physical Chemistry B*** **104**(22): 5213-5216.

Cui, Y. and C. M. Lieber (2001a). "Functional nanoscale electronic devices assembled using silicon nanowire building blocks". ***Science*** **291**(5505): 851-853.

Cui, Y., Q. Q. Wei, et al. (2001b). "Nanowire nanosensors for highly sensitive and selective detection of biological and chemical species". ***Science*** **293**(5533): 1289-1292.

Cui, Y., Z. H. Zhong, et al. (2003). "High performance silicon nanowire field effect transistors". ***Nano Letters*** **3**(2): 149-152.

Dai, Z. R., Z. W. Pan, et al. (2003). "Novel nanostructures of functional oxides synthesized by thermal evaporation". ***Advanced Functional Materials*** **13**(1): 9-24.

Deng, D. and J. Y. Lee (2008). "Hollow core-shell mesospheres of crystalline SnO2 nanoparticle aggregates for high capacity Li+ ion storage". ***Chemistry of Materials*** **20**(5): 1841-1846.

Dick, K. A., K. Deppert, et al. (2005). "A new understanding of au-assisted growth of III-V semiconductor nanowires". ***Advanced Functional Materials*** **15**(10): 1603-1610.

Dick, K. A., S. Kodambaka, et al. (2007). "The morphology of axial and branched nanowire heterostructures". ***Nano Letters*** **7**(6): 1817-1822.

Dijkkamp, D., T. Venkatesan, et al. (1987). "Preparation of Y-Ba-Cu oxide superconductor thin films using pulsed laser evaporation from high Tc bulk material". ***Applied Physics Letters*** **51**: 619-621.

Dresselhaus, M. S., G. Dresselhaus, et al. (1996). "Science of Fullerenes and Carbon Nanotubes: Their Properties and Applications", Academic Press.

Duan, X. F., Y. Huang, et al. (2003). "Single-nanowire electrically driven lasers". ***Nature*** **421**(6920): 241-245.

Duan, X. F., Y. Huang, et al. (2001). "Indium phosphide nanowires as building blocks for nanoscale electronic and optoelectronic devices". ***Nature*** **409**(6816): 66-69.

Duan, X. F. and C. M. Lieber (2000). "General synthesis of compound semiconductor nanowires". ***Advanced Materials*** **12**(4): 298-302.

Dubrovskii, V. G., N. V. Sibirev, et al. (2006). "Theoretical analysis of the vapor-liquid-solid mechanism of nanowire growth during molecular beam epitaxy". ***Physical Review E*** **73**(2): 021603-1-021603-10.

Ebbesen, M. and T. G. Jensen (2006). "Nanomedicine: Techniques, Potentials, and Ethical Implications". ***Journal of Biomedicine and Biotechnology*** **2006**(51516): 1-11.

Edington, J. W. (1976). "Practical electron microscopy in materials science", Van Nostrand Reinhold Co.

Fan, H. J., B. Fuhrmann, et al. (2006). "Well-ordered ZnO nanowire arrays on GaN substrate fabricated via nanosphere lithography". ***Journal of Crystal Growth*** **287**(1): 34-38.

Fan, X., X. M. Meng, et al. (2007). "Template fabrication of SiO2 nanotubes". ***Applied Physics Letters*** **90**(10): 103114-1-103114-3.

Faraday, M. (1857). "Experimental relations of gold (and other metals) to light". ***Philosophical trasactions*** **147**: 145-181.

Fraundorf, P. (2008). "Digital darkfield decompositions". ***arXiv: cond-mat/0403017v1 [cond-mat.mtrl-sci]***.

Fraundorf, P., W. T. Qin, et al. (2005). "Making sense of nanocrystal lattice fringes". ***Journal of Applied Physics*** **98**(11): 114308-1-114308-10.

Gao, P. X., Y. Ding, et al. (2003a). "Crystallographic orientation-aligned ZnO nanorods grown by a tin catalyst". ***Nano Letters*** **3**(9): 1315-1320.

Gao, P. X. and Z. L. Wang (2003b). "Mesoporous polyhedral cages and shells formed by textured self-assembly of ZnO nanocrystals". ***Journal of the American Chemical Society*** **125**(37): 11299-11305.

Gasparac, R., P. Kohli, et al. (2004). "Template synthesis of nano test tubes". ***Nano Letters*** **4**(3): 513-516.

Geng, C. Y., Y. Jiang, et al. (2004). "Well-aligned ZnO nanowire arrays fabricated on silicon substrates". ***Advanced Functional Materials*** **14**(6): 589-594.

Govender, K., D. S. Boyle, et al. (2002). "Room-temperature lasing observed from ZnO nanocolumns grown by aqueous solution deposition". ***Advanced Materials*** **14**(17): 1221-1224.

Gu, Z. H. and P. B. Balbuena (2005). "Structural characterization of Pt nanoclusters deposited on graphite: Effects of substrate and surrounding medium". ***Catalysis Today*** **105**(1): 152-161.

Guan, Y. F. and A. J. Pedraza (2008). "Synthesis and alignment of Zn and ZnO nanoparticles by laser-assisted chemical vapor deposition". ***Nanotechnology*** **19**(4): 045609-1-045609-7.

Guo, S. J., S. J. Dong, et al. (2008). "Gold/platinum hybrid nanoparticles supported on multiwalled carbon nanotube/silica coaxial nanocables: Preparation and application as electrocatalysts for oxygen reduction". ***Journal of Physical Chemistry C*** **112**(7): 2389-2393.

Guo, T., P. Nikolaev, et al. (1995a). "Self-Assembly of Tubular Fullerenes". ***Journal of Physical Chemistry*** **99**(27): 10694-10697.

Guo, T., P. Nikolaev, et al. (1995b). "Catalytic Growth of Single-Walled Nanotubes by Laser Vaporization". ***Chemical Physics Letters*** **243**(1-2): 49-54.

Hamada, N., S. Sawada, et al. (1992). "New One-Dimensional Conductors - Graphitic Microtubules". ***Physical Review Letters*** **68**(10): 1579-1581.

Han, L., W. Wu, et al. (2004a). "A direct route toward assembly of nanoparticle-carbon nanotube composite materials". ***Langmuir*** **20**(14): 6019-6025.

Han, S., C. Li, et al. (2004b). "Transition metal oxide core-shell nanowires: Generic synthesis and transport studies". ***Nano Letters*** **4**(7): 1241-1246.

Hara, K., T. Horiguchi, et al. (2000). "Highly efficient photon-to-electron conversion with mercurochrome-sensitized nanoporous oxide semiconductor solar cells". ***Solar Energy Materials and Solar Cells*** **64**(2): 115-134.

Herring, C. (1951). "Some theorems on the free energies of crystal surfaces". ***Physical Review*** **82**(1): 87-93.

Hiruma, K., M. Yazawa, et al. (1995). "Growth and Optical-Properties of Nanometer-Scale Gaas and Inas Whiskers". ***Journal of Applied Physics*** **77**(2): 447-462.

Huang, M. H., S. Mao, et al. (2001a). "Room-temperature ultraviolet nanowire nanolasers". ***Science*** **292**(5523): 1897-1899.

Huang, M. H., Y. Y. Wu, et al. (2001b). "Catalytic growth of zinc oxide nanowires by vapor transport". ***Advanced Materials*** **13**(2): 113-116.

Hughes, W. L. and Z. L. Wang (2005). "Controlled synthesis and manipulation of ZnO nanorings and nanobows". ***Applied Physics Letters*** **86**(4): 043106-1-043106-3.

Humbert, A., M. Dayez, et al. (1991). "Ultrahigh-Vacuum and Air Observations of Pd Clusters Grown on Clean Graphite". ***Journal of Vacuum Science & Technology B*** **9**(2): 804-805.

Iijima, S. (1991). "Helical Microtubules of Graphitic Carbon". ***Nature*** **354**(6348): 56-58.

Iijima, S. and T. Ichihashi (1993). "Single-Shell Carbon Nanotubes of 1-Nm Diameter". ***Nature*** **363**(6430): 603-605.

Iwasa, N., S. Masuda, et al. (1995). "Steam Reforming of Methanol over Pd/Zno - Effect of the Formation of Pdzn Alloys Upon the Reaction". ***Applied Catalysis a-General*** **125**(1): 145-157.

Jie, J. S., G. Z. Wang, et al. (2005). "Synthesis and optical properties of well-aligned ZnO nanorod array on an undoped ZnO film". ***Applied Physics Letters*** **86**(3): 031909-1-031909-3.

Jin, Z. C., I. Hamberg, et al. (1988). "Optical properties of sputter-deposited ZnO:Al thin films". ***J. Appl. Phys*** **64**: 5117.

Joseyacaman, M., M. Mikiyoshida, et al. (1993). "Catalytic Growth of Carbon Microtubules with Fullerene Structure (Applied Physics Letter, Vol 62, Pg 202, 1993)". ***Applied Physics Letters*** **62**(6): 657-659.

Kar, S. and S. Chaudhuri (2005). "Controlled synthesis and photoluminescence properties of ZnS nanowires and nanoribbons". ***Journal of Physical Chemistry B*** **109**(8): 3298-3302.

Karabacak, T., A. Mallikarjunan, et al. (2003). "beta-phase tungsten nanorod formation by oblique-angle sputter deposition". ***Applied Physics Letters*** **83**(15): 3096-3098.

Kast, M., P. Schroeder, et al. (2007). "Synthesis of single-crystalline Zn metal nanowires utilizing cold-wall physical vapor deposition". ***Nano Letters*** **7**(8): 2540-2544.

Keis, K., L. Vayssieres, et al. (1999). "Nanostructured ZnO electrodes for photovoltaic applications". ***Nanostructured Materials*** **12**(1-4): 487-490.

Khan, A., W. M. Jadwisienczak, et al. (2007). "Catalyst-free synthesis and luminescence of aligned ZnO nanorods". ***Physica E-Low-Dimensional Systems & Nanostructures*** **39**(2): 258-261.

Kim, B. M., S. Qian, et al. (2005). "Filling carbon nanotubes with particles". ***Nano Letters*** **5**(5): 873-878.

Kim, T. Y., J. Y. Kim, et al. (2004). "Characterization of ZnO needle-shaped nanostructures grown on NiO catalyst-coated Si substrates". ***Synthetic Metals*** **144**(1): 61-68.

Kind, H., H. Q. Yan, et al. (2002). "Nanowire ultraviolet photodetectors and optical switches". ***Advanced Materials*** **14**(2): 158-160.

Kirkham, M., X. D. Wang, et al. (2007). "Solid Au nanoparticles as a catalyst for growing aligned ZnO nanowires: a new understanding of the vapour-liquid-solid process". ***Nanotechnology*** **18**(36): 365304-1-365304-5.

Konenkamp, R., R. C. Word, et al. (2004). "Vertical nanowire light-emitting diode". ***Applied Physics Letters*** **85**(24): 6004-6006.

Kong, B. H., D. C. Kim, et al. (2006). "Shape control and characterization of one-dimensional ZnO nanostructures through the synthesis procedure". ***Physica B-Condensed Matter*** **376**: 726-730.

Kong, J., M. G. Chapline, et al. (2001). "Functionalized carbon nanotubes for molecular hydrogen sensors". ***Advanced Materials*** **13**(18): 1384-1386.

Kong, J., N. R. Franklin, et al. (2000). "Nanotube molecular wires as chemical sensors". ***Science*** **287**(5453): 622-625.

Kong, X. Y., Y. Ding, et al. (2004a). "Single-crystal nanorings formed by epitaxial self-coiling of polar nanobelts". ***Science*** **303**(5662): 1348-1351.

Kong, X. Y. and Z. L. Wang (2004b). "Polar-surface dominated ZnO nanobelts and the electrostatic energy induced nanohelixes, nanosprings, and nanospirals". ***Applied Physics Letters*** **84**(6): 975-977.

Kovtyukhova, N. I., T. E. Mallouk, et al. (2003). "Templated surface sol-gel synthesis of SiO2 nanotubes and SiO2-insulated metal nanowires". ***Advanced Materials*** **15**(10): 780-785.

Kuoni, A., R. Holzherr, et al. (2003). "Polyimide membrane with ZnO piezoelectric thin film pressure transducers as a differential pressure liquid flow sensor". ***Journal of Micromechanics and Microengineering*** **13**(4): S103-S107.

Lai, Y. K., C. J. Lin, et al. (2008). "Superhydrophilic-superhydrophobic micropattern on TiO2 nanotube films by photocatalytic lithography". ***Electrochemistry Communications*** **10**(3): 387-391.

Lao, C., P. Gao, et al. (2005). "Formation of double-side teethed nanocombs of ZnO and self-catalysis of Zn-terminated polar surface". ***Chemical Physics Letters*** **417**: 359-363.

Lauhon, L. J., M. S. Gudiksen, et al. (2002). "Epitaxial core-shell and core-multishell nanowire heterostructures". ***Nature*** **420**(6911): 57-61.

Law, M., L. E. Greene, et al. (2005). "Nanowire dye-sensitized solar cells". ***Nature Materials*** **4**(6): 455-459.

Lee, C. J., T. J. Lee, et al. (2002). "Field emission from well-aligned zinc oxide nanowires grown at low temperature". ***Applied Physics Letters*** **81**(19): 3648-3650.

Lee, J. P. and M. M. Sung (2004). "A new Patterning method using photocatalytic lithography and selective atomic layer deposition". ***Journal of the American Chemical Society*** **126**(1): 28-29.

Lee, P. S., O. J. Lee, et al. (2005). "Vertically aligned nanopillar arrays with hard skins using anodic aluminum oxide for nano imprint lithography". ***Chemistry of Materials*** **17**(24): 6181-6185.

Li, C., G. J. Fang, et al. (2006). "Effect of substrate temperature on the growth and photoluminescence properties of vertically aligned ZnO nanostructures". ***Journal of Crystal Growth*** **292**(1): 19-25.

Li, J., Y. J. Lu, et al. (2003a). "Carbon nanotube sensors for gas and organic vapor detection". ***Nano Letters*** **3**(7): 929-933.

Li, Q. and C. Wang (2003b). "Fabrication of wurtzite ZnS nanobelts via simple thermal evaporation". ***Appl. Phys. Lett.*** **83**: 359-361.

Li, S. Y., P. Lin, et al. (2004). "Field emission and photofluorescent characteristics of zinc oxide nanowires synthesized by a metal catalyzed vapor-liquid-solid process". ***Journal of Applied Physics*** **95**(7): 3711-3716.

Li, W. Z., C. H. Liang, et al. (2003c). "Preparation and characterization of multiwalled carbon nanotube-supported platinum for cathode catalysts of direct methanol fuel cells". ***Journal of Physical Chemistry B*** **107**(26): 6292-6299.

Lin, C. C., P. L. Chen, et al. (2005a). "Selective growth of horizontally-oriented carbon nanotube bridges on patterned silicon wafers by electroless plating Ni catalysts". ***Diamond and Related Materials*** **14**(11-12): 1867-1871.

Lin, Y. H., X. L. Cui, et al. (2005b). "Platinum/carbon nanotube nanocomposite synthesized in supercritical fluid as electrocatalysts for low-temperature fuel cells". ***Journal of Physical Chemistry B*** **109**(30): 14410-14415.

Lin, Z. S. and P. D. Bristowe (2007). "Microscopic characteristics of the Ag(111)/ZnO(0001) interface present in optical coatings". ***Physical Review B*** **75**(20): 205423-1-205423-13.

Liu, C. H., J. A. Zapien, et al. (2003a). "High-density, ordered ultraviolet light-emitting ZnO nanowire arrays". ***Advanced Materials*** **15**(10): 838-841.

Liu, H. S., K. Ishida, et al. (2003b). "Thermodynamic assessment of the Au-Zn binary system". ***Intermetallics*** **11**(10): 987-994.

Liu, Z. L., X. Y. Ling, et al. (2004). "Carbon-supported Pt and PtRu nanoparticles as catalysts for a direct methanol fuel cell". ***Journal of Physical Chemistry B*** **108**(24): 8234-8240.

Mahmud, S., M. J. Abdullah, et al. (2006). "Growth model for nanomallets of zinc oxide from a catalyst-free combust-oxidised process". ***Journal of Crystal Growth*** **287**(1): 118-123.

Marsen, B. and K. Sattler (1999). "Fullerene-structured nanowires of silicon". ***Physical Review B*** **60**(16): 11593-11600.

Massalski, T. B. (1986). "Binary Alloy Phase Diagrams". Metals Park, Ohio, ASM International.

McIlroy, D. N., A. Alkhateeb, et al. (2004). "Nanospring formation - unexpected catalyst mediated growth". ***Journal of Physics-Condensed Matter*** **16**(12): R415-R440.

Meyer, B. and D. Marx (2004). "Density-functional study of Cu atoms, monolayers, films, and coadsorbates on polar ZnO surfaces". ***Physical Review B*** **69**(23): 235420-1-235420-7.

Meyer, E., H. J. Hug, et al. (2003). "Scanning Probe Microscopy: The Lab on a Tip", Springer.

Mitchell, D. T., S. B. Lee, et al. (2002). "Smart nanotubes for bioseparations and biocatalysis". ***Journal of the American Chemical Society*** **124**(40): 11864-11865.

Mitzner, K. D., J. Sternhagen, et al. (2003). "Development of a micromachined hazardous gas sensor array". ***Sensors and Actuators B-Chemical*** **93**(1-3): 92-99.

Morales, A. M. and C. M. Lieber (1998). "A laser ablation method for the synthesis of crystalline semiconductor nanowires". ***Science*** **279**(5348): 208-211.

Murakami, K., M. Saito, et al. (2003). "ARHVTEM of the Pd/ZnO heterointerface chemical structure". ***Journal of Electron Microscopy*** **52**(1): 27-32.

Nakayama, T., T. A. Yamamoto, et al. (2000). "Structure and magnetic properties of iron oxide dispersed silver based nanocluster composite". ***Journal of Materials Science*** **35**(15): 3857-3861.

Nutz, T. and M. Haase (2000). "Wet-chemical synthesis of doped nanoparticles: Optical properties of oxygen-deficient and antimony-doped colloidal SnO2". ***Journal of Physical Chemistry B*** **104**(35): 8430-8437.

O'Keefe, M. A., L. F. Allard, et al. (2005). "HRTEM imaging of atoms at sub-angstrom ngstrom resolution". ***Journal of Electron Microscopy*** **54**(3): 169-180.

Odom, T. W., J. L. Huang, et al. (1998). "Atomic structure and electronic properties of single-walled carbon nanotubes". ***Nature*** **391**(6662): 62-64.

Ogawa, H., M. Nishikawa, et al. (1982). "Hall measurement studies and an electrical conduction model of tin oxide ultrafine particle films". ***J. Appl. Phys.*** **53**: 4448-4455.

Pan, Z. W., Z. R. Dai, et al. (2001). "Nanobelts of semiconducting oxides". ***Science*** **291**(5510): 1947-1949.

Park, W. I. and G. C. Yi (2004). "Electroluminescence in n-ZnO nanorod arrays vertically grown on p-GaN". ***Advanced Materials*** **16**(1): 87-90.

Park, W. I., G. C. Yi, et al. (2003). "Schottky nanocontacts on ZnO nanorod arrays". ***Applied Physics Letters*** **82**(24): 4358-4360.

Pengfei, Q. F., O. Vermesh, et al. (2003). "Toward large arrays of multiplex functionalized carbon nanotube sensors for highly sensitive and selective molecular detection". ***Nano Letters*** **3**(3): 347-351.

Persson, A. I., M. W. Larsson, et al. (2004). "Solid-phase diffusion mechanism for GaAs nanowire growth". ***Nature Materials*** **3**(10): 677-681.

Pettersson, H., J. Tragardh, et al. (2006). "Infrared photodetectors in heterostructure nanowires". ***Nano Letters*** **6**(2): 229-232.

Prabhuram, J., X. Wang, et al. (2003). "Synthesis and characterization of surfactant-stabilized PVC nanocatalysts for fuel cell applications". ***Journal of Physical Chemistry B*** **107**(40): 11057-11064.

Qin, W. and P. Fraundorf (2003). "Lattice parameters from direct-space images at two tilts". ***Ultramicroscopy*** **94**(3-4): 245-262.

Qin, Y., X. D. Wang, et al. (2008). "Microfibre-nanowire hybrid structure for energy scavenging". ***Nature*** **451**(7180): 809-813.

Qu, L. T., L. M. Dai, et al. (2006). "Shape/size-control led syntheses of metal nanoparticles for site-selective modification of carbon nanotubes". ***Journal of the American Chemical Society*** **128**(16): 5523-5532.

Remita, H., P. F. Siril, et al. (2006). "Activity evaluation of carbon paste electrodes loaded with pt nanoparticles prepared in different radiolytic conditions". ***Journal of Solid State Electrochemistry*** **10**(7): 506-511.

Roco, M. C. (2003). "Broader societal issues of nanotechnology". ***Journal of Nanoparticle Research*** **5**(3-4): 181-189.

Rosei, F. (2004). "Nanostructured surfaces: challenges and frontiers in nanotechnology". ***Journal of Physics-Condensed Matter*** **16**(17): S1373-S1436.

Saito, R., M. Fujita, et al. (1992). "Electronic-Structure of Chiral Graphene Tubules". ***Applied Physics Letters*** **60**(18): 2204-2206.

Sears, G. W. (1955). "Influence of adsorbed films on crystal growth kinetics". ***Journal of Chemical Physics*** **25**(1): 154-159.

Service, R. E. (1997). "Materials science - Will UV lasers beat the blues?" ***Science*** **276**(5314): 895-895.

Shibata, T., K. Unno, et al. (2002). "Characterization of sputtered ZnO thin film as sensor and actuator for diamond AFM probe". ***Sensors and Actuators a-Physical*** **102**(1-2): 106-113.

Shimizu, Y., T. Hyodo, et al. (2004). "Mesoporous semiconducting oxides for gas sensor application". ***Journal of the European Ceramic Society*** **24**(6): 1389-1398.

Singh, J. and D. E. Wolfe (2005). "Nano and macro-structured component fabrication by electron beam-physical vapor deposition (EB-PVD)". ***Journal of Materials Science*** **40**(1): 1-26.

Snow, E. S., F. K. Perkins, et al. (2005). "Chemical detection with a single-walled carbon nanotube capacitor". ***Science*** **307**(5717): 1942-1945.

Sreenivas, K., S. Kumar, et al. (2005). "Growth of zinc oxide nanostructures". ***Pramana-Journal of Physics*** **65**(5): 809-814.

Steinhart, M., L. L. Zhao, et al. (2004). "Compound semiconductor 1D nanostructures by template wetting." ***Abstracts of Papers of the American Chemical Society*** **227**: U1451-U1451.

Suenaga, K., M. P. Johansson, et al. (1999). "Carbon nitride nanotubulite - densely-packed and well-aligned tubular nanostructures". ***Chemical Physics Letters*** **300**(5-6): 695-700.

Sun, Y., G. M. Fuge, et al. (2006). "Growth mechanisms for ZnO nanorods formed by pulsed laser deposition". ***Superlattices and Microstructures*** **39**(1-4): 33-40.

Takai, K. and T. Enoki (2007). "Fabrication of graphitic nanowire structure by electron beam lithography". ***Physica E-Low-Dimensional Systems & Nanostructures*** **40**(2): 321-323.

Tang, Y. B., H. T. Cong, et al. (2005). "Synthesis of rectangular cross-section AlN nanofibers by chemical vapor deposition". ***Chemical Physics Letters*** **416**(1-3): 171-175.

Taniguchi, N. (1974). On the Basic Concept of Nanotechnology. Proc. Int. Conf. Prod. Eng. Tokyo, Part 2, Tokyo.

Tans, S. J., A. R. M. Verschueren, et al. (1998). "Room-temperature transistor based on a single carbon nanotube". ***Nature*** **393**(6680): 49-52.

Tatsuyama, C. and S. Ichimura (1976). "Electrical and Optical Properties of GaSe-SnO2 Heterojunctions". ***Jpn. J. Appl. Phys*** **15**: 843-847.

Thelander, C., H. A. Nilsson, et al. (2005). "Nanowire single-electron memory". ***Nano Letters*** **5**(4): 635-638.

Tjong, S. C. and H. Chen (2004). "Nanocrystalline materials and coatings". ***Materials Science & Engineering R-Reports*** **45**(1-2): 1-88.

Tseng, Y. K., H. C. Hsu, et al. (2003a). "Two-step oxygen injection process for growing ZnO nanorods". ***Journal of Materials Research*** **18**(12): 2837-2844.

Tseng, Y. K., C. J. Huang, et al. (2003b). "Characterization and field-emission properties of needle-like zinc oxide nanowires grown vertically on conductive zinc oxide films". ***Advanced Functional Materials*** **13**(10): 811-814.

Umar, A., S. H. Kim, et al. (2007). "Effect of hydrogen pretreatment combined with growth temperature on the morphologies of ZnO nanostructures: Structural and optical properties". ***Journal of Crystal Growth*** **306**(1): 52-61.

Urban, J. J., W. S. Yun, et al. (2002). "Synthesis of single-crystalline perovskite nanorods composed of barium titanate and strontium titanate". ***Journal of the American Chemical Society*** **124**(7): 1186-1187.

Vinodgopal, K., M. Haria, et al. (2004). "Fullerene-based carbon nanostructures for methanol oxidation". ***Nano Letters*** **4**(3): 415-418.

Vlasenko, L. S. and G. D. Watkins (2005). "Optical detection of electron paramagnetic resonance in room-temperature electron-irradiated ZnO". ***Physical Review B*** **71**(12): 125210-1-125210-6.

Wagner, R. S. and W. C. Ellis (1964). "Vapor-liquid-solid mechanism of single crystal growth". ***Applied Physics Letters*** **4**(5): 89-90.

Wan, Q., Q. H. Li, et al. (2004). "Fabrication and ethanol sensing characteristics of ZnO nanowire gas sensors". ***Applied Physics Letters*** **84**(18): 3654-3656.

Wang, M., C. H. Ye, et al. (2006a). "Synthesis of well-aligned ZnO nanorod arrays with high optical property via a low-temperature solution method". ***Journal of Crystal Growth*** **291**(2): 334-339.

Wang, X., B. Yang, et al. (2007a). "Tungsten oxide nanorods array and nanobundle prepared by using chemical vapor deposition technique ". ***Nanoscale research letters*** **2**(8): 405-409.

Wang, X. D., J. H. Song, et al. (2005). "Growth of uniformly aligned ZnO nanowire heterojunction arrays on GaN, AIN, and Al0.5Ga0.5N substrates". ***Journal of the American Chemical Society*** **127**(21): 7920-7923.

Wang, X. D., J. H. Song, et al. (2007b). "Direct-current nanogenerator driven by ultrasonic waves". ***Science*** **316**(5821): 102-105.

Wang, X. D., J. H. Song, et al. (2006b). "Single-crystal nanocastles of ZnO". ***Chemical Physics Letters*** **424**(1-3): 86-90.

Wang, X. D., C. J. Summers, et al. (2004a). "Large-scale hexagonal-patterned growth of aligned ZnO nanorods for nano-optoelectronics and nanosensor arrays". ***Nano Letters*** **4**(3): 423-426.

Wang, Z. L. (2004). "Zinc oxide nanostructures: growth, properties and applications". ***Journal of Physics-Condensed Matter*** **16**(25): R829-R858.

Wang, Z. L., X. Y. Kong, et al. (2004b). "Semiconducting and piezoelectric oxide nanostructures induced by polar surfaces". ***Advanced Functional Materials*** **14**(10): 943-956.

Warren, B. E. (1992). "X-Ray Diffraction". New York, Dover publications, INC.

Wei, H. Y., G. W. Cong, et al. (2007a). "Combined structure of ZnO vertical well-aligned nanorods and net-like structures on AIN/sapphire". ***Journal of Crystal Growth*** **306**: 12-15.

Wei, S. Y., Z. G. Wang, et al. (2007b). "First-principles studies on the Au surfactant on polar ZnO surfaces". ***Physics Letters A*** **363**(4): 327-331.

Wildgoose, G. G., C. E. Banks, et al. (2006). "Metal nanopartictes and related materials supported on carbon nanotubes: Methods and applications". ***Small*** **2**(2): 182-193.

Wildoer, J. W. G., L. C. Venema, et al. (1998). "Electronic structure of atomically resolved carbon nanotubes". ***Nature*** **391**(6662): 59-62.

Wu, C. L., L. Chang, et al. (2006). "Growth and characterization of chemical-vapor-deposited zinc oxide nanorods". ***Thin Solid Films*** **498**(1-2): 137-141.

Wu, Z. H., X. Mei, et al. (2003). "Growth, branching, and kinking of molecular-beam epitaxial < 110 > GaAs nanowires". ***Applied Physics Letters*** **83**(16): 3368-3370.

Wyckoff, R. W. G. (1982). "Crystal structures." New York, Interscience Publishers.

Xia, Y. N., P. D. Yang, et al. (2003). "One-dimensional nanostructures: Synthesis, characterization, and applications". ***Advanced Materials*** **15**(5): 353-389.

Xing, W., F. Li, et al. (2004). "Synthesis and electrochemical properties of mesoporous nickel oxide". ***Journal of Power Sources*** **134**(2): 324-330.

Xu, S. and G. Y. Liu (1997). "Nanometer-scale fabrication by simultaneous nanoshaving and molecular self-assembly". ***Langmuir*** **13**(2): 127-129.

Yan, M., H. T. Zhang, et al. (2003). "Self-assembly of well-aligned gallium-doped zinc oxide nanorods". ***Journal of Applied Physics*** **94**(8): 5240-5246.

Yang, P. D., H. Q. Yan, et al. (2002). "Controlled growth of ZnO nanowires and their optical properties". ***Advanced Functional Materials*** **12**(5): 323-331.

Ye, C. H., X. S. Fang, et al. (2005). "Zinc oxide nanostructures: Morphology derivation and evolution". ***Journal of Physical Chemistry B*** **109**(42): 19758-19765.

Ye, X. R., L. H. Chen, et al. (2006). "Electrochemical modification of vertically aligned carbon nanotube arrays". ***Journal of Physical Chemistry B*** **110**(26): 12938-12942.

Ye, X. R., Y. H. Lin, et al. (2003). "Decorating catalytic palladium nanoparticles on carbon nanotubes in supercritical carbon dioxide". ***Chemical Communications***(5): 642-643.

Ye, X. R., Y. H. Lin, et al. (2004). "Supercritical fluid synthesis and characterization of catalytic metal nanoparticles on carbon nanotubes". ***Journal of Materials Chemistry*** **14**(5): 908-913.

Ye, Z. Z., J. Y. Huang, et al. (2007). "Catalyst-free MOCVD growth of aligned ZnO nanotip arrays on silicon substrate with controlled tip shape". ***Solid State Communications*** **141**(8): 464-466.

Young, S. L., H. Z. Chen, et al. (2006). "Grain size effect on the colossal magnetoresistance in granular perovskite La0.7Pb0.3MnO3". ***Modern Physics Letters B*** **20**(29): 1859-1865.

Yu, C., Q. Hao, et al. (2005). "Integration of metal oxide nanobelts with microsystems for nerve agent detection". ***Applied Physics Letters*** **86**(6): 063101-1-063101-3.

Yumoto, H., T. Inoue, et al. (1999). "Application of ITO films to photocatalysis". ***Thin Solid Films*** **345**(1): 38-41.

Zaoui, A. (2004). "Energetic stabilities and the bonding mechanism of ZnO{0001}/Pd(111) interfaces". ***Physical Review B*** **69**(11): 115403-1-115403-8.

Zeng, C. L., D. S. Tang, et al. (2007). "Controllable preparation of SnO2 one-dimensional nanostructures by chemical vapor deposition". ***Acta Physica Sinica*** **56**(11): 6531-6536.

Zhang, J., F. H. Jiang, et al. (2005). "Catalyst-assisted vapor-liquid-solid growth of single-crystal Ga2O3 nanobelts". ***Journal of Physical Chemistry B*** **109**(27): 13143-13147.

Zhang, Y. L., Y. Liu, et al. (2006a). "Nanostructured columnar tin oxide thin film electrode for lithium ion batteries". ***Chemistry of Materials*** **18**(19): 4643-4646.

Zhang, Y. S., K. Yu, et al. (2006b). "Field emission from patterned SnO2 nanostructures". ***Applied Surface Science*** **253**(2): 792-796.

Zhang, Z., S. J. Wang, et al. (2007). "Controlling the growth mechanism of ZnO nanowires by selecting catalysts." ***Journal of Physical Chemistry C*** **111**(47): 17500-17505.

Zheng, G. F., F. Patolsky, et al. (2005). "Multiplexed electrical detection of cancer markers with nanowire sensor arrays". ***Nature Biotechnology*** **23**(10): 1294-1301.

Zhu, Y. W., H. Z. Zhang, et al. (2003). "Efficient field emission from ZnO nanoneedle arrays". ***Applied Physics Letters*** **83**(1): 144-146.

VITA

Jinfeng Wang was born on July 27, 1978 in Xuchang, China. In July of 2001 he graduated from Shandong University with a B.S. degree in Optical Information Science and Technology, Jinan, China. He completed his M.S. degree in Physics at Nankai University, Tianjin, China. In August of 2008, he received his Ph.D. degree in Physics from Missouri University of Science and Technology and University of Missouri-St. Louis.